

CHARACTERIZATION OF SOFT-TISSUE RESPONSE TO  
MECHANICAL LOADING USING NUCLEAR MAGNETIC  
RESONANCE (NMR) AND FUNCTIONAL MAGNETIC RESONANCE  
IMAGING (fMRI) OF NEURONAL ACTIVITY DURING SUSTAINED  
COGNITIVE-STIMULUS PARADIGMS

A dissertation submitted to the faculty of  
Worcester Polytechnic Institute  
in partial fulfillment of the requirements for the degree of  
Doctor of Philosophy in Biomedical Engineering  
by

---

Jeremy W. Wellen  
May 2003

Approved:

---

Christopher H. Sotak, Ph.D.  
Professor and Head, Major Advisor  
Biomedical Engineering Department  
Worcester Polytechnic Institute

---

Karl G. Helmer, Ph.D.  
Research Assistant Professor  
Biomedical Engineering Department  
Worcester Polytechnic Institute

---

James F. Paskavitz, M.D.  
Department of Neurology  
UMass Memorial Healthcare

---

George Pins, Ph.D.  
Assistant Professor  
Biomedical Engineering Department  
Worcester Polytechnic Institute

---

Ronald A. Cohen, Ph.D.  
Dept of Psychiatry and Human Behavior  
Brown Medical School



## **Acknowledgements**

I cannot imagine having completed this endeavor without the relentless support and encouragement from my wonderful new wife and family. Suki, you have been there for me through all the joys and sorrows I have experienced over the past years – I am eternally grateful for your support and companionship. Thanks also to my parents for instilling in me wholesome values, perseverance, and a work ethic that has carried me through many seemingly insurmountable tasks.

I would also like to thank the many individuals who played a vital role in the work that comprises this dissertation. Thanks to my advisor, Chris Sotak, for providing me with opportunity and guidance during my time at WPI. I have the utmost respect for your knowledge, leadership, enthusiasm and discipline in the pursuit of good science.

Thanks to Karl Helmer. Your hands-on participation and eagerness to get involved and teach by example has been an essential component to my education. I am a great fan of your open-mindedness and eclectic interests in all things science.

Thanks to Jim Paskavitz for having the determination to initiate the clinical fMRI research projects that I had the good fortune of being a part of. Your enthusiasm for the field and motivation to succeed are inspiring. Thanks also to Larry Sweet, Jeff Browndyke and Matt O'Connor for their dedication to and collaboration on the fMRI research projects.

Besides the knowledge base that this experience has afforded me, I am grateful for the opportunity to develop friendships with many lab colleagues that have come and gone over the years. A special thanks to Matt Silva for his great camaraderie and encouragement. I would truly never have even dreamt of embarking on this endeavor if Matt had not led the way. Thanks also to Erica Henning for lively chatter, conversations, and dedication to the lab. Additional thanks to Mike Meiler, Mark Kazemi, Alicia Briggs, Orna Mayzel, Fuhai Li and Xianjun Meng for valuable collaborations and discussions.

## Table of Contents

Table of Contents .....	i
Table of Figures.....	v
Table of Tables.....	viii
Abstract .....	ix
Chapter 1.....	12
<i>Principles of Nuclear Magnetic Resonance</i>	
1. Basic Physical Principles .....	13
1.1. Nuclear Angular Momentum .....	13
1.2. Nuclear Magnetic Dipole Moment .....	14
1.3. Nuclear Energy States.....	15
1.4. Classical Physics Description of NMR.....	19
1.5. Net Magnetization.....	21
1.6. Spin Excitation & The Rotating Frame of Reference.....	23
2. Free Induction Decay .....	27
3. Spin Echo .....	29
4. Bloch Equations.....	30
5. Relaxation Processes.....	34
5.1. Spin-Lattice ( $T_1$ ) Relaxation.....	35
5.2. Spin-Spin ( $T_2$ ) Relaxation.....	36
5.3. Fundamental Relaxation Mechanisms .....	38
6. Magnetic Resonance Imaging.....	44
6.1. Slice Selection.....	46
6.2. Frequency Encoding .....	49
6.3. Phase Encoding.....	50
6.4. Fourier Reconstruction.....	52
6.5. Imaging Pulse Sequences.....	54
Chapter 2.....	64
<i>NMR Measurement of Water Diffusion in Biological Tissue</i>	
Stimulated Echo Diffusion Imaging .....	64
1. The Diffusion Process.....	65
1.1. Brownian Motion & The Physical Model of Diffusion .....	65
1.2. Fick's Laws of Diffusion .....	67
2. Diffusion in Biological Systems .....	70
2.1. Restricted Diffusion .....	70
2.2. Tortuosity of Diffusion .....	71

2.3.	Diffusion Anisotropy .....	72
3.	NMR Measurement of Diffusion .....	73
3.1.	Pulsed Field Gradient Method .....	73
3.2.	Stimulated Echo Diffusion-Weighted Imaging .....	76
3.3.	Diffusion Tensor Imaging .....	78
<b>Chapter 3.....</b>	<b>83</b>	
	<i>Tendon Composition and Characterization by NMR</i>	
1.	Tendon Composition.....	84
1.1.	Hierarchical Organization of Collagen .....	84
1.2.	Tendon Ultrastructure .....	85
1.3.	Tendon Mechanical Properties .....	86
2.	Previous NMR Investigations of Tendon .....	87
2.1.	Spectroscopic Relaxation Time Characterization.....	87
2.2.	Spectroscopic Water Diffusion Characterization.....	88
<b>Chapter 4.....</b>	<b>91</b>	
	<i>Characterization of the Spectroscopic Water ADC(<math>t_{dif}</math>) in Rabbit Achilles Tendon</i>	
1.	Introduction.....	92
2.	Methodology .....	94
2.1.	Experimental Set-up.....	94
2.2.	NMR Experimental Parameters .....	95
3.	Results.....	96
4.	Discussion.....	96
5.	Conclusions.....	101
6.	Acknowledgments.....	102
<b>Chapter 5.....</b>	<b>103</b>	
	<i>Spatial Characterization of Tendon by NMR</i>	
1.	Introduction.....	104
2.	Methodology .....	106
2.1.	Sample Preparation .....	106
2.2.	Experimental Set-up.....	106
2.3.	NMR Experimental Parameters .....	108
2.4.	Data-Processing .....	110
3.	Results.....	113
3.1.	Tendon Imaging in Cross-Section .....	113
3.2.	Qualitative Analysis of 3-D Parameter Maps .....	114
3.3.	Quantitative Analysis of 3-D Parameter Maps .....	116
3.4.	Diffusion-Time Dependent ADC Imaging .....	118
4.	Discussion .....	121
4.1.	Spin Populations Observed in Imaging Experiments .....	121
4.2.	Localized Relaxation and ADC Parameter Values.....	123

4.3.	Data Interpretation With Respect to Tendon Ultrastructure .....	128
5.	Acknowledgements .....	129
<b>Chapter 6</b> .....		<b>130</b>
	<i>Functional Brain Imaging</i>	
1.	Physiological Origins of the BOLD Contrast Mechanism .....	131
1.1.	Hemodynamic Response to Neuronal Activation .....	132
1.2.	Magnetic Properties of Blood .....	132
1.3.	Magnetic-Susceptibility-Induced Signal Change .....	133
2.	Characteristics of the BOLD Response Signal .....	134
3.	Detection of Neuronal Activation .....	136
3.1.	Block Design Experiment .....	136
3.2.	fMRI Data Analysis .....	137
3.3.	Statistical Inference .....	139
<b>Chapter 7</b> .....		<b>141</b>
	<i>Dynamic Changes in Neural Network Activation Patterns</i>	
1.	Introduction .....	142
2.	Methodology .....	145
2.1.	Data Acquisition .....	145
2.2.	Subject Population .....	145
2.3.	Simple Motor Function .....	146
2.4.	Semantic Reasoning .....	146
2.5.	Visuospatial Processing .....	148
2.6.	Working Memory .....	149
2.7.	Temporal Analysis of Activation Refinement .....	151
3.	Results .....	152
3.1.	Simple Motor Function .....	153
3.2.	Semantic Reasoning .....	155
3.3.	Visuospatial Processing .....	158
3.4.	Working Memory .....	161
4.	Discussion .....	164
4.1.	Simple Motor Function .....	164
4.2.	Semantic Reasoning .....	166
4.3.	Visuospatial Processing .....	167
4.4.	Working Memory .....	168
4.5.	Data Analysis in Light of Heterogeneous BOLD Response .....	169
5.	Conclusions .....	170
<b>References</b> .....		<b>172</b>
<b>Curriculum Vita</b> .....		<b>180</b>



## Table of Figures

### Chapter 1

Figure 1.1 – Quantum energy levels of a spin- $\frac{1}{2}$ nucleus.....	17
Figure 1.2 – Precession of a nuclear magnetic moment.....	21
Figure 1.3 – Net magnetization vector for a spin- $\frac{1}{2}$ system. ....	23
Figure 1.4 – Laboratory and rotating frames of reference.....	25
Figure 1.5 – Magnetization perturbation by a $\mathbf{B}_1$ field.....	27
Figure 1.6 – Flip angles.....	28
Figure 1.7 – The spin-echo .....	30
Figure 1.8 – Longitudinal magnetization return to equilibrium condition .....	36
Figure 1.9 – Transverse magnetization return to equilibrium condition .....	38
Figure 1.10 – Spectral distributions of proton rotational frequency.....	42
Figure 1.11 – Axis orientation of the various MR imaging processes.....	46
Figure 1.12 – Slice thickness .....	48
Figure 1.13 – Sinc-modulated RF pulse.....	49
Figure 1.14 –Fourier transform of the exponentially decaying, sinusoidal FID signal.....	53
Figure 1.15 – Spin-echo imaging pulse sequence .....	56
Figure 1.16 – Gradient-recalled echo imaging pulse sequence.....	58
Figure 1.17 – Spin-echo sequence with 3-D image acquisition .....	59
Figure 1.18 – Partial flip angle RF excitation as implemented with a SE sequence. ....	61
Figure 1.19 – Blipped-EPI acquisition.....	63



## Chapter 2

Figure 2.1 – 1-D mean-squared displacement.....	67
Figure 2.2 – Pulsed-field-gradient spin echo method for diffusion weighting .....	75
Figure 2.3 – Pulsed-field-gradient stimulated echo method for diffusion weighting .....	78

## Chapter 3

Figure 3.1 – Overview of the organizational structure of tendon.....	86
--	----

## Chapter 4

Figure 4.1 – Hierarchy of tendon-holding apparatus .....	95
Figure 4.2 – Spectroscopically-acquired diffusion-time dependent plots of ADC.....	99

## Chapter 5

Figure 5.2 – Assembled experimental set-up with holding apparatus in magnet.....	107
Figure 5.3 – Example proton density weighted image of tendon cross-section .....	114
Figure 5.4 – Composite figure providing example output of $T_1$ , $T_2$ , $ADC_{\parallel}$ and $ADC_{\perp}$ .....	116
Figure 5.5 – Mean values of $ADC_{\parallel}$ and $ADC_{\perp}$ as a function of diffusion time .....	120
Figure 5.6 – Histograms of cumulative number of fitted pixels from ADC maps .....	121
Figure 5.7 – Dash-dot plots of $ADC_{\parallel}$ and $T_1$ .....	128

## Chapter 6

Figure 6.1 – Timing of a four-cycle blocked-task paradigm .....	137
Figure 6.2 – Relationship between $r(t)$ , $c+\varepsilon(t)$ , and $y(t)$ . .....	138

## Chapter 7

Figure 7.1 – Semantic reasoning paradigm .....	147
Figure 7.2 – Visuospatial processing paradigm .....	149
Figure 7.3 – 2-back working memory paradigm .....	150

Figure 7.4 – Subdivision of 4-cycles of the active epochs in the blocked paradigm .....152

Figure 7.5 – Simple motor function paradigm activation (fourths analysis) .....154

Figure 7.6 – Simple motor paradigm activation (entire stimulus waveform) .....155

Figure 7.7 – Semantic reasoning paradigm activation (fourths analysis).....157

Figure 7.8 – Semantic reasoning paradigm activation (entire stimulus waveform) .....158

Figure 7.9 – Visuospatial processing paradigm activation (fourths analysis).....160

Figure 7.10 – Visuospatial processing paradigm activation (entire stimulus waveform) ..161

Figure 7.11 – 2-back working memory paradigm activation (fourths analysis) .....163

Figure 7.12 – Behavioral response data from the 2-back WM task .....164

Figure 7.13 – Localization of three ROIs in motor control areas.....165

## Table of Tables

### Chapter 4

Table 4.1 – Initial slopes from the short $t_{\text{dif}}$ regime $\text{ADC}(t_{\text{dif}})$ vs. $t_{\text{dif}}^{1/2}$ plots .....	98
---	----

### Chapter 5

Table 5.1 – Summary of the pulse sequence parameters used to acquire imaging data.....	110
--	-----

Table 5.2 – Mean $\pm$ S.E.M. values for $T_1$ , $T_2$ , $\text{ADC}_{\parallel}$ and $\text{ADC}_{\perp}$ .....	117
--	-----

## Abstract

Research applications of nuclear magnetic resonance (NMR) span a broad range of fields and disciplines. The work presented in this dissertation attests to this fact. Specifically, the research topics discussed in the body of this work employ NMR spectroscopy and imaging to characterize the water diffusion and NMR relaxation times *ex vivo* in rabbit Achilles tendon and, in a clinical setting, employ functional magnetic resonance imaging (fMRI) to investigate the behavior of different neural networks over a period of sustained activity.

In the *ex vivo* in rabbit Achilles tendon work, a series of studies were performed. First, the diffusion-time dependence of the water apparent diffusion coefficient (ADC) was characterized in a spectroscopic mode with the samples subjected to different states of tensile loading. The results of this study demonstrated: (1) the anisotropy of the diffusion of water through tendon; (2) the ADC is diffusion-time dependent; (3) the values of the ADC( $t_{\text{dif}}$ ) curve increased with tensile loading; (4) a change at the short diffusion-time points that is consistent with the interpretation of a load-induced increase in the collagen fibril packing density; and (5) an increase in the water ADC at long diffusion times, hypothesized to be due to  $T_1$  editing.

To further investigate these issues, another series of *ex vivo* in rabbit Achilles tendon experiments was performed that employed NMR imaging to spatially characterize the water ADC,  $T_1$  and  $T_2$  relaxation time constants. As with the spectroscopic work, these studies were also conducted with the tendon samples subjected to different states of tensile loading. The results from these imaging experiments demonstrated: (1) two regions with distinct differences in signal intensity across the tendon: a thin region of

high signal intensity at the peripheral rim of the tendon that encircles a region of low signal intensity in the central core of the tendon; (2) a higher diffusion anisotropy ratio in the tendon central core relative to the peripheral rim; (3) upon tensile loading, significant increases in the ADC of water in the peripheral rim region and a corresponding increase in a measure of the change in proton density in the rim region, consistent with the hypothesis that tensile loading causes extrusion of water from the core to the rim region of the tendon; (4) this water extrusion is not uniformly distributed throughout the tendon rim region; and (5) the long-diffusion-time ADC behavior is consistent with the  $T_1$  spin editing hypothesis of the spectroscopic work.

From the clinical fMRI studies, an analysis method was presented for observing dynamic changes in brain regions involved in different neural network processes during a period of sustained activity. The results from these studies are consistent with the idea that over time, brain regions adapt to the given task demands through either recruitment or discharge of adjacent areas of tissue. These results also indicate that traditional analysis of block design fMRI studies may underestimate dynamic changes in brain regions during a sustained task. The analysis method may be useful as an exploratory tool to observe region specific variations in activation that may allow inferences to be made regarding how different brain regions adapt to and interact with one another during periods of extended activity.



# Chapter 1

## Principles of Nuclear Magnetic Resonance

---

### Basic Physical Principles

- Nuclear Angular Momentum
- Nuclear Magnetic Dipole Moment
- Nuclear Energy States
- Classical Physics Description of NMR
- Net Magnetization
- Spin Excitation & The Rotating Frame

### Free Induction Decay

### Spin Echo

### Bloch Equations

### Relaxation Processes

- Spin-Lattice ( $T_1$ ) Relaxation

### Spin-Spin ( $T_2$ ) Relaxation

### Fundamental Relaxation Mechanisms

### Magnetic Resonance Imaging

### Slice Selection

### Frequency Encoding

### Phase Encoding

### Fourier Reconstruction

### Imaging Pulse Sequences

### Spin Echo Imaging

### Gradient Recalled Echo Imaging

### 3-D Image Acquisition

### Echo Planar Image Acquisition

---

This chapter introduces those concepts of nuclear magnetic resonance (NMR) appropriate for the general reader as they apply to the experimental work presented in the subsequent chapters of this dissertation. The information presented begins with a discussion of the nuclear physics foundations of the phenomenon, from both the classical and quantum mechanical perspectives, to explain how magnetic nuclei interact with applied magnetic fields and radiofrequency pulses. In these initial sections, neither a classical or quantum mechanical approach is adopted in favor of the other since each provides valuable insights to an introductory portrayal of NMR. A discussion of NMR signal characteristics and how the environment of the nuclei of interest affects the signal appearance and behavior follows. Finally, these concepts are brought together and shown how they apply to the acquisition and generation of magnetic resonance images.

The general principles discussed in this section have an extensive historical foundation and numerous texts have been written on the topic. Several texts that have proved to be helpful resources while writing this section include those by Gadian (1995), Farrar (1989), and Callaghan (1993).

## 1. Basic Physical Principles

### 1.1. Nuclear Angular Momentum

Nuclei that can be detected in the NMR experiment possess nuclear angular momentum. The total angular momentum of a particle is comprised of two types of rotational motion: orbital motion, which is the motion of a particle with mass  $m$  rotating at an angular velocity  $\omega$  in a radius  $r$  about an axis; and spin rotational motion, which is an intrinsic property independent of its orbital motion. Nuclear angular momentum of atomic-scale particles is a quantized (i.e., only possesses



discrete values) vector quantity. The total angular momentum vector,  $\mathbf{J}$ , is the sum of the orbital and spin angular momentum components. The quantized value of the orbital angular momentum component of a particle is given by  $n\hbar/2\pi$  where  $n$  takes integer values and is known as the principle quantum number. [Note: due to the prevalence of  $2\pi$  in equations involving Planck's constant,  $\hbar/2\pi$  is often represented by  $\hbar$  and will be used periodically in this text.] Similarly, the magnitude of the spin angular momentum is quantized by a parameter known as the spin quantum number,  $I$ , and is given by  $\hbar[I(I+1)]^{1/2}$ . Depending on the combination of neutrons and protons in the nucleus of interest,  $I$  is an integer or half-integer value. Individually, protons and neutrons in the nucleus have spin quantum number  $I = 1/2$ . In the nucleus, these particles will pair with themselves, i.e., protons pair with protons and neutrons pair with neutrons, and cancel each other out. Consequently, the total spin angular momentum of the nucleus is determined by the spin of unpaired particles. For nuclei with an even atomic mass number,  $I$  is an integer value; those nuclei with an odd mass number have half-integer spin numbers (e.g.  $^1\text{H}$ ,  $^{13}\text{C}$  and  $^{31}\text{P}$  are examples of spin  $1/2$  nuclei); and  $I$  is zero for nuclei with even numbers of both protons and neutrons (e.g.  $^{12}\text{C}$  and  $^{16}\text{O}$  have zero spin and do not produce NMR signals).

## 1.2. Nuclear Magnetic Dipole Moment

Nuclei with non-zero spin (i.e.,  $I \neq 0$ ) possess a nuclear magnetic dipole moment,  $\mu$  (often referred to in an abbreviated manner as the magnetic moment). This parameter describes the magnitude and direction of the local magnetic field generated from the rotational motion of the net charges of the nuclear particles.

The magnetic moment of a nucleus is always oriented parallel to its angular momentum and the two properties are related to each other through a proportionality constant that is unique to a given nucleus and known as the magnetogyric (or gyromagnetic, depending upon your academic upbringing) ratio,  $\gamma$ . The relationship is expressed as:

$$\boldsymbol{\mu} = \gamma \mathbf{J} \quad (1.1)$$

From this equation it can be seen that if the total angular momentum of nuclei is zero (i.e.,  $I = 0$ ), then the nucleus will have no magnetic moment and hence will not produce an NMR signal.

### 1.3. Nuclear Energy States

The angular momentum and magnetic moment vectors are restricted to a finite number of possible orientations or states that are described by a set of magnetic (also referred to as directional) spin quantum numbers,  $m$ , determined from  $I$  and given by the series:

$$m_I = I, (I - 1), (I - 2), \dots, -I \quad (1.2)$$

As an example, for nuclei with spin quantum number  $I = \frac{1}{2}$  (referred to as a spin- $\frac{1}{2}$  nucleus), there are two possible magnetic spin quantum numbers,  $+\frac{1}{2}$  and  $-\frac{1}{2}$ ; for  $I = 1$ ,  $m_I$  may have values 1, 0,  $-1$ . In general, there are  $(2I + 1)$  possible states of the nucleus.

In the absence of a magnetic field, the magnetic moments have no preferred orientation and the energy is the same at each of the  $2I + 1$  different states, a condition in which the energies associated with each state are said to be degenerate (or the same). In the presence of a static magnetic field  $B_0$ , however, the interaction between the  $B_0$  field and the nuclear magnetic moment imparts potential energy to the nucleus that depends on the orientation of  $\mu$  with respect to the  $B_0$  field:

$$E_I = -\gamma\hbar m_I B_0 \quad (1.3)$$

where the magnetic quantum number  $m_I$  determines which of the  $(2I + 1)$  possible states a nucleus may occupy. For a spin- $1/2$  nucleus,  $m_I = +1/2$  or  $-1/2$  so there are two possible orientations of the magnetic moment with respect to the applied field: with  $m_I = +1/2$ , the z-component of the nuclear magnetic moment,  $\mu_z$ , is aligned with the  $B_0$  field; and with  $m_I = -1/2$ ,  $\mu_z$  is aligned against the  $B_0$  field, as shown in Fig. 1.1. The energy difference,  $\Delta E$ , between adjacent energy levels (i.e.,  $\Delta m_I = \pm 1$ ) is given by:

$$\Delta E = \gamma\hbar B_0 \quad (1.4)$$

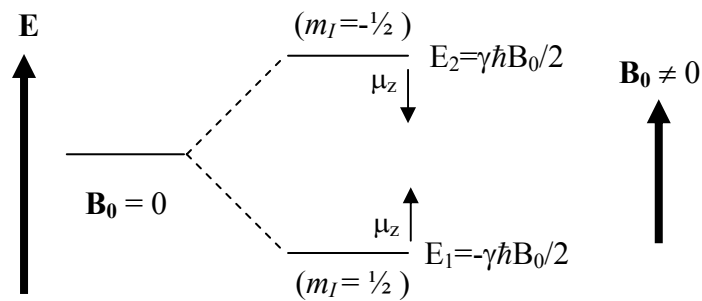


Figure 1.1 – Possible orientations of the z-component of the nuclear magnetic moment of a spin- $\frac{1}{2}$  nucleus, with respect to a static magnetic field  $B_0$ , and the energy associated with each orientation.

Transitions of nuclei between adjacent energy levels are required in order to observe an NMR signal. One of the fundamental aspects of quantum mechanics is the notion that electromagnetic radiation can be regarded as discrete packets, or quanta, of energy. Nuclear interaction with radiation involves the absorption or emission of one quantum of radiation, which results in a change in the energy state of the nucleus. Since energy must be conserved, the energy difference between the transitioned energy states is also equal to one quantum of radiation:  $\Delta E = h\nu$ , where  $\nu$  is the frequency of the absorbed or emitted radiation. From Eq. (1.4), we know the  $B_0$  field establishes the energy difference between states and that transitions between states are accompanied by the absorption or emission of a quantum of radiation with frequency obtained by relating Eq. (1.4) to the energy of a quantum of radiation:

$$\Delta E = h\nu_0 = \gamma(h/2\pi)B_0 \quad (1.5)$$

and therefore,

$$\nu_0 = \gamma B_0/2\pi. \quad (1.6)$$

To induce transitions between energy states, energy is applied to the system in the form of an oscillating electromagnetic field (which has a magnetic field component referred to as the  $B_1$  field). The frequency of the applied  $B_1$  field must satisfy Eq. (1.6) such that nuclei absorb the applied radiation and transition to the adjacent energy level. Since the gyromagnetic ratio,  $\gamma$ , is unique to each nuclear isotope, each nucleus will resonate at a different frequency in a given  $B_0$  field.

The number of nuclei that populate one of the  $(2I + 1)$  different energy levels that arise when a sample is placed in a  $B_0$  field is determined from the Boltzmann distribution. For a sample at thermal equilibrium, the nuclear population of an individual energy state  $N_I$  is given by:

$$N_I = \exp(-E_I/kT) \quad (1.7)$$

where  $E_I$  is the energy of state  $I$ ,  $k$  is the Boltzmann constant ( $1.38 \times 10^{-23}$  J/K) and  $T$  is the environmental temperature. What is detected in the NMR experiment is the population difference between energy states. Without a population difference between states, there would be equal numbers of transitions in both directions resulting in no net absorption of energy and therefore no NMR signal. Given a population of spin- $1/2$  nuclei where  $N_T$  represents the total number of spins in the population, from Eq. (1.7) it can be shown that the population difference  $\Delta N$  between the two spin states is:

$$\Delta N = \frac{N_T \gamma \hbar B_0}{2kT} \quad (1.8)$$

An increase in strength of the static  $B_0$  field increases the energy difference between adjacent states and hence their population difference. The greater population difference between energy states enhances the net absorption of energy from the applied  $B_1$  field, which, in turn, improves the signal-to-noise ratio of the NMR signal.

#### 1.4. Classical Physics Description of NMR

Prior to introducing some of the subsequent topics of this chapter, specifically those concerning spin excitation and relaxation, it is helpful to consider the description of the NMR experiment from a classical physics perspective.

In effort to maintain continuity with the quantum mechanical description of NMR, this section will begin by considering the behavior of particles with intrinsic angular momentum,  $\mathbf{J}$ , and a non-zero net magnetic moment,  $\boldsymbol{\mu}$ , which we know from Eq. (1.1) are related to one another through the gyromagnetic ratio,  $\gamma$ , of the isotope under consideration. In the presence of a static magnetic field, a torque is exerted on the magnetic moment of the particle, causing it to precess about the axis of the applied field at a frequency that is proportional to the field strength. The torque,  $\mathbf{L}$ , which acts on the particle is determined from the cross-product of the magnetic moment and the magnetic field:

$$\mathbf{L} = \boldsymbol{\mu} \times \mathbf{B} \quad (1.9)$$

By definition, torque is the time rate of change of angular momentum.

Therefore, we can relate the rate of change of a nucleus's angular momentum to the magnetic interaction between its magnetic moment and the static magnetic field:

$$d\mathbf{J}/dt = \mathbf{L} = \boldsymbol{\mu} \times \mathbf{B} \quad (1.10)$$

Using the relationship between the magnetic moment and angular momentum of a nucleus, Eq. (1.10) may be rewritten in terms of Eq. (1.1) as:

$$d\boldsymbol{\mu}/dt = \gamma d\mathbf{J}/dt = \gamma(\boldsymbol{\mu} \times \mathbf{B}) \quad (1.11)$$

For a given isotope in a static magnetic field, parameters  $\boldsymbol{\mu}$  and  $\mathbf{B}$  are constant, and, consequently, the magnetic moment will precess at a constant frequency. Realizing that  $(\boldsymbol{\mu} \times \mathbf{B}) = (-\mathbf{B} \times \boldsymbol{\mu})$  allows us to rearrange Eq. (1.11) to incorporate an angular frequency term:

$$d\boldsymbol{\mu}/dt = \gamma(\boldsymbol{\mu} \times \mathbf{B}) = (\boldsymbol{\omega} \times \boldsymbol{\mu}) \quad (1.12)$$

where

$$\boldsymbol{\omega} = -\gamma\mathbf{B} \text{ [rad/sec]} \quad (1.13)$$

is referred to as the Larmor equation. Thus, if an isotope with angular momentum and a non-zero net magnetic moment is placed in a magnetic field,  $\mathbf{B}$ , the torque produced from the interaction between the nuclear magnetic moment,  $\boldsymbol{\mu}$ , and the  $\mathbf{B}$  field prevents the nucleus from aligning with the field; instead it will 'precess' about the field with a characteristic angular frequency. The rotational

frequency vector is oriented antiparallel to the static field and is termed the precessional frequency,  $\omega_0$ , and its value is directly proportional to the applied field strength. Since the proportionality constant  $\gamma$  differs for each nuclear isotope, different nuclei resonate in a given magnetic field at different frequencies. These concepts are conveyed through the vector diagram of Fig. 1.2.

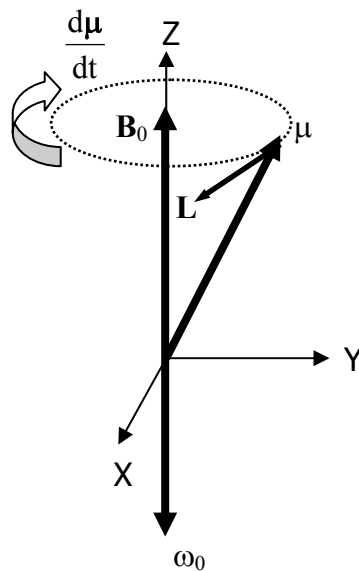


Figure 1.2 – Vector diagram of the precession of a nuclear magnetic moment,  $\mu$ , due to the torque,  $L$ , that a nucleus experiences due to the interaction between the magnetic moment and the static magnetic field,  $B_0$ .

### 1.5. Net Magnetization

When initially placed in a magnetic field, the individual nuclear magnetic moments are randomly oriented. With time, the magnetic moments tend to align along the direction of the  $B_0$  field with slightly more spins aligned parallel rather than anti-parallel to the field (i.e., there are more nuclei in the lower energy state



than in the upper state) in the case of a spin- $\frac{1}{2}$  system. This situation leads to the concept of the net longitudinal magnetization vector (another term for this is macroscopic magnetization),  $\mathbf{M}_0$ , which reflects the vector sum of the ensemble of magnetic moments in the sample. A time constant referred to as the spin-lattice time,  $T_1$ , characterizes the rate at which nuclei of a given sample establish this net magnetization after being placed in the  $B_0$  field (this topic will be covered more thoroughly in Section 5 of this chapter). The diagrams of Fig. 1.3 summarize the generation of  $\mathbf{M}_0$  in a pictorial manner from the classical physics perspective. Since the individual spins that comprise  $\mathbf{M}_0$  are randomly positioned on the surface of the cones shown in Fig. 1.3 (i.e., have no phase coherence), the xy-components of the individual nuclear magnetic moments cancel each other out and there is no component of the net magnetization that resides in the xy-plane (also referred to as the transverse plane). Thus, the net longitudinal magnetization,  $\mathbf{M}_0$ , is a static vector that is aligned parallel with the orientation of the static  $\mathbf{B}_0$  field and is proportional to the population difference between the two alignments.

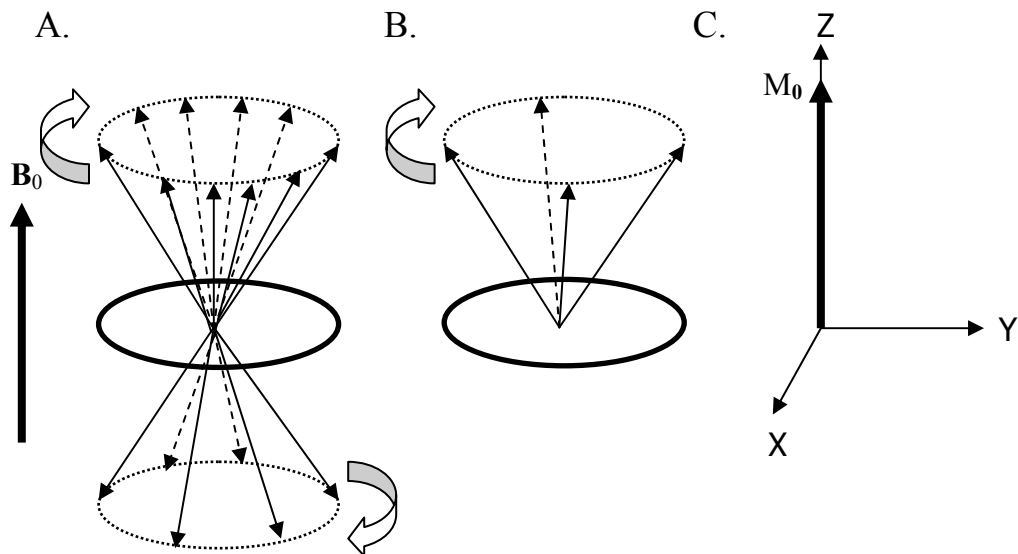


Figure 1.3 – Conceptual description of the composition of the net magnetization vector for a spin- $\frac{1}{2}$  system. A.) Individual nuclear magnetic dipole moments (arrowhead lines) align parallel or anti-parallel to the orientation of the applied static magnetic field  $\mathbf{B}_0$ . B.) In the Boltzmann equilibrium state, an excess of individual magnetic moments align in the energetically favorable orientation parallel to  $\mathbf{B}_0$ . C.) The magnitude of the net magnetization vector,  $\mathbf{M}_0$ , is the vector sum of the z-components of the individual magnetic moments with an orientation parallel to  $\mathbf{B}_0$ .

### 1.6. Spin Excitation & The Rotating Frame of Reference

To this point, the orientation of the external static magnetic field  $\mathbf{B}_0$  with respect to the Cartesian coordinate system has been along the z-axis. This is the common convention in the NMR field and all subsequent sections and chapters of this text will follow this convention. Therefore, any future reference to  $\mathbf{B}_0$  or  $\mathbf{M}_0$  will no longer be specifically designated a vector through the use of bold font as convention implies that the z-axis is collinear with either vector.

The effect of the radiofrequency (RF) pulse can be visualized as tipping of the net longitudinal magnetization some angle  $\theta$  away from equilibrium along the z-axis. This causes a vector component of the net magnetization,  $M_{xy}$ , to exist in the transverse plane from which an NMR signal can be detected. The Larmor equation, Eq. (1.13), predicts the precessional frequency of nuclei about an applied magnetic field. With respect to an observer standing in the laboratory frame of reference where the NMR experiment is conducted, the nuclei appear to be moving about the  $B_0$  field with angular frequency  $\omega_0 = \gamma B_0$ . If the observer were able to rotate in the direction of precession at a reference frequency  $\omega_r$ , then the nuclei would appear to precess with angular frequency  $(\omega_0 - \omega_r)$ .

Visualization of the behavior of the net magnetization vector is simplified by viewing the spins through what is known as the rotating frame of reference. If  $\omega_r$  of the rotating frame were equal to the Larmor frequency  $\omega_0$ , the net magnetization vector would appear stationary in the transverse plane after application of an RF pulse with  $\mathbf{B}_1$  directed along the (+x)-axis. This situation is conveyed in Fig. 1.4 (B.), which illustrates the clarity that the rotating frame of reference (differentiated from the laboratory frame by the prime marks on the axis labels) brings to the problem of visualizing the magnetization behavior in response to an RF pulse.

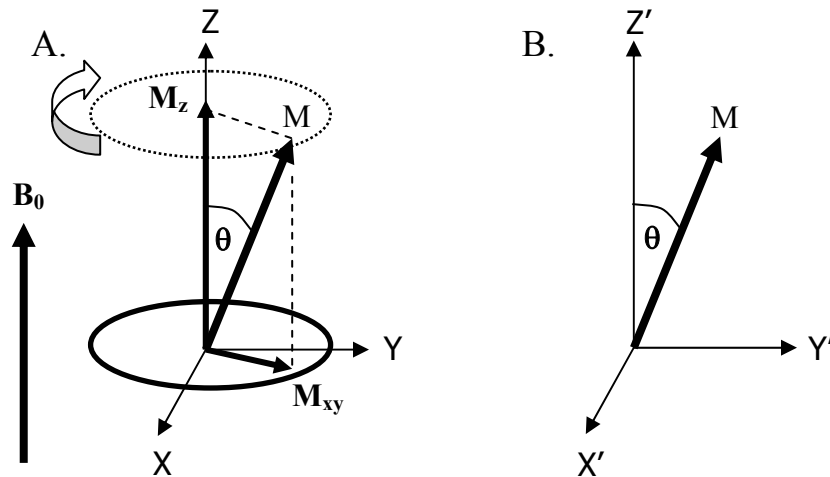


Figure 1.4 – A.) To the observer standing in the laboratory frame of reference, nuclei placed in a static magnet field  $B_0$  precess with angular frequency  $\gamma B_0$ . B.) In the rotating frame of reference, the point of reference is rotating at the same angular frequency as the precessing nuclei; therefore the net magnetization appears stationary as if there were no static magnetic field. The z-component of  $\mathbf{M}$  is often referred to as the longitudinal magnetization,  $M_z$ , and the component of  $\mathbf{M}$  in the xy-plane (i.e. the transverse plane) is often referred to as the transverse magnetization,  $M_{xy}$ .

In all the experiments discussed in this text, application of RF pulses of finite duration,  $t_p$ , are used to generate a magnetic field ( $B_1$ ) normal to the static  $B_0$  field. Consider the application of an RF pulse as viewed from the rotating frame of reference. The  $B_1$  field is the only field apparent in the rotating frame and therefore the magnetization is found to precess about the  $B_1$  field with angular frequency  $\gamma B_1$ . For a given  $B_1$  field strength, which is a function of the RF power, the net magnetization is tipped away from the z-axis in proportion to the duration of the applied field:

$$\theta = \gamma B_1 t_p \quad (1.14)$$

In Eq. (1.14), the degree to which the net magnetization is tipped away from the z-axis is given by  $\theta$ , a parameter often referred to as the flip angle. RF pulses that rotate the nuclei through an angle of  $90^\circ$  ( $\pi/2$  radians) bring the entire net magnetization vector into the transverse plane and are referred to as  $90^\circ$  pulses. A  $180^\circ$  pulse aligns the net magnetization vector along the negative z-axis and is often referred to as an inversion pulse.

The direction of rotation of the magnetization vector due to an applied  $\mathbf{B}_1$  field is dependent upon the phase of the applied field. As demonstrated in Fig. 1.5 from the perspective of the rotating frame of reference, the magnetization vector rotates in a clockwise direction about the  $\mathbf{B}_1$  vector. Figure 1.5 demonstrates this behavior for two incidences of magnetization perturbation. In Fig. 1.5 (A.), the  $\mathbf{B}_1$  field is directed along the (+x)-axis and the net magnetization vector is shown to rotate from equilibrium along the z-axis to align along the (+y)-axis. In Fig. 1.5 (B.), the  $\mathbf{B}_1$  field is directed along the (-x)-axis resulting in a rotation of the net magnetization vector toward the (-y)-axis.

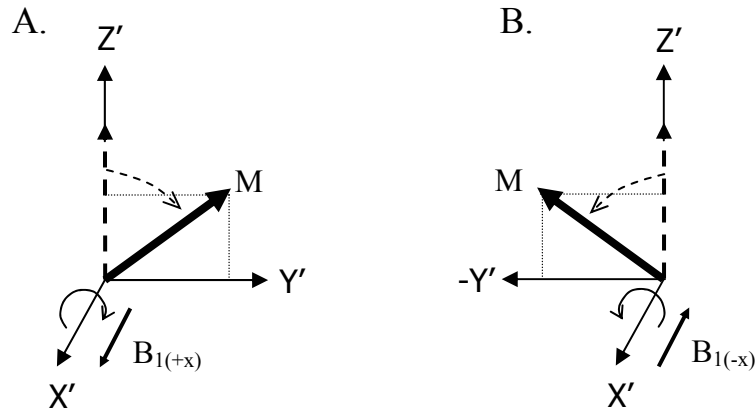


Figure 1.5 – Application of a  $\mathbf{B}_1$  field perturbs the magnetization vector from its equilibrium position along the (+z)-axis in a direction determined by the phase of  $\mathbf{B}_1$ . In (A.), the applied  $\mathbf{B}_1$  field is oriented with the (+x)-axis, rotating  $\mathbf{M}$  toward the (+y)-axis, i.e. in a direction clockwise about  $\mathbf{B}_1$ . B.) With the phase of  $\mathbf{B}_1$  oriented along the (-x)-axis, a clockwise rotation results in rotation of the magnetization vector toward the (-y)-axis.

## 2. Free Induction Decay

In the most basic NMR experiment, an RF pulse that produces a given flip angle  $\theta$  is applied to the sample of interest, a signal is induced in the RF receive coil which is amplified and displayed. The signal observed from this experiment is an exponentially-decaying sinusoid called a free induction decay (FID). The acquired signal reflects the RF resonance signal from the precessing spins. Application of an RF pulse imparts phase coherence to the spins that comprise the net magnetization, such that their precession about  $B_0$  is no longer totally random and, therefore, a net component of magnetization resides in the transverse plane,  $M_{xy}$ . The Larmor equation, Eq. (1.13), describes the rotational frequency  $\omega_0$  at which  $M_{xy}$  rotates about  $B_0$  in phase coherence. As depicted in Fig. 1.6, the amplitude of the FID is proportional to this transverse magnetization component. This figure provides examples of free induction decay experiments acquired with two different flip angles.

For the case where  $\theta = 30^\circ$ , note that the result is a smaller component of magnetization in the transverse plane and a correspondingly smaller amplitude FID than in the case where  $\theta = 60^\circ$ .

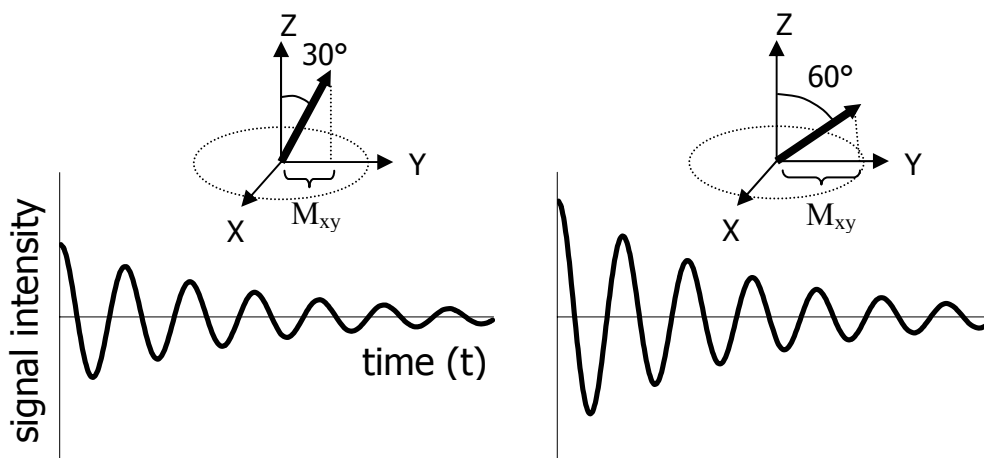


Figure 1.6 – Demonstration of the effect of different flip angles on the FID. At left, a short RF pulse that tips the magnetization  $30^\circ$  results in a smaller FID than the case on the right where a  $60^\circ$  pulse was applied. Note in the instance where a  $60^\circ$  flip angle was applied that a larger component of the magnetization vector resides in the xy-plane, yielding an FID of larger amplitude than that of the smaller flip angle.

After a period of time, the ensemble of spins that comprise  $M_{xy}$  begin to lose the phase coherence imparted by the RF pulse. The loss of phase coherence is a result of intrinsic relaxation processes of the nuclei in the system coupled with issues such as: contributions from magnetic susceptibility differences in the sample under study,  $B_0$  field inhomogeneity, and molecular diffusion effects. The cumulative effects of these processes are characterized by the relaxation time constant known as  $T_2^*$  and give rise to the exponential decay of the FID. Section 5 of this chapter will include a more detailed discussion of this relaxation parameter.

### 3. Spin Echo

Discovery of the spin-echo was made by Erwin Hahn (Hahn , 1950) and has added an important dimension to the field of NMR by employing a simple means of eliminating the de-phasing effects of susceptibility and  $B_0$  inhomogeneity that were touched upon in the previous section. Formation of the spin-echo can be explained through the aid of Fig. 1.7. Consider the component of transverse magnetization that arises after application of an RF pulse. Due to inhomogeneity of the  $B_0$  field, not all magnetic moments are exposed to the same static magnetic field and are thus precessing at slightly different frequencies. From the Larmor equation, we know that those spins subject to a static magnetic field larger than  $B_0$  precess at a slightly faster rate (F) than those slower precessing spins (S) subject to a static magnetic field slightly less than  $B_0$ . Therefore, spins begin to lose the phase coherence imparted by the RF pulse after a short period of time. The rate of this spin de-phasing is characterized by the  $T_2^*$  time constant mentioned in the previous section. In the spin-echo pulse sequence, a  $180^\circ$  RF pulse is applied some period of time after a  $90^\circ$  pulse. The  $180^\circ$  RF pulse rotates the transverse magnetization such that the spins are repositioned to locations that mirror their original positions about the rotation axis. At this point in the sequence, precession continues in the same direction and same rates as before the  $180^\circ$  pulse, except now the slower precessing spins 'lead' the faster precessing spins. This situation leads to re-phasing of the transverse magnetization and eventual formation of the spin-echo. Note from the figure that the magnitude of the spin-echo magnetization is smaller than that of the transverse magnetization after the initial  $90^\circ$  RF pulse. This magnetization decay is due to the



intrinsic relaxation processes of the system under study and is described by the  $T_2$  relaxation time constant. Relaxation concepts will be discussed further in Section 5 of this chapter.

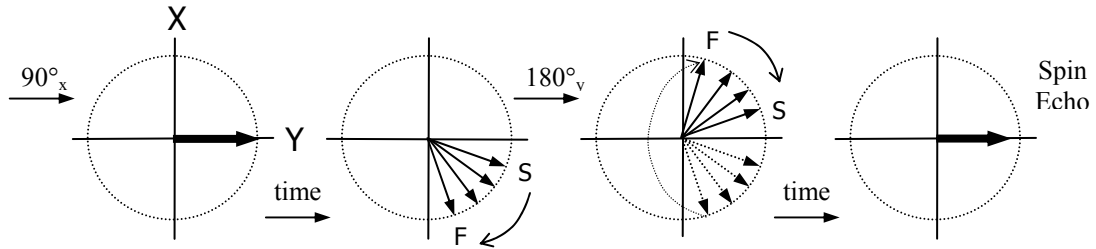


Figure 1.7 – Top-down view of the transverse plane showing how the spin-echo develops after application of a  $90^\circ$  RF pulse. As the net transverse magnetization vector precesses about  $B_0$ , the individual magnetic moments begin to lose the phase coherence imparted by the RF pulse.  $B_0$  inhomogeneity is the primary source of this de-phasing. Those spins subject to a static magnetic field larger than  $B_0$  precess at a slightly faster rate (F) than those subject to a static magnetic field at or slightly less (S) than  $B_0$ . The  $180^\circ$  pulse rotates the transverse magnetization such that the spins are repositioned to locations that mirror their original positions about the rotation axis (the Y-axis in this figure). Precession continues in the same direction and same rates as before the  $180^\circ$  pulse, leading to re-phasing and formation of the spin-echo.

#### 4. Bloch Equations

In 1946, Felix Bloch developed the theory that details the dynamic response of magnetization to perturbations in the form of equations of motion (Bloch, 1946).

Now known as the Bloch equations, this set of mathematical relationships describes the motional behavior of magnetization in response to exposure to static and time-varying magnetic fields. This section introduces that theory.

There are two sources of terms in the Bloch equations that influence the behavior of the net magnetization: precessional effects due to application of  $B_0$  and  $B_1$  fields, and

relaxation effects. We will begin by considering the effects of magnetic fields on the magnetization. First, Eq. (1.11) describes the time rate of change of a magnetic moment placed in a magnetic field as being proportional to the cross-product of the magnetic moment and the applied field. From the discussion of the concept of net (or macroscopic) magnetization in Section 1.5 of this chapter, it follows that Eq. (1.11) may be written in terms of  $\mathbf{M}$ :

$$d\boldsymbol{\mu}/dt = \gamma(\boldsymbol{\mu} \times \mathbf{B}) \rightarrow d\mathbf{M}/dt = \gamma(\mathbf{M} \times \mathbf{B}) \quad (1.15)$$

Here,  $\mathbf{B}$  represents the vector sum of the applied static magnetic field,  $B_0$ , and the magnetic field vector generated by an applied RF pulse,  $\mathbf{B}_1$ . Expanding the cross-product term in Eq. (1.15) yields:

$$\begin{aligned} \gamma(\mathbf{M} \times \mathbf{B}) &= \begin{vmatrix} \hat{i} & \hat{j} & \hat{k} \\ M_x & M_y & M_z \\ B_x & B_y & B_z \end{vmatrix} \\ &= \gamma[(M_y B_z - M_z B_y)\hat{i} + (M_z B_x - M_x B_z)\hat{j} + (M_x B_y - M_y B_x)\hat{k}] \end{aligned} \quad (1.16)$$

where  $(\hat{i}, \hat{j}, \hat{k})$  are (x, y, z) unit vectors. In Eq. (1.16), each of the magnetization and magnetic field vector components have an implied temporal dependence. Therefore, looking at the solution when the magnetization is exposed solely to the static  $B_0$  field (remember,  $B_0$  is collinear with the z-axis such that  $B_z = B_0$  and  $B_x = B_y = 0$  in Eq. (1.16)), we find that:

$$dM_z(t)/dt = 0 \quad (1.17)$$

$$dM_y(t)/dt = -\gamma B_0 M_x(t) = -\omega_0 M_x(t) \quad (1.18)$$

$$dM_x(t)/dt = \gamma B_0 M_y(t) = \omega_0 M_y(t) \quad (1.19)$$

That is, the equations of motion of  $\mathbf{M}$  in the transverse plane are described by first order differential equations. In the absence of any  $\mathbf{B}_1$  fields to excite the system, the z-component of magnetization is constant while the x- and y-components precess about the static field in accordance with the Larmor equation (i.e., Eq. (1.13)). Next, consider the effect of applying the time-varying  $\mathbf{B}_1$  field on the motional behavior of the magnetization. To begin, note that a linear oscillating magnetic field such as that of  $\mathbf{B}_1$  may be decomposed and expressed as the sum of two counter rotating fields with frequencies  $-\omega$  and  $+\omega$ :

$$\mathbf{B}_1(t) = B_1 \cos(\omega t) \hat{i} - B_1 \sin(\omega t) \hat{j} \quad (1.20)$$

Substituting the vector components of the decomposed  $\mathbf{B}_1$  into Eq. (1.16) provides the magnetization response to the combined effects of  $B_0$  and  $\mathbf{B}_1$ :

$$dM_z(t)/dt = -\gamma B_1 [M_x(t) \sin(\omega t) - M_y(t) \cos(\omega t)] \quad (1.21)$$

$$dM_y(t)/dt = \gamma [B_1 M_z(t) \cos(\omega t) - B_0 M_x(t)] \quad (1.22)$$

$$dM_x(t)/dt = \gamma [B_1 M_z(t) \sin(\omega t) + B_0 M_y(t)] \quad (1.23)$$

We next need to consider what happens to the magnetization after the application of an applied RF pulse that generates an excitatory  $\mathbf{B}_1$  field. When this occurs, the magnetization is said to relax. Relaxation occurs at different rates between the longitudinal and transverse magnetization and each can be expressed as follows:

$$dM_z(t)/dt = -(M_z - M_0)/T_1 \quad (1.24)$$

$$dM_y(t)/dt = -M_x(t)/T_2 \quad (1.25)$$

$$dM_x(t)/dt = -M_y(t)/T_2 \quad (1.26)$$

where  $T_1$  and  $T_2$  are referred to as the longitudinal and transverse relaxation time constants respectively. Combining the respective components of Eqs. (1.21) – (1.23) with those of Eqs. (1.24) – (1.26) yields the Bloch equations in their full form:

$$dM_z(t)/dt = -\gamma B_1 [M_x(t) \sin(\omega t) - M_y(t) \cos(\omega t)] - (M_z - M_0)/T_1 \quad (1.27)$$

$$dM_y(t)/dt = \gamma [B_1 M_z(t) \cos(\omega t) - B_0 M_x(t)] - M_y(t)/T_2 \quad (1.28)$$

$$dM_x(t)/dt = \gamma [B_1 M_z(t) \sin(\omega t) + B_0 M_y(t)] - M_x(t)/T_2 \quad (1.29)$$

Note that Eqs. (1.27) – (1.29) are the Bloch equations in the laboratory frame of reference. Through a coordinate system transformation, these equations can also be represented in the rotating frame of reference. The corresponding equations that arise after the transformation is performed are:

$$dM_z(t)/dt = -\gamma B_1 M_y'(t) - (M_z - M_0)/T_1 \quad (1.30)$$

$$dM_y(t)/dt = \gamma B_1 M_z(t) - (\omega_0 - \omega) M_x'(t) - M_y'(t)/T_2 \quad (1.31)$$

$$dM_x(t)/dt = (\omega_0 - \omega) M_y'(t) - M_x'(t)/T_2 \quad (1.32)$$

where  $\omega_0$  is the Larmor frequency,  $\omega$  is the frequency of the rotating frame about  $B_0$  and the components of magnetization in the rotating frame are given by:

$$M_x'(t) = M_x(t) \cos(\omega t) - M_y(t) \sin(\omega t) \quad (1.33)$$

$$M_y'(t) = M_x(t) \sin(\omega t) + M_y(t) \cos(\omega t) \quad (1.34)$$

Further discussion of and solutions to the differential equations developed in this section is provided in the section that follows regarding magnetization relaxation processes.

## 5. Relaxation Processes

Following perturbation of the equilibrium condition established after placing a sample in a magnetic field, relaxation processes proceed to return the magnetization back to the equilibrium state where the longitudinal magnetization,  $M_z$ , returns to a value of  $M_0$  and the transverse magnetization,  $M_{xy}$ , returns to zero. The magnetization returns to its state of equilibrium in an exponential fashion where the rate of return of  $M_z$  is measured by the time constant  $T_1$ ; likewise, the time constant  $T_2$  determines the rate of equilibration of  $M_{xy}$ . As will be discussed in the sections that follow, these relaxation time constants provide insight to the molecular motions and the surrounding environment inherent to the sample under study. A difference in time constants between different tissues in biological samples is one metric that can be used to generate tissue contrast in MR images.

The theoretical groundwork on relaxation mechanisms presented here is based on the work of Bloembergen, Purcell and Pound (1948) and is referred to as the BPP theory of relaxation. In their theory,  $T_1$  and  $T_2$  relaxation are expressed in terms of the correlation time  $\tau_c$  and the resonant frequency  $\omega_0$  of the structure under study.

Section 5.3 will discuss the mechanisms involved in each of these relaxation processes. Reference for much of the discussion included in the sections that follow stems from the writings of Fullerton and Cameron (1988).

### 5.1. Spin-Lattice ( $T_1$ ) Relaxation

The relaxation process that returns spins to the equilibrium state where the  $M_z$  component of magnetization returns to  $M_0$  is termed spin-lattice (or longitudinal) relaxation and is characterized by the time constant  $T_1$ . The reference to a lattice in the  $T_1$  relaxation terminology is used because the process involves the exchange of energy between the spins and their molecular environment, which is referred to as the lattice. Longitudinal relaxation restores the spin-population difference established by the Boltzmann equilibrium condition, as given through Eq. (1.8), by returning spins to the lower energy state, thereby giving up energy to the environment (i.e., the lattice). In the development of the Bloch equations in Section 4 of this chapter, the relaxation behavior to the  $M_z$  component of magnetization motion was included in the form of Eq. (1.24). This first-order differential equation describes the exponential return of the longitudinal component of magnetization to its equilibrium condition of  $M_0$ . The solution to Eq. (1.24) may be expressed in the following form:

$$M_z(t) = M_0 + Ce^{-t/T_1} \quad (1.35)$$

where  $C$  represents the constant of integration which will be determined from the initial condition of the system under study. For example, at time  $t = 0$  following a  $90^\circ$  RF pulse, the component of magnetization in the longitudinal plane is zero as shown in the diagram in Fig. 1.8 (A.). Given this initial condition,  $M_z(t=0) = 0$ , yields the constant  $C = -M_0$ . With the equilibrium condition disrupted by an  $180^\circ$  inversion pulse, the initial condition at time  $t = 0$  becomes  $M_z(t=0) = -M_0$ , as demonstrated in the diagram in Fig. 1.8 (B.). In this case, the constant  $C$

becomes  $-2M_0$ . Following application of the RF pulse,  $M_z(t)$  follows the exponential return to equilibrium as shown in each of the plots of Fig. 1.8.

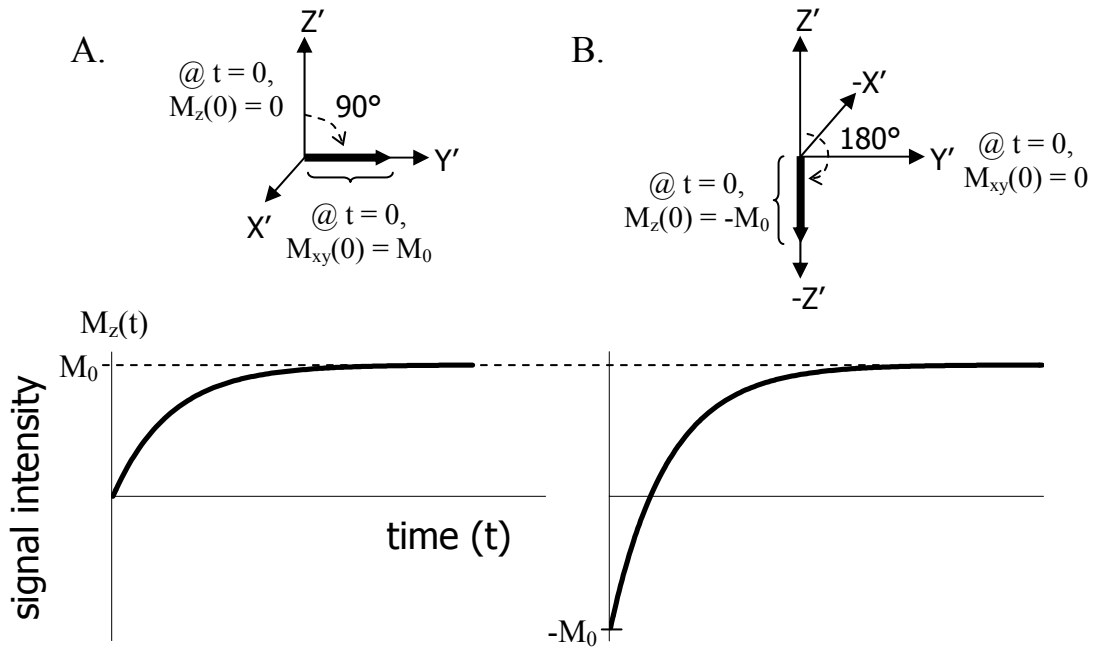


Figure 1.8 – Response of the longitudinal magnetization after RF perturbation from the equilibrium condition. A.) After application of a  $90^\circ$  RF pulse, the longitudinal plane has no component of magnetization, i.e. corresponds with the initial condition  $M_z(0) = 0$ . B.) Following a  $180^\circ$  RF pulse, the initial condition is  $M_z(0) = -M_0$ .  $M_z(t)$  returns to its equilibrium condition following each perturbation in an exponential manner with time constant  $T_1$ , as shown in each diagram.

## 5.2. Spin-Spin ( $T_2$ ) Relaxation

As discussed in Section 1.5 of this chapter, at equilibrium the net magnetization vector is oriented along the longitudinal axis and the net magnetization in the transverse plane is zero. Application of an RF pulse moves a component of the magnetization vector into the transverse plane such that the net transverse magnetization becomes non-zero. Following application of an RF pulse, this transverse magnetization decays away in an exponential fashion characterized by

a time constant referred to as  $T_2$ . This time constant is referred to as the spin-spin (or transverse) relaxation. The term spin-spin reflects the notion that this relaxation process involves interactions between neighboring nuclear spins without any exchange of energy with the lattice. In the previous discussion of the Bloch equations, we introduced the  $T_2$  relaxation time constant as a measure of the rate of decay of transverse magnetization. This relaxation is an exponential process that may be expressed as in Eqs. (1.25) and (1.26). Solutions to these first-order differential equations take the form:

$$M_{x,y}(t) = M_{x,y}(0)e^{-t/T_2} \quad (1.36)$$

where  $M_{x,y}(0)$  expresses the initial component of transverse magnetization following application of the RF excitation pulse.

Figure 1.9 depicts the behavior of transverse magnetization in the rotating frame following excitation by a  $90^\circ$  RF pulse. Immediately following the  $90^\circ$  RF pulse, the magnetization in the transverse plane has the value  $M_{x,y}(0) = M_0$ . Due to accumulation of a variety of relaxation effects that include inhomogeneity in the static  $B_0$  field, magnetic susceptibility differences within the sample, molecular diffusion, and intrinsic  $T_2$  relaxation within the sample, the transverse magnetization begins to lose phase coherence over time. The time constant that describes the transverse magnetization decay in response to these cumulative effects is referred to as  $T_2^*$ . This effect is depicted for two time points in Fig. 1.9 (B.) and (C.) as the individual magnetic moments that comprise  $M_{x,y}$  separate



and, correspondingly, the magnitude of the  $M_{x,y}$  vector along the  $Y'$ -axis is reduced. The plot below the vector diagrams demonstrates the exponential decay by  $T_2^*$  of transverse magnetization from the initial condition of  $M_{x,y}(0) = M_0$  that corresponds with the loss of phase coherence. The mechanisms responsible for the magnetization relaxation are discussed in detail in the section that follows.

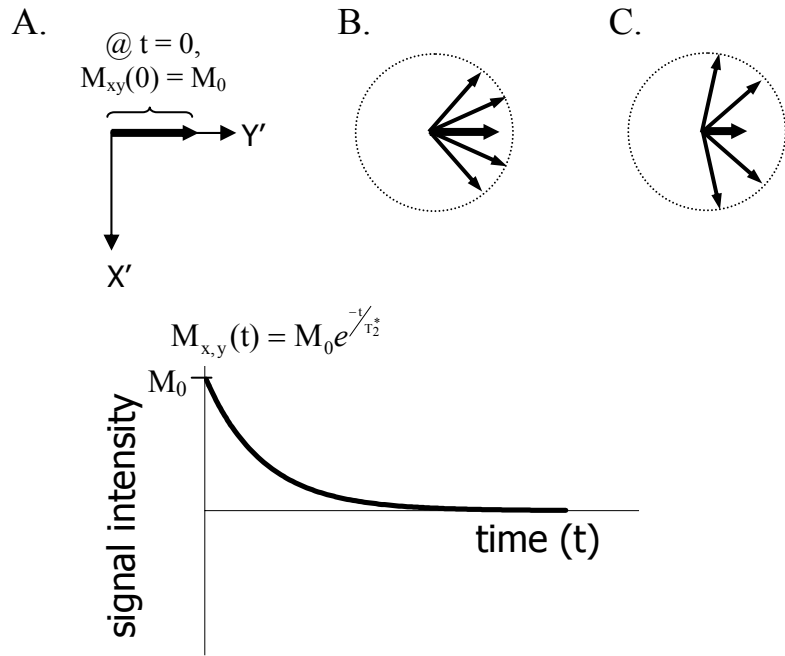


Figure 1.9 – Exponential decay of the transverse magnetization following RF excitation as it loses phase coherence in its return to the Boltzmann equilibrium condition (i.e.,  $M_{xy} = 0$ ). A.) Following application of a  $90^\circ$  RF pulse, magnetization resides in the transverse plane with the initial condition  $M_{x,y}(0) = M_0$ . B.) and C.) As time progresses, the transverse magnetization loses phase coherence and the magnitude of the  $M_{x,y}$  vector along the  $Y'$ -axis is reduced as it returns to its equilibrium condition in an exponential manner with time constant  $T_2^*$ .

### 5.3. Fundamental Relaxation Mechanisms

In order to understand the nature of the processes that lead to magnetization relaxation, it must be appreciated that the molecules within a given sample

possess a distribution of motions that may take the form of vibrational, rotational and translational molecular motions. Specifically, the discussion that follows will focus on intramolecular dipole-dipole interactions for which translational and rotational motions are the only motions that need to be considered.

Translational motion represents the spatial displacement of molecules due to molecular collisions. Rotational motion is due to the random tumbling of molecules. The spectral density function,  $J(\omega)$ , is a parameter that characterizes motional frequencies in a sample and may be expressed as:

$$J(\omega) = \frac{\tau_c}{1 + \omega^2 \tau_c^2} \quad (1.37)$$

where the correlation time,  $\tau_c$ , is a temperature-dependent parameter that expresses the characteristic time-scale of the molecular motion. Given a molecule in some state of motion,  $\tau_c$  can be thought of as the average time between molecular collisions for translational motion. For rotational motion,  $\tau_c$  is the time it takes for a molecule to rotate through one radian. For example,  $\tau_c$  of water molecules in solution at room temperature is  $\sim 3 \times 10^{-12}$  sec. At a given temperature, larger molecules such as lipids or proteins will have longer correlation times than smaller molecules. Correlation time is also conveyed in terms of frequency, which, in keeping within the scope of this discussion, implies a collisional or rotational frequency that is inversely proportional to  $\tau_c$ , i.e.,  $\omega_c = 1/\tau_c$ .

Magnetization relaxation results from fluctuations in the local magnetic field that nuclei are exposed to in the same manner that nuclei are excited by a fluctuating magnetic field produced by an RF pulse. Of the various internal mechanisms that produce fluctuating local magnetic fields in biological systems, the dominant mechanism that promotes relaxation involves intramolecular dipole-dipole interaction. Dipole-dipole coupling has both static and dynamic components. Consider the interactions between the magnetic moments of the two  $^1\text{H}$  nuclei in a water molecule. Static magnetic coupling between proton pairs arises if the water molecule were bound to a macromolecule with a long  $\tau_c$  such that, relative to unbound water molecules, it is rotating so slowly that each proton experiences a small contribution to its total magnetic field due to its neighbor. As a result, the static component of the magnetic coupling between the two dipoles adds a magnetic field inhomogeneity component that dephases transverse magnetization and contributes to  $T_2$  relaxation.

The source of the dynamic component of dipole-dipole coupling is the translational and random tumbling motion of molecules in a sample. Consider again the two  $^1\text{H}$  nuclei in a water molecule. The total magnetic field experienced by each nucleus is the sum of the static  $\mathbf{B}_0$  field and the local contribution from the magnetic moment of the neighboring nucleus. As the molecular motion progresses, the motions of the nuclear magnetic moments generate fluctuating magnetic fields; that is, each magnetic moment exposes its neighbors to a magnetic field that varies at the molecular tumbling frequency.

These microscopic fluctuating fields behave in a manner similar to the  $\mathbf{B}_1$  field generated by an RF pulse. The difference being these fluctuating fields are associated with the lattice and there is an exchange of energy until the nuclear spins are in thermal equilibrium with the lattice, i.e. the population difference of the energy states has returned to the Boltzmann equilibrium condition. For this reason, the relaxation mechanism of dynamic dipole-dipole coupling is most efficient when the characteristic frequency of the molecular motion,  $\omega_c = 1/\tau_c$ , is equal to the resonance frequency  $\omega_0$ . That is, if the motional frequencies are similar to the Larmor frequency, there is efficient exchange of energy with the lattice, resulting in a short  $T_1$  time constant.

The plots in Fig. 1.10 depict relative spectral distributions for three idealized molecular environments. For large molecules such as proteins (– line),  $J(\omega)$  is confined over a smaller range of rotational frequencies compared with the much larger frequency range of smaller molecules. For a sample in a magnetic field of a given magnitude, the measured relaxation time depends on the number of molecules with motional frequencies at the resonance frequency  $\omega_0$  relative to all other frequencies. Note that with the transition from large to small molecules, the decrease in  $\tau_c$  (i.e.,  $\omega_c$  increase) corresponds with a decrease in the relative number of molecules at a particular motional frequency. Since these motional frequencies are fixed by the thermal energy of the surrounding environment, and knowing the resonance frequency is dependent on magnetic field strength (i.e., through the Larmor equation, Eq. (1.13)), efficient energy transfer at the Larmor

frequency depends on magnetic field strength. If the population of molecules represented by a given spectral distribution is a function of frequency, then change of  $B_0$  will cause a change in relaxation rate.

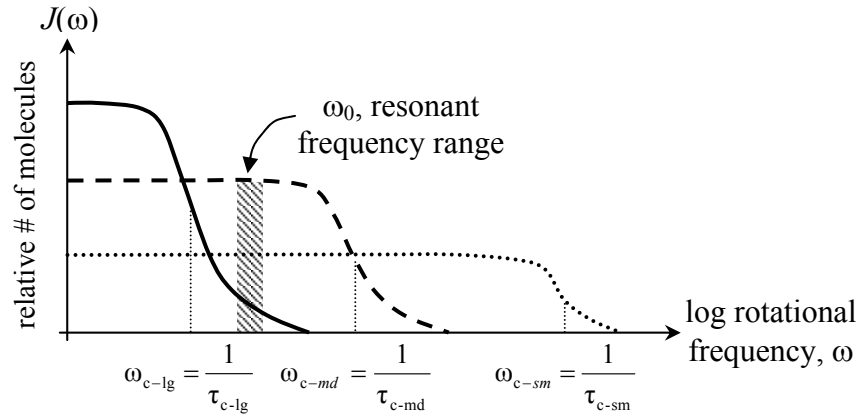


Figure 1.10 – Log of spectral distributions ( $J(\omega)$ ) of proton rotational frequency as characterized by correlation times of molecules from three size ranges: (—) long  $\tau_c$  (e.g. from large molecules such as proteins); (---) mid-range  $\tau_c$  (e.g. from medium-sized molecules such as lipids); (···) short  $\tau_c$  (e.g. from small molecules such as water).

We now move from a qualitative description of the effects of molecular motion on magnetization relaxation to the BPP theory of relaxation. In their work, Bloembergen *et al.* (1948) derived expressions to describe the specific influence of rotational motion on magnetization relaxation rates. These equations express relaxation rates ( $R_1 = 1/T_1$  and  $R_2 = 1/T_2$ ) in terms of the molecular correlation time and the resonant frequency:

$$R_1 = \frac{1}{T_1} = K \left[ \frac{\tau_c}{1 + \omega_0^2 \tau_c^2} + \frac{4\tau_c}{1 + 4\omega_0^2 \tau_c^2} \right] \quad (1.38)$$

$$R_2 = \frac{1}{T_2} = \frac{K}{2} \left[ 3\tau_c + \frac{5\tau_c}{1 + \omega_0^2\tau_c^2} + \frac{2\tau_c}{1 + 4\omega_0^2\tau_c^2} \right] \quad (1.39)$$

where  $K$  is a constant dependent on a number of parameters related to the nuclear isotope of interest (e.g.,  $^1\text{H}$  atoms in a water molecule are separated by 1.6 Å yield  $K = 1.02 \times 10^{-10}$  in SI units). To gain an appreciation for the implications of these expressions, consider the classes of molecules used in Fig. 1.10. With their three different sizes (and their corresponding correlation times), it is expected that for a given resonance frequency, each will have different motional properties that affect their respective relaxation rates.

For the case of small, mobile molecules such as bulk water, the ( ... ) plot in Fig. 1.10 shows that the fraction of molecules with a given motional frequency is the same over a broad range of frequencies. This implies that the relaxation rate is independent of the resonance frequency for molecules with short  $\tau_c$ . For  $\tau_c \sim 3 \times 10^{-12}$  sec (approximate correlation time of pure water at room temperature), the  $(\omega_0\tau_c)^2$  terms in the denominator of Eqs. (1.38) and (1.39) become much less than one, leaving equivalent relaxation rates given as:

$$R_1 = K[\tau_c + 4\tau_c] = R_2 = (K/2)[3\tau_c + 5\tau_c + 2\tau_c] = 5K\tau_c \quad (1.40)$$

This is an example of the so-called extreme-narrowing regime and demonstrates the conditions whereby  $T_1$  and  $T_2$  relaxation times become equivalent and independent of the resonant frequency condition.

As molecular size increases, molecular motion slows and the corresponding molecular correlation times increase. With regard to relaxation values, as the  $\omega_0\tau_c$  terms of Eqs. (1.38) and (1.39) become  $\geq 1$ , the  $T_1$  and  $T_2$  values transition from the extreme-narrowing regime, where they have nearly equivalent values, to a region where their values diverge. Both  $T_1$  and  $T_2$  show a frequency dependence:  $T_1$  values reach a minimum and begin to increase while  $T_2$  values decrease as correlation times increase. This frequency dependence is demonstrated in the ( - - ) and ( - ) plots of spectral density in Fig. 1.10. Relative to the small molecule plot, (  $\cdots$  ), a small change in the resonance frequency causes a change in the fraction of molecules rotating at the resonant frequency. As the resonant frequency increases,  $T_1$  relaxation time becomes longer because the fraction of molecules with motional frequencies at  $\omega_0$  becomes smaller. For this reason, the  $T_1$  relaxation time of solids and large macromolecules is strongly frequency dependent.

## 6. Magnetic Resonance Imaging

The first published account of an object imaged by means of NMR was in 1973 by Paul Lauterbur (Lauterbur, 1973). By taking advantage of the Larmor relationship between the resonance frequency and the magnetic field it is exposed to, Lauterbur showed that applying a linear magnetic field gradient over the static  $B_0$  field yields spatial information of the object in the form of one-dimensional profiles. By varying the direction of the applied gradient, a series of these profiles could be used to create an image using projection reconstruction methods employed in contemporary imaging modalities of the day such as x-ray computed tomography. Rapid

development of this new application followed with the first NMR image of a live human being published in 1977 (Damadian *et al.*, 1977).

The projection-reconstruction method used in the original demonstrations of MR imaging has been superseded by the technique of Fourier transform imaging (Edelstein *et al.*, 1980), which is employed in the majority of modern MR imaging methods. In general, the amplitude of the MR signal acquired during Fourier transform imaging represents the transverse magnetization of the signals from the object of interest at some point defined through a sequence of RF and magnetic field gradient pulses. The discussion of MR imaging that follows introduces the main aspects of Fourier transform imaging as they relate to how they were employed in the research applications of subsequent chapters of this work. To that end, the processes of slice-selection, frequency- and phase-encoding will be introduced, followed by data reconstruction by means of the Fourier transform and examples of some common pulse sequences used to acquire MR images. In discussing these topics, a common acquisition geometry orientation will be assumed to help the reader develop a grasp of the topics. In the sections that follow, a Cartesian coordinate system will be used to discuss the different components of the MR image acquisition process. During this discussion, an axial image plane orientation will be assumed whereby the different image acquisition processes are oriented as in the coordinate system shown in Fig. 1.11. In practice, however, the orientation of these processes with respect to the fixed Cartesian coordinates will vary depending on the desired image plane section of interest through the sample.



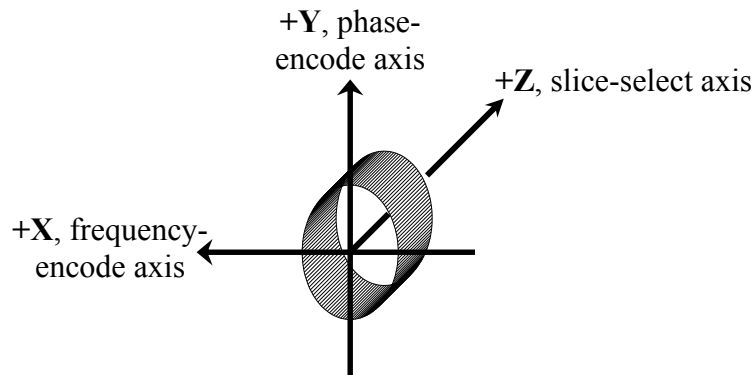


Figure 1.11 – Axis orientation of the various MR imaging processes for axial plane image acquisition through the object of interest as discussed in the sections that follow: x-axis is the frequency-encode direction; y-axis is the phase-encode direction; and slice-selection is along the z-axis.

### 6.1. Slice Selection

On those occasions where information pertaining to only a portion of the object under study is desired, slice-selective imaging is used. This technique limits the extent of information obtained from the object by exposing a limited region of the object to RF excitation as opposed to exciting spins over the entire sample with a non-slice-selective excitation pulse. Selective excitation is achieved by simultaneously applying a magnetic field gradient with a frequency-selective RF pulse. With a linear field gradient applied in the direction normal to the desired imaging plane (e.g. applied along the z-axis as in Fig. 1.11 for an axial plane image), the effective magnetic field ( $B_{\text{eff}}$ ) experienced by the spins in the object becomes dependent on position along the axis of the applied gradient:

$$B_{\text{eff}} = B_0 + G_z z \quad (1.41)$$

where  $B_0$  is the static magnetic field;  $G_z$  is the amplitude of the linear field gradient applied along the z-axis; and  $z$  is the position from isocenter along the z-axis. Following from the Larmor equation, Eq. (1.13), the resonant frequency of spins excited by an RF pulse during the application of a magnetic field gradient will have a positional dependence and vary according to  $B_{\text{eff}}$ :

$$\omega_{\text{eff}} = \gamma(B_0 + G_z z). \quad (1.42)$$

It follows then, that excitation with a frequency-selective RF pulse made up of a narrow range of frequencies would selectively excite a region of the object where the resonant frequencies fall in that range. The spatial extent of this excited region is referred to as the slice thickness. Control of this variable is performed by selective variation of the RF pulse bandwidth or the strength of the applied magnet field gradient. For an RF frequency bandwidth of  $\Delta\omega$ , the slice thickness  $\Delta z$  is given by:

$$\Delta z = \frac{2\pi\Delta\omega}{\gamma G_z} \quad (1.43)$$

The interdependencies between these two parameters are demonstrated in Fig. 1.12 and show how either a wider band of RF frequencies or a lower magnetic field gradient will result in a larger slice thickness.

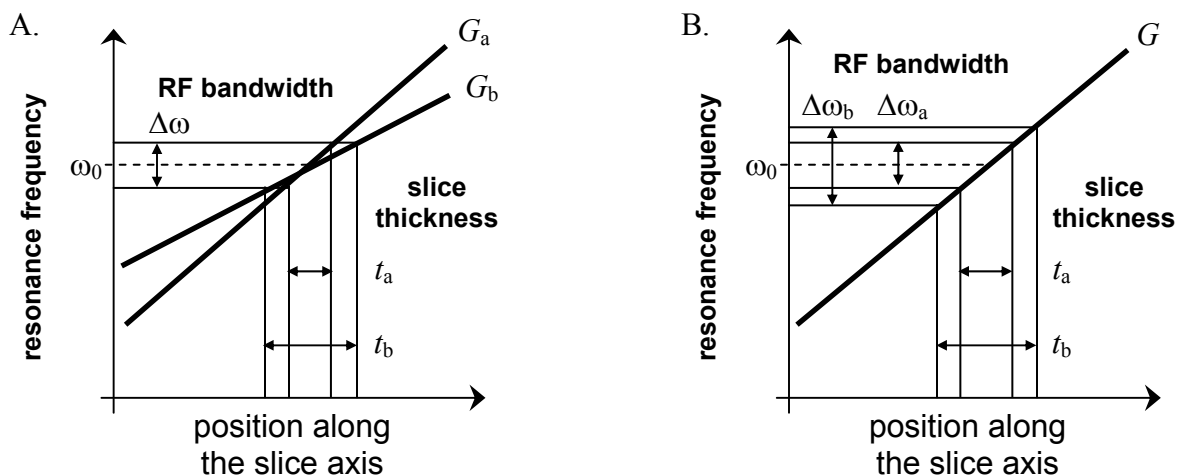


Figure 1.12 – The RF pulse bandwidth ( $\Delta\omega$ ) and the strength of the magnetic field gradient ( $G$ ) are the determinants of slice thickness ( $t$ ). In practice, slice thickness is varied using either of these variables. A.)  $\Delta\omega$  is held constant and  $G$  is varied, yielding a slice thickness that is inversely proportional to  $G$  ( $G_a > G_b$  and  $t_a < t_b$ ). B.)  $\Delta\omega$  is varied and  $G$  is held constant yielding a slice thickness that is proportional to  $\Delta\omega$  ( $\Delta\omega_a < \Delta\omega_b$  and  $t_a < t_b$ ). The slice position is controlled by varying  $\omega_0$ .

The ideal frequency-selective RF pulse will achieve uniform excitation of spins throughout the thickness of the selected slab and simultaneously ensure no excitation occurs outside the slab. To satisfy these requirements, consider the frequency response of the pulse shape. As shown in Fig. 1.13, the sinc and the rectangle functions are related to one another through the Fourier transform. By capitalizing on this relationship, a sinc-shape-modulated excitation pulse can be used to generate a rectangular-shaped frequency response. The transmitter frequency modulated by the sinc shape corresponds with the central excitation frequency of the excited slice profile while the extent of the slice, as discussed in

Fig. 1.12, is partially dependent on the RF pulse bandwidth:  $\Delta\omega = 2\pi \Delta f = 2\pi (1/2T)$ . Therefore, an RF pulse consisting of a narrow frequency range excites a narrow spatial distribution of nuclei within the sample along the slice selection axis.

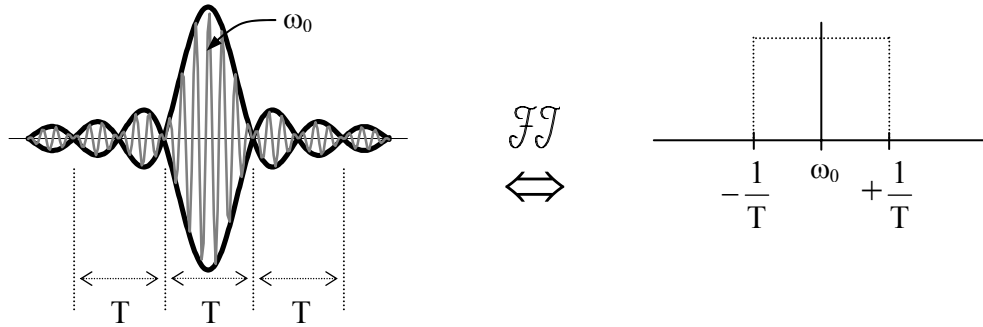


Figure 1.13 – The sinc-modulated RF pulse with transmitter frequency  $\omega_0$  and period  $T$  is related to a rectangle-shaped function with center frequency  $\omega_0$  and width  $(1/2T)$  through the Fourier transform.

## 6.2. Frequency Encoding

In an analogous manner to the spatial encoding of the slice-selection process, the in-plane frequency encoding process applies a magnetic field gradient (referred to as the read-out gradient) during the data acquisition period to encode spatial information along the direction of the applied read-out gradient. As depicted in Fig. 1.11, where the read-out gradient is applied along the x-axis, the spatial extent of the image is based on an interrelationship between the signal bandwidth (BW), the gradient amplitude ( $G_x$ ) and the field of view ( $FOV_x$ ) as:

$$FOV_x = \frac{BW}{\gamma G_x} \quad (1.44)$$

where  $BW = N/t_{\text{acq}}$  ( $N$  is the number of sampling points collected during the acquisition period,  $t_{\text{acq}}$ ). These parameters define the spatial resolution of the resulting image in the read-out direction and Eq. (1.44) demonstrates three approaches available to increase image resolution in this dimension: (1) reduce the  $\text{FOV}_x$  (while simultaneously increasing gradient amplitude  $G_x$  by the same factor); (2) lower the bandwidth; and (3) increase the number of sampling points. It should be noted that each approach to increase image resolution generally has a corresponding drawback that must be considered to obtain good image quality. For example, increasing image resolution by doubling the number of sampling points requires a corresponding doubling of the acquisition time, if a constant  $BW$  is to be maintained. The consequences of this approach are a doubling of the total data collection time and a direct reduction of the per data point signal-to-noise ratio (SNR). Similarly, lowering the  $BW$  improves the SNR, as noise decreases as the square root of the bandwidth.

### 6.3. Phase Encoding

While the frequency-encoding process spatially encodes information in one in-plane direction of the image due to the resonance frequency dependence on  $B_{\text{eff}}$ , information in the second in-plane direction is encoded due to a shift in the phase of precessing nuclei that results from the application of a second magnetic field gradient. Equation (1.41) provides the relationship between the effective resonance frequency and the variables that comprise  $B_{\text{eff}}$ : the static  $B_0$  field, the strength of the magnetic field gradient applied along the slice-select axis  $G_z$ , and the position,  $z$ , of a nucleus along the  $z$ -axis. The spatially dependent frequency

offset from the Larmor frequency experienced by nuclei is, from Eq. (1.42), given by:

$$\Delta\nu = \frac{\gamma}{2\pi} G_y y \quad (1.45)$$

As a result, nuclei precess at different rates according to their position along the y-axis and, after exposed to the gradient for a period of time  $t$ , generate a phase shift,  $\Delta\phi$ , in the ensuing signal:

$$\Delta\phi = 2\pi\Delta\nu = \gamma G_y t \quad (1.46)$$

Since this phase-encoding gradient is not applied during the signal acquisition window, it does not affect the frequencies detected. However, the phase imparted to the nuclei will be retained and, from Eq. (1.46), is proportional to the gradient strength, its duration and the position of the nuclei along the y-axis.

In practice, a common approach to encoding information in the phase-encode dimension is to repeat the pulse sequence a number of times, dependent upon the desired spatial resolution of the final image, incrementing the amplitude of the phase-encode gradient with each iteration. The gradient increment value,  $G_{y,inc}$ , is chosen such that nuclei at the edge of the FOV in the phase-encode dimension ( $FOV_p$ ) experience a  $180^\circ$  phase change. Meeting this requirement means that spatial locations between the extents of the  $FOV_p$  have phase changes that are less than  $180^\circ$  per increment. Therefore, the phase-encode gradient increment is

dependent on the desired  $FOV_p$  and the phase-encode gradient duration,  $t$ , as given by:

$$G_{y,inc} = \frac{1}{\gamma FOV_p t} \quad (1.47)$$

The minimum and maximum extents of the phase-encoding gradient amplitudes can be determined from the total number of phase-encode steps and the parameter  $G_{y,inc}$ .

#### 6.4. Fourier Reconstruction

Having introduced the different approaches used to encode the NMR signal with information from the three spatial dimensions of the imaging sample, we next move on to discussing how that information is transformed into an image. The mathematical operation used to carry out this task is the Fourier transform (FT). As alluded to in Section 6.1 of this chapter, the FT operation interrogates a temporal signal for its frequency content and transforms that time-domain signal to a frequency-domain signal. For example, consider the time-dependent FID of Fig. 1.6. The FID may be described as an exponentially-decaying, sinusoidal signal in the time domain. Applying the FT to this signal yields a frequency domain signal that takes the form of a Lorentzian, as shown in Fig. 1.14. As discussed in Section 2 of this chapter, the sinusoidal component of the FID is convolved with an exponential decay function that is characterized by time constant  $T_2^*$ . This time constant characterizes the full-width at half-maximum (FWHM) of the Lorentzian curve in the frequency domain:  $FWHM = 1/\pi T_2^*$ .

Note that the information content of the two plots in Fig. 1.14 is identical; it is only the manner in which the information is presented that differs.

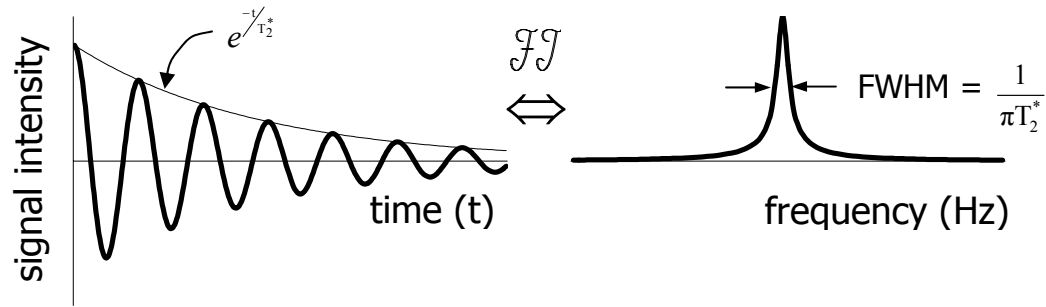


Figure 1.14 – The Fourier transform of the exponentially decaying, sinusoidal FID signal in the time domain is a Lorentzian waveform in the frequency domain. The exponential decay of the FID is characterized by the time constant  $T_2^*$ , which correspondingly characterizes the FWHM of the Lorentzian curve.

This processing method may be extended for case of data acquired in an imaging mode. As discussed in Sections 6.1 – 6.3, magnetic field gradients are used to encode spatial information in the NMR signal, yielding a 2-D dataset of spatial frequencies. Therefore, a 2-D FT is employed to reconstruct an image dataset. That is, the FT is applied along the frequency encode direction and along the phase encode direction of the dataset to yield a spatial image of signal amplitude versus position. In most NMR systems, processing of the digitized NMR signal is done using the fast-Fourier transform (FFT) algorithm.



## 6.5. Imaging Pulse Sequences

This section introduces a number of different pulse sequences used in MR imaging to demonstrate how RF pulses and magnetic field gradient pulses applied along the three orthogonal gradient axes interact to acquire the data needed to produce an MR image. The sequences introduced are the most fundamental pulse sequences used in MR imaging and include the gradient-recalled echo and the spin-echo imaging sequences as well as 3-D and echo-planar imaging acquisition methods. This information will provide a reference for the data-acquisition methods applied in the research topics that appear in subsequent chapters of this dissertation.

### 6.5.1. Spin-Echo Imaging

In Section 3 of this chapter we discussed the mechanics of the spin-echo (SE) formation through application of  $90^\circ$  and  $180^\circ$  RF pulses. This section introduces how this technique is combined with the application of magnetic field gradient pulses to encode spatial information in the acquired echo signal. The timing diagram for the SE imaging pulse sequence is provided in Fig. 1.15 and shows a  $90^\circ$  RF pulse, followed a period of time  $TE/2$  later by a  $180^\circ$  RF pulse. The spin-echo formation reaches its maximum amplitude a time interval  $TE/2$  after the  $180^\circ$  pulse (i.e., a total time interval  $TE$  after the  $90^\circ$  pulse). Note that slice-selective magnetic field gradient pulses are applied along the  $G_{\text{slice}}$  axis simultaneously with the RF pulses to selectively excite a particular volume of spins in the sample of interest, as discussed in Section 6.1 of this

chapter. The negative-lobed gradient pulse that appears following the  $90^\circ$  slice-select gradient is necessary in order to re-phase the dephasing effect of the slice-select gradient. A magnetic field gradient pulse along the  $G_{\text{phase}}$  axis is generally applied at some point between the  $90^\circ$  and  $180^\circ$  pulses. As discussed in Section 6.3, information in the phase-encode direction is acquired through iteration of the pulse sequence where the amplitude of the phase-encode gradient is incremented after each iteration. The total number of phase-encode steps,  $N_p$ , is generally a number that is a power of 2 (i.e., 64, 128, etc.) to facilitate implementation of the FFT algorithm during the image reconstruction processing. The time allotted for each iteration of the pulse sequence is referred to as the repetition-time (TR). During each TR period, the phase-encode gradient is advanced through one of the  $N_p$  total phase-encode steps; therefore, the total time necessary to acquire an imaging dataset is  $\text{TR} \times N_p$ . Along the frequency-encoding axis,  $G_{\text{freq}}$ , an initial magnetic field gradient is applied simultaneously with the phase-encode and slice-rephasing gradients. The purpose of this gradient is to dephase transverse magnetization prior to application of the frequency-encode gradient during the spin-echo formation, thus counteracting the dephasing effects of the frequency-encode gradient and this gradient pulse is often referred to as a pre-dephasing gradient. Further information regarding frequency encoding is found in Section 6.2 of this chapter.

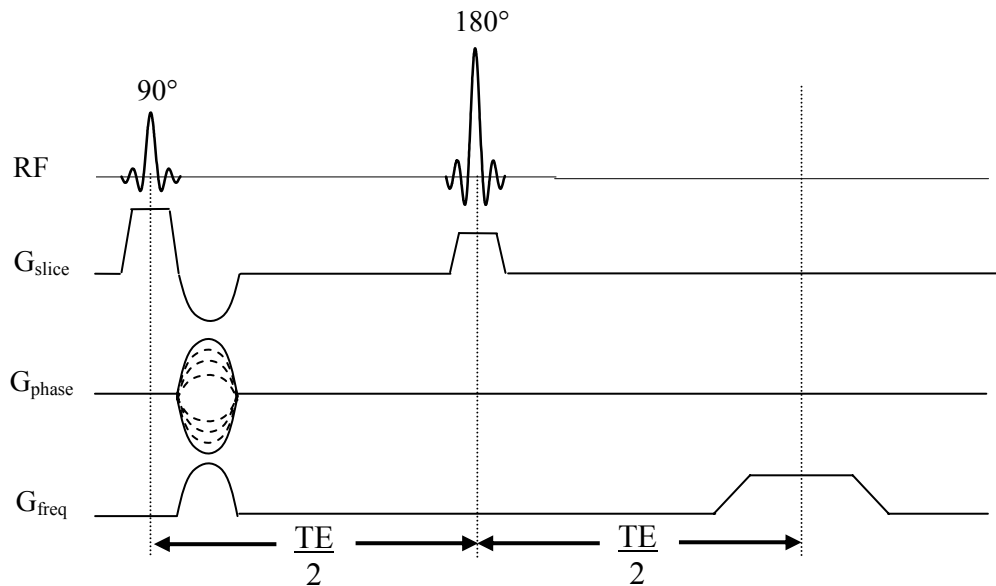


Figure 1.15 – Timing diagram of the spin-echo sequence with imaging gradients. Slice-selective RF excitation pulses are applied a period of time  $TE/2$  apart simultaneously with magnetic field gradient pulses along the slice-select gradient axis. Timing of the corresponding frequency- and phase-encode gradient pulses is also shown. The dashed lines of  $G_{\text{phase}}$  imply that consecutive iterations of the sequence are acquired using a range of different gradient amplitudes.

### 6.5.2. Gradient Recalled Echo Imaging

The gradient-recalled echo (GRE) imaging pulse sequence, Fig. 1.16, employs a single RF excitation pulse followed by the phase- and the frequency-encode gradient pulses. Echo formation at time  $TE$  after application of the RF excitation pulse is generated in the GRE sequence through application of a magnetic field gradient. As shown on the  $G_{\text{freq}}$  axis of Fig. 1.16, prior to applying the read-out gradient, a magnetic field gradient pulse of opposite phase is applied to dephase transverse magnetization. The amount of spin dephasing is proportional to the duration and magnitude of this dephasing gradient. Reversal of the phase

of  $G_{\text{freq}}$  during the read-out gradient refocuses the magnetization, such that total rephasing (i.e., the point where the echo signal reaches its maximum amplitude) occurs at time TE after the initial RF excitation pulse. The flip angle,  $\theta$ , of the RF excitation pulse in the GRE sequence is generally some value much less than  $90^\circ$ . The absence of a  $180^\circ$  RF pulse allows the minimum TE of a GRE sequence (i.e., on the order of 5 msec) to be much shorter than that of a SE sequence. The short TE and low flip angle also allows the sequence repetition-time to also be very short (i.e., less than 10 msec), enabling very rapid image acquisitions. The gradient-echo generated with this pulse sequence does not refocus the static dephasing effects of intrinsic magnetic field inhomogeneities as the  $180^\circ$  RF pulse of a SE sequence will. Transverse magnetization will therefore rapidly decay by the relaxation time constant  $T2^*$ , however, these effects are somewhat mitigated by the short TE values used in GRE sequences. In all other respects, the general GRE imaging sequence is identical to the SE pulse sequence.

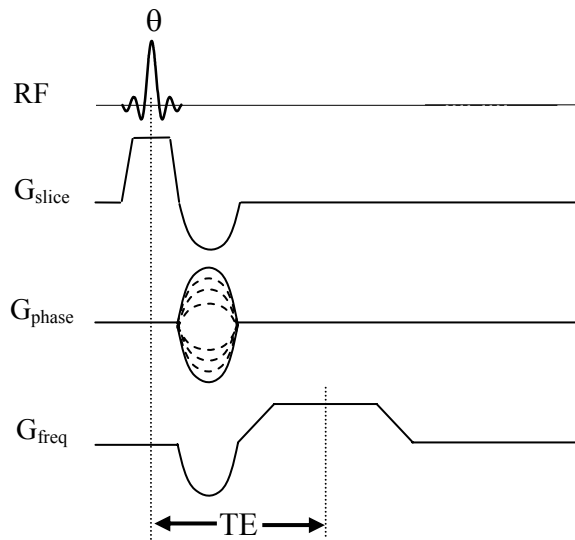


Figure 1.16 – Timing diagram of the gradient-recalled echo sequence with imaging gradients. Echo formation at time TE after application of the RF excitation pulse is generated with a magnetic field gradient. Prior to the frequency-encode gradient, a magnetic field gradient pulse of opposite phase is applied to dephase transverse magnetization. Subsequent application of the read-out gradient refocuses the magnetization, producing a gradient-echo at time TE after the initial RF excitation pulse.

### 6.5.3. 3-D Image Acquisition

With the conventional pulse sequences described in the preceding sections, two-dimensional spatial information is encoded in the acquired signal. The third dimension, the slice-selection dimension, is obtained through the slice-selective RF pulse. For 3-D image acquisition, the third dimension is encoded in the acquired echo signal through use of an additional phase-encode gradient. An example of this modification implemented with a SE imaging pulse sequence is provided in Fig. 1.17, where the third dimension is encoded with the gradient line labeled  $\phi$ -encode (slice). When the sequence is executed, the phase-encoding

iterations of one dimension [say, the in-plane  $\phi$ -encode (image)] are nested within the phase-encoding iterations of the second dimension [the thickness  $\phi$ -encode (slice)]. As one might imagine, the size of the data array acquired through 3-D image acquisition can become quite large, depending on the number of steps in the second phase-encoding dimension.

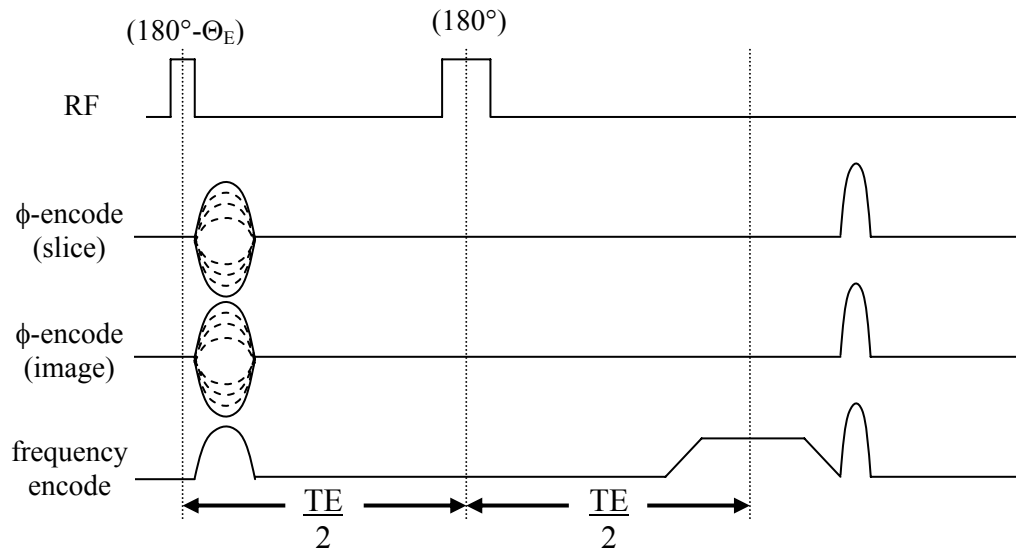


Figure 1.17 – Timing diagram of the spin-echo sequence with 3-D image acquisition. The third dimension of the acquisition matrix is filled by means of an additional phase-encoding gradient such that when executed, one phase-encode direction is nested within the other. As with the conventional 2-D SE sequence, maximum amplitude of the echo formation occurs at time TE after application of the initial RF pulse. This diagram illustrates the use of a partial flip angle excitation as implemented in SE mode whereby the flip angle of the initial RF pulse is  $180^\circ - \Theta_E$ . Following the acquisition period, crusher gradients are often applied along all three gradient axes to dephase residual transverse magnetization prior to the subsequent iteration of the sequence.

One of the positive attributes to performing all of the sequence iterations necessary to fill a 3-D acquisition matrix is the increased number of independent measurements of a single voxel relative to a conventional

slice-selective 2-D acquisition. This translates into a signal averaging effect, resulting in a relative increase in SNR by the square root of the number of slice-dimension phase-encoding steps over that of the conventional 2-D acquisition. The primary drawback to performing all the necessary iterations of a 3-D acquisition, however, is that the total data acquisition time needed to encode the entire matrix is often prohibitively long. Therefore, the number of steps in the second phase-encode dimension is often reduced from that of the first phase-encode dimension. Even given this reduction in spatial resolution, scan times can be exceedingly long if a SE sequence is employed in 3-D mode.

One method for decreasing the total scan time of a 3-D image acquisition is to implement the sequence using partial flip angle excitation. With this approach, the initial RF excitation pulse does not rotate the entire net magnetization vector into the transverse plane as in a conventional SE sequence. Instead, a greater portion of the magnetization is left along the longitudinal axis, which means less recovery time (i.e., shorter TR) is needed for  $T_1$  relaxation processes to restore longitudinal magnetization to equilibrium. A flip angle that maximizes SNR for a given set of experimental conditions may be calculated based on the pulse interval (i.e., TR) and  $T_1$  time constant of the sample. This optimum flip angle is referred to as the Ernst angle,  $\Theta_E$ , and is given by the expression:

$$\Theta_E = \cos^{-1} e^{-TR/T_1} \quad (1.48)$$

Implementation of the 3-D acquisition with a SE pulse sequence, as shown in Fig. 1.17, the initial RF excitation pulse is a pulse with flip angle  $(180^\circ - \Theta_E)$  (Winkler *et al.*, 1988). The spin manipulations that ensue are depicted in Fig. 1.18. The initial RF excitation pulse rotates the net magnetization  $(180 - \Theta_E)^\circ$  about the x-axis such that its z-component is aligned along the  $(-z)$ -axis. A  $180^\circ$  pulse follows after a time period  $TE/2$ , restoring the longitudinal magnetization back along the  $(+z)$ -axis. The  $180^\circ$  pulse also allows magnetization in the transverse plane to refocus in the same manner as a conventional SE sequence. Prior to a subsequent iteration of the pulse sequence, a delay period follows the echo formation to allow  $T_1$  relaxation to restore the longitudinal magnetization to  $M_0$ .

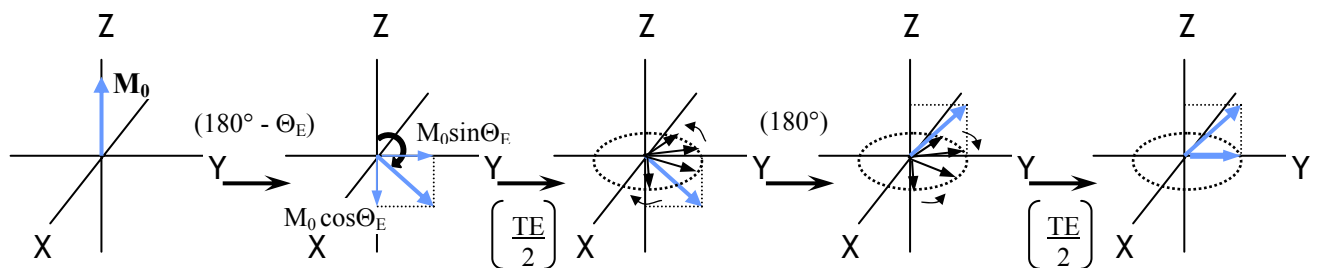


Figure 1.18 – Manipulation of the net magnetization vector,  $M_0$ , following partial flip angle RF excitation as implemented with a SE sequence. The initial RF pulse rotates the net magnetization  $(180 - \Theta_E)^\circ$  about the x-axis such that its z-component is aligned along the  $-z$ -axis. A  $180^\circ$  pulse follows after a time period  $TE/2$ , restoring the longitudinal magnetization back along the  $+z$ -axis. The  $180^\circ$  pulse also allows magnetization in the transverse plane to refocus in the same manner as a conventional SE sequence. Prior to a subsequent iteration of the pulse sequence, a delay period follows the echo formation to allow  $T_1$  relaxation to restore the longitudinal magnetization to  $M_0$ .



#### 6.5.4. Echo-Planar Imaging

The echo-planar image (EPI) acquisition method (Mansfield, 1977) is an ultra-high-speed MR imaging technique. This method decreases the total image acquisition time from that of conventional methods by an order of magnitude or more, enabling image data acquisitions of  $< 100$  msec. As opposed to the conventional spin-warp acquisition approach, where the total acquisition time is dependent upon the desired resolution in the phase-encode direction (i.e., the total number of phase-encode steps,  $N_p$ , as discussed in Section 6.5.1), the EPI acquisition scheme collects all the frequency and phase information after a single RF excitation (an acquisition scheme that is often referred to as ‘single-shot’ imaging). After the RF excitation, a series of echoes, each with a different degree of phase encoding, are quickly and repetitively refocused and sampled. A number of approaches to performing single-shot EPI acquisitions have been developed, the primary distinction between them being the manner in which the frequency and phase information is encoded. One relatively straightforward approach used to map this information is referred to as blipped-EPI. Figure 1.19 diagrams the use of this approach coupled with slice-selective gradient-echo excitation. On the phase-encode axis, an initial gradient pulse dephases magnetization, which is then partially rephased with each successive gradient blip. A gradient-echo forms after each gradient blip applied along the  $G_{\text{phase}}$  axis that is encoded with a read-

out gradient pulse on the frequency-encode axis. This process is repeated for the chosen number of phase-encode steps.

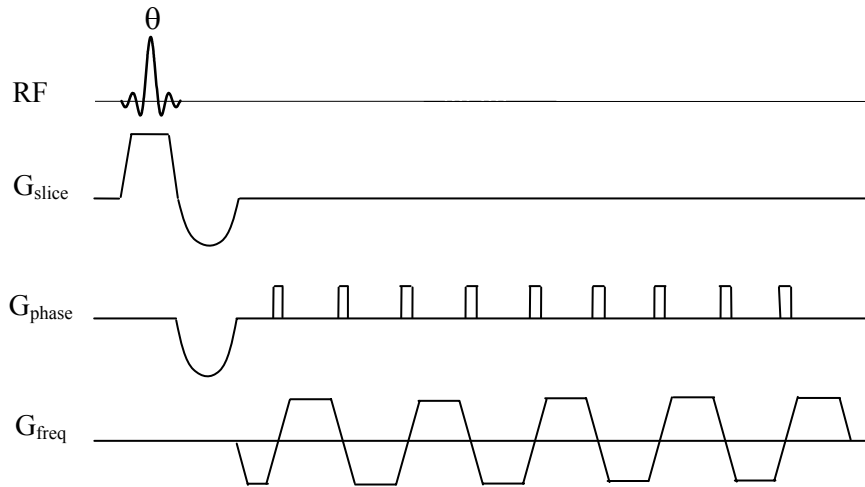


Figure 1.19 – Timing diagram of the gradient-recalled echo sequence, implemented with blipped-EPI acquisition. In this acquisition scheme, an initial gradient pulse is applied along the phase-encode axis to dephase magnetization along that axis. With a series of successive gradient pulse blips along this axis, magnetization partially rephases and a gradient-echo forms. A read-out gradient pulse on the frequency-encode axis encodes the echo after each  $G_{\text{phase}}$  gradient blip.

# Chapter 2

## NMR Measurement of Water Diffusion in Biological Tissue

---

### The Diffusion Process

- Brownian Motion

- Fick's Laws of Diffusion

### Diffusion in Biological Systems

- Restricted Diffusion

- Tortuosity of Diffusion

- Diffusion Anisotropy

### NMR Measurement of Diffusion

- Pulsed Field Gradient Method

- Stimulated Echo Diffusion Imaging

- Diffusion Tensor Imaging

  - Acquisition Schemes

  - Metrics of Diffusion Isotropy

  - Metrics of Diffusion Anisotropy

---

This chapter provides an introduction to the NMR measurement of the diffusion of water molecules in biological tissues. Diffusion measurements can be made with NMR in a spectroscopic mode as well as in an imaging mode. A unique attribute of molecular diffusion that makes it a parameter of interest is the fact that the diffusion process directly reflects translational molecular motion. The effects of molecular motion (predominately rotational motions) are also reflected in the NMR relaxation parameters  $T_1$  and  $T_2$ , but these are parameters that are dependent upon conditions such as the magnetic field strength of the NMR instrument. Molecular diffusion, however, is not an intrinsic NMR parameter and is therefore independent of such conditions. Parameters inferred from the diffusion of water molecules in biological tissues have found a broad range of applications spanning from basic science research to clinical radiology. Diffusion processes are inherent to both of the research topics presented in this dissertation. In the work with static tensile loading of tendon tissue, differences in the diffusion parameters between unloaded and loaded tendon reflect the reorganization of the tendon collagen fibers that occurs with loading. In the human fMRI work, the mechanism of signal changes observable after neural activation is primarily considered to be the result of diffusion processes.

## 1. The Diffusion Process

### 1.1. Brownian Motion & The Physical Model of Diffusion

Brownian motion is the random translational motion of particles driven by ambient thermal energy. The physical model of diffusion is one of successive small, random steps that comprise what is referred to as a random-walk pattern. Each step in the random walk may be thought of as a vector with magnitude and

direction components that are unrelated to those of preceding steps. If we consider a homogeneous water bath of infinite extent, the probability of a single water molecule moving in a particular direction is equivalent to that of any other direction. Therefore, on average, after a large number of individual steps, there will be no net displacement of a molecule from its starting location. However, there will be a region around the starting location within which the molecule can be expected to be located at any one time. Considering a large population of molecules in the homogeneous water bath, the distribution of displacements over a given period of time takes a Gaussian form with mean of zero and standard deviation proportional to the average displacement of the population. The dependence of the displacement distribution on the duration of diffusion (i.e., the diffusion time,  $t_{\text{dif}}$ ) is defined by the Einstein relationship:

$$\langle (r - r')^2 \rangle = 2nD_0t_{\text{dif}} \quad (2.1)$$

where  $\langle (r - r')^2 \rangle$  represents the mean-squared displacement of the population,  $n$  represents the number of dimensions in which molecules are able to diffuse, and  $D_0$  is the proportionality constant referred to as the free diffusion coefficient. Figure 2.1 depicts the condition of freely diffusing molecules in a single direction. The displacement distributions shown reflect the diffusion-time-dependence of the free diffusion process for three different durations. An increase in the time allowed for diffusion results in a correspondingly larger mean-squared displacement for the population.

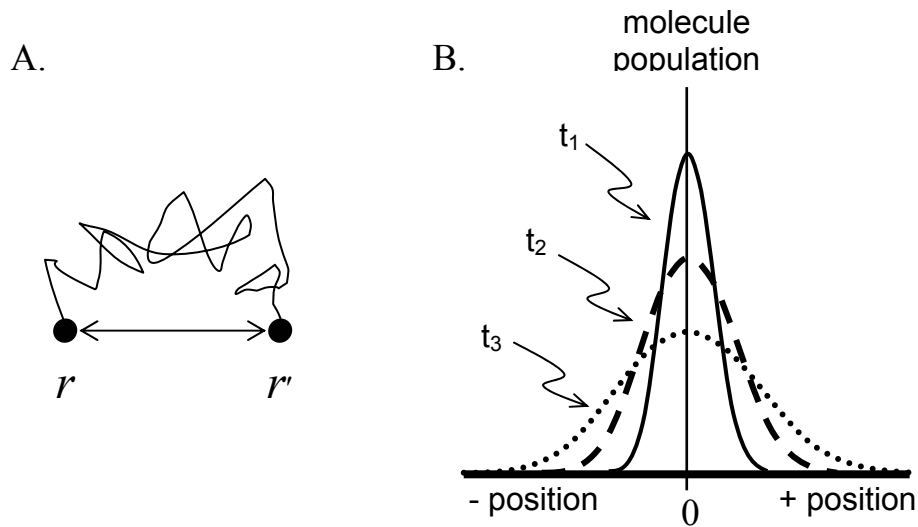


Figure 2.1 – For the case of diffusion in a single dimension, the mean-squared displacement between position  $r$  and position  $r'$  (A.) is predicted from the Einstein relation:  $\langle (r - r')^2 \rangle = 2D_0 t_{\text{dif}}$ . (B.) One-dimensional displacement distributions of a freely diffusing population of molecules originating at position 0 at time  $t=0$  reflect the Gaussian nature of the free diffusion process. Distributions for three different diffusion durations, where  $t_1 < t_2 < t_3$ , are shown. The standard deviation of the distribution is proportional to the average molecular displacement for a given diffusion time.

## 1.2. Fick's Laws of Diffusion

The process of diffusion may also be viewed from a perspective that differs from the random-walk approach. Fick's laws model diffusion as a transport process driven by concentration gradients. Fick's first law is commonly used to describe transport by free diffusion (i.e., diffusion in an isotropic and homogeneous medium). That is, it describes the flux of particles across some arbitrary plane at an instant in time and characterizes diffusion as a process that balances out concentrations of particles in the medium over time. Barring any opposing force, the net flux of particles in a solution will be from a region of high concentration to one that is more dilute. In mathematical terms, Fick's first law states that the

flux of particles,  $\mathbf{J}$ , at position  $\mathbf{r}$  over a period of time is directly proportional to the gradient of the solute concentration,  $\nabla c(\mathbf{r}, t)$ , at that position:

$$\mathbf{J}(\mathbf{r}, t) = -D\nabla c(\mathbf{r}, t) \quad (2.2)$$

where the proportionality constant,  $D$ , is the diffusion coefficient. Diffusion within a homogeneous solution is assumed to be isotropic and can therefore be described by the scalar diffusion coefficient  $D$ . Under more general conditions where diffusion occurs in an anisotropic medium, the diffusion process is represented by the  $3 \times 3$  Cartesian tensor  $\mathbf{D}$  and Fick's first law written for the more general case is:

$$\mathbf{J}(\mathbf{r}, t) = -\mathbf{D}\nabla c(\mathbf{r}, t) \quad (2.3)$$

In general, for *in vivo* and *in vitro* work such as that presented in subsequent chapters of this dissertation, where the molecular species of interest is an uncharged molecule such as water,  $\mathbf{D}$  is a symmetric tensor (i.e.,  $\mathbf{D} = \mathbf{D}^T$ ) (Stejskal, 1965; Basser *et al.*, 1994).

Leading to the development of Fick's second law of diffusion, it is assumed that the number of particles within the volume of interest is conserved; therefore, the continuity theorem applies. The change in concentration at position  $\mathbf{r}$  at any point in time is expressed as a function of the flux of particle through that point:

$$\frac{\partial c(\mathbf{r}, t)}{\partial t} = -\nabla \cdot \mathbf{J}(\mathbf{r}, t) \quad (2.4)$$

Combining Eqs. (2.3) and (2.4) leads to the expression for Fick's second law of diffusion:

$$\frac{\partial c(\mathbf{r}, t)}{\partial t} = \nabla \cdot \mathbf{D} \nabla c(\mathbf{r}, t) \quad (2.5)$$

In the NMR experiment, we are interested in the case of self-diffusion where there is no net concentration gradient. Therefore, instead of representing Fick's laws in terms of a concentration function, they may be expressed in terms of the conditional probability of finding a particle at a given position at a given time. From this, it can be shown that the solution to Fick's second law for molecules experiencing free diffusion in an isotropic, homogeneous medium takes the form of a Gaussian probability density function,  $P(r, r', t_{\text{dif}})$ :

$$P(r, r', t_{\text{dif}}) = \frac{1}{\sqrt{(4\pi D t_{\text{dif}})^3}} \exp\left(\frac{-(r - r')^2}{4 D t_{\text{dif}}}\right) \quad (2.6)$$

which expresses the conditional probability of finding a given molecule initially at position  $r$  between positions  $r'$  and  $r' + dr'$  after a duration of diffusion  $t_{\text{dif}}$ .

Note in this equation that  $P(r, r', t_{\text{dif}})$  does not depend on the initial position  $r$  but instead the net displacement,  $(r - r')$ . This expression is often referred to as the diffusion propagator.



## 2. Diffusion in Biological Systems

In a homogeneous fluid of infinite extent, diffusion may be a truly random process with no preferred directionality to the spatial drift of molecules. In biological tissue, however, molecular mobility may not be the same in all directions as the extent to which molecules diffuse is affected by the properties of the cytosol and the presence of cellular structures that provide barriers to free movement. The implications of these issues are important considerations when performing molecular diffusion experiments in biological systems.

### 2.1. Restricted Diffusion

In most biological systems, because there is always some fraction of water molecules whose motion is restricted, for even short  $t_{\text{dif}}$ , the mean-squared displacement is usually reduced from that predicted by the Einstein relation of Eq. (2.1). The degree of restriction experienced by diffusing molecules will depend on the time they are allowed to probe the surrounding environment and as a result, the measured diffusion coefficient is diffusion-time dependent. This diffusion-time dependent parameter is referred to as the apparent diffusion coefficient (ADC or  $D_{\text{app}}$ ) and replaces the free diffusion coefficient of Eq. (2.1) to leave:  $\langle (r - r')^2 \rangle = 2nD_{\text{app}}t_{\text{dif}}$ .

In an environment with restrictions to diffusion, it is therefore evident that the value of the diffusion-time dependent ADC will always be reduced from that of the free diffusion coefficient,  $D_0$ . Structural information about the system under investigation can be obtained from the short  $t_{\text{dif}}$  behavior of the  $\text{ADC}(t_{\text{dif}})$  curve

in terms of the ratio of surface area to diffusing volume,  $S/V$ . Mitra *et al.* (1992, 1993) have shown that in the short  $t_{\text{dif}}$  regime,  $\text{ADC}(t_{\text{dif}})$ , normalized by  $D_0$ , may be expressed as:

$$\frac{\text{ADC}(t_{\text{dif}})}{D_0} = 1 - \frac{4}{9\sqrt{\pi}} \frac{S}{V} \sqrt{D_0 t} \quad (2.7)$$

where  $(S/V)$  is the average surface-area to volume ratio of the space available for diffusion. The general form of Eq. (2.7) is a linear equation with intercept  $D_0$  and slope  $\propto (S/V)$ ; therefore, the initial slope of a plot of  $\text{ADC}$  vs.  $t_{\text{dif}}^{1/2}$  will reflect the surface-area to volume ratio of the system under investigation.

Calculation of  $(S/V)$  through Eq. (2.7), however, requires that  $D_0$  be known. In general, experimental determination of  $D_0$  is often difficult in biological systems. Note, however, that the limit of  $\text{ADC}(t_{\text{dif}}) \rightarrow D_0$  as  $t_{\text{dif}} \rightarrow 0$ , which implies that extrapolating the linear fit of the initial time points of  $\text{ADC}$  vs.  $t_{\text{dif}}^{1/2}$  to the zero-time intercept will yield an estimate of  $D_0$ .

## 2.2. Tortuosity of Diffusion

In a medium with barriers to the diffusion of water, increasing the duration that molecules are allowed to diffuse increases the portion of the confining geometry they are able to probe. In the regime where the diffusion-time dependent  $\text{ADC}$  has reached a constant value, i.e. where the  $\text{ADC}$  vs.  $t_{\text{dif}}^{1/2}$  plot is no longer diffusion-time dependent, each of the diffusing molecules have probed over a length scale larger than the characteristic length scale of the restricting space and the  $\text{ADC}$  is said to have reached the effective diffusion regime,  $D_{\text{eff}}$ , which

reflects the tortuosity,  $T$ , of the medium. The tortuosity is a measure of the long-range connectivity of the space available for diffusion in a given direction through the medium.  $D_{\text{eff}}$  is reduced from the free diffusion coefficient,  $D_0$ , by the tortuosity such that:

$$D_{\text{eff}} = D_0/T. \quad (2.8)$$

### 2.3. Diffusion Anisotropy

As alluded to in the discussion of Fick's first law of diffusion in Section 1.2 of this chapter, diffusion coefficients in a non-homogenous medium can often be directionally dependent. Anisotropic diffusion arises in samples with highly oriented barriers. Excised muscle or nerve fibers are common biological samples used to demonstrate anisotropic diffusion. In these tissues, the larger diffusion coefficient measured along the direction parallel to the long axis of the muscle or nerve fibers relative to the perpendicular direction reflects the larger molecular displacements along the parallel direction. The ADC may be expressed as a symmetric tensor (i.e.,  $\mathbf{ADC}_{ij} = \mathbf{ADC}_{ji}$  with  $i, j = x, y, z$ ) to characterize diffusion throughout the medium of interest in a regular Cartesian coordinate system:

$$\mathbf{ADC} = \begin{bmatrix} \text{ADC}_{xx} & \text{ADC}_{xy} & \text{ADC}_{xz} \\ \text{ADC}_{xy} & \text{ADC}_{yy} & \text{ADC}_{yz} \\ \text{ADC}_{xz} & \text{ADC}_{yz} & \text{ADC}_{zz} \end{bmatrix} \quad (2.9)$$

Discussion of the diffusion tensor and the information it contains will continue in Section 3.2 of this chapter.

### 3. NMR Measurement of Diffusion

The work of Stejskal and Tanner (1965) introduced the use of short magnetic field gradient pulses as a method of sensitizing the NMR spin-echo experiment to molecular diffusion. Since that time, the method has been implemented as an imaging mode acquisition (i.e., diffusion-weighted imaging, DWI) (Taylor *et al.*, 1985) and the advent of DWI to the realm of biological systems (Le Bihan *et al.*, 1986) has proved to be an important contrast parameter in the diagnostic utility of MRI. In contrast to classical methods of measuring diffusion, the NMR method directly detects net molecular displacements of an ensemble of spins. From the measures of displacement, the diffusion coefficient is then inferred from the linear relationship between the mean-squared displacement of an ensemble of diffusing molecules and the time allowed for diffusion, as expressed by the Einstein relationship of Eq. (2.1). The sections that follow describe the details of how magnetic field gradients are used to encode translational diffusion of molecules in the NMR signal.

#### 3.1. Pulsed Field Gradient Method

The pulsed field gradient (PFG) method of diffusion measurement employs a pair of magnetic field gradients to encode the NMR signal with molecular diffusion information. In this method, a magnetic field gradient pulse encodes spins with a spatially-varying resonant frequency. Those spins positioned in a region exposed to a strong magnetic field will have a higher resonant frequency relative to those in a weak magnetic field and, therefore, accumulate a phase offset from the spins in the weaker magnetic field. For spins that randomly translate from one field

value to another, their precessional frequency changes and, over time, so does their accumulated phase relative to stationary spins. Due to the random distribution of acquired phases (i.e., degree of phase dispersion), destructive interference of the ensemble of phase-dispersed spins results, attenuating the overall signal.

In terms of specific features of the pulse sequence that produces diffusion-weighting in the acquired data, refer to the pulse sequence timing diagram shown in Fig. 2.2. Each diffusion gradient pulse of magnitude  $g$  is applied for a duration  $\delta$  and the temporal separation between them is denoted by  $\Delta$ . The initial  $90^\circ$  RF pulse creates coherent magnetization in the transverse plane and the initial diffusion gradient pulse induces a spatially dependent phase shift to the spins. The sign of the phase shifts are reversed by the subsequent  $180^\circ$  RF pulse. If the spins diffuse during the time interval  $\Delta$  between diffusion gradients, they will likely experience a net displacement from their place of origin,  $r_0$ , to some position  $r'$  at the time of the second gradient pulse. If this displacement is along the direction of the applied diffusion gradient pulse, the phase imparted by the first gradient pulse will not be completely negated, leaving those spins with a net phase shift. Signal from spins left with a net phase shift due to the effects of diffusion will not completely refocus at the echo time, which will manifest itself in an attenuation of the echo signal that is a function of the molecular diffusion coefficient. In contrast, for static spins, the second gradient pulse completely

compensates for the effect of the first gradient pulse, leaving the echo signal attenuated only by standard relaxation mechanisms rather than diffusion effects.

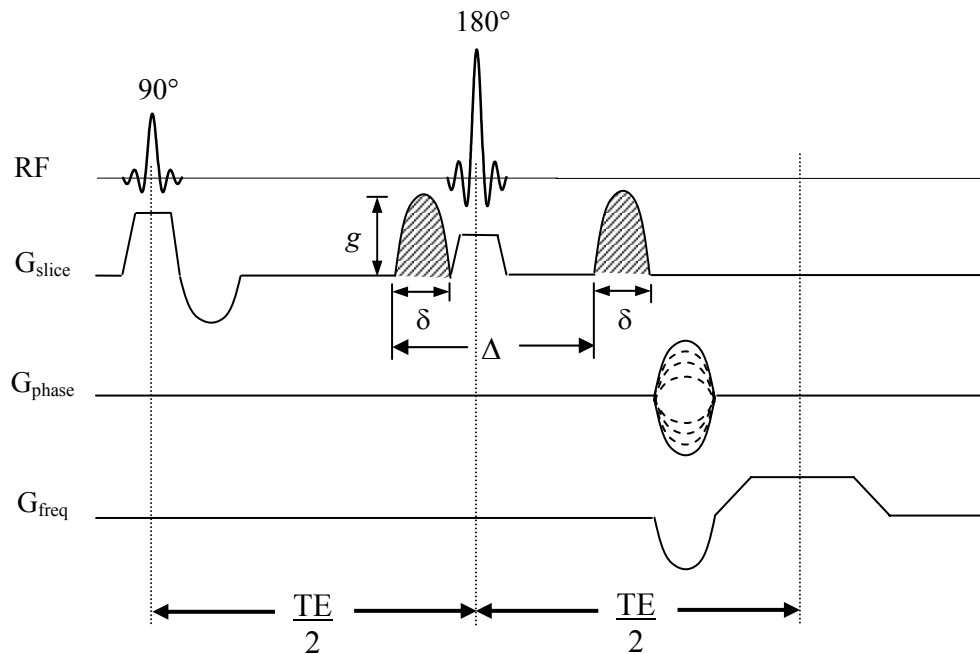


Figure 2.2 – Timing diagram of the pulsed-field-gradient method for diffusion weighting implemented into a spin-echo imaging sequence (PFG-SE). Diffusion gradient pulses are shown applied along the  $G_{\text{slice}}$  axis with magnitude  $g$ , for a duration  $\delta$  and the temporal separation between them is denoted by  $\Delta$ . The initial  $90^\circ$  RF pulse creates coherent magnetization in the transverse plane and the initial diffusion gradient pulse induces a spatially-dependent phase shift to the spins. The sign of the phase shifts are reversed by the subsequent  $180^\circ$  RF pulse. Molecules that diffuse from their original position in the direction of the applied diffusion gradient during the time period  $\Delta$  will be left with a net phase shift that causes attenuation of the spin-echo signal.

The dependence of the NMR signal on molecular diffusion in the pulse sequence described in Fig. 2.2 is a function of the diffusion weighting term,  $b$ , and can be expressed (Le Bihan *et al.*, 1986) in terms of the ADC as (neglecting the effects of imaging gradients):

$$S(\mathbf{b}) = S_0 \exp(-\mathbf{bADC}) \quad (2.10)$$

where  $S_0$  is the signal intensity with no diffusion weighting (i.e.,  $\mathbf{b} = 0$ ) and the  $\mathbf{b}$ -value characterizes the timing, amplitude and shape of the applied diffusion gradient pulses. Using a pair of half-sine shaped diffusion gradient pulses as shown in Fig. 2.2, the  $\mathbf{b}$ -value may be expressed as:

$$\mathbf{b} = \gamma^2 \delta^2 g^2 \frac{4}{\pi^2} \left( \Delta - \frac{\delta}{4} \right) \quad (2.11)$$

where  $\gamma$  is the gyromagnetic ratio,  $g$  is the diffusion gradient pulse amplitude,  $\delta$  is the diffusion gradient pulse duration and  $\Delta$  is the time interval between rising edges of the two diffusion gradient pulses. The quantity  $(\Delta - \delta/4)$  is referred to as the diffusion-time,  $t_{\text{dif}}$ . Using the PFG-SE imaging sequence of Fig. 2.2, the ADC from Eq. (2.10) may be calculated for the image on a pixel-by-pixel basis from a series of image acquisitions, each with a different  $\mathbf{b}$ -value weighting. In practice, the  $\mathbf{b}$ -value is varied by incrementing the amplitude  $g$  of the diffusion gradient pulses. Using a linear least-squares regression algorithm, the natural log of the signal intensity can be fitted as a function of  $\mathbf{b}$ -value where the slope of the fitted line yields the ADC value. Applying this procedure to each pixel in an image yields a map of ADC values.

### 3.2. Stimulated Echo Diffusion-Weighted Imaging

In addition to the SE pulsed field gradient pulse sequence, diffusion-weighted acquisitions may be acquired with a stimulated echo pulsed field gradient (PFG-STE). The PFG-STE sequence is comprised of three RF pulses and standard

imaging and diffusion weighting gradient pulses, as shown in Fig. 2.3. The three RF pulses used with a STE sequence are most often  $90^\circ$  pulses and are separated by time intervals ( $TE/2$ ) and  $TM$  (subsequent chapters of this dissertation discuss applications of this pulse sequence employing  $90^\circ$  pulses; therefore, the discussion that follows assumes  $90^\circ$  pulses). The stimulated echo forms at time ( $TE/2$ ) after the third RF pulse. After the second RF pulse, part of the transverse magnetization is oriented along the longitudinal axis. During the  $TM$  interval that follows, the longitudinal magnetization experiences  $T_1$  relaxation (refer to Section 5.1 of Chapter 1 of this dissertation for details on longitudinal magnetization decay by  $T_1$  relaxation). This feature of the pulse sequence is particularly advantageous when investigating samples with short  $T_2$ - and long  $T_1$ -relaxation time constants, as is often the case with biological tissue. Since diffusion sensitizing gradient pulses are applied before the second and after the third RF pulse, the temporal separation between the diffusion gradient pulses is determined by the  $TM$  interval, enabling diffusion measurements that require long diffusion times. In contrast, diffusion time duration in the PFG-SE sequence is determined through the ( $TE/2$ ) interval. For samples with short  $T_2$ , long diffusion time measurements with the PFG-SE sequence may not be feasible due to magnetization decay by  $T_2$  relaxation. A negative feature of the PFG-STE sequence is the reduction in signal intensity relative to an acquisition with a PFG-SE sequence. This aspect of the sequence is due to fact that the second RF pulse will not orient all the transverse magnetization along the longitudinal axis,



therefore not all the transverse magnetization generated from the first RF pulse will contribute to the echo formation.

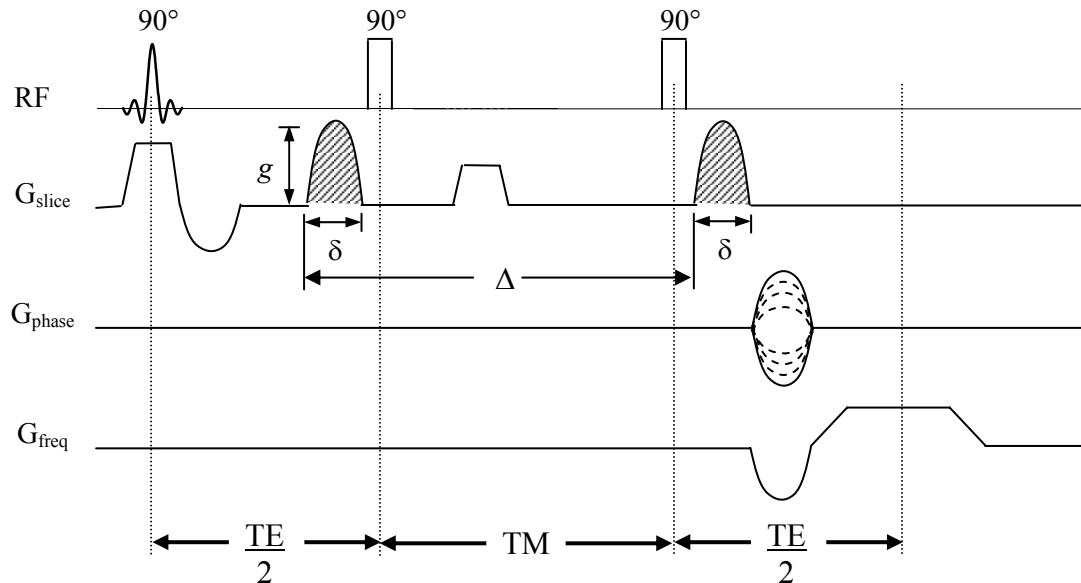


Figure 2.3 – Timing diagram of the pulsed-field-gradient method for diffusion weighting implemented into a stimulated-echo imaging sequence (PFG-STE). As with the PFG-SE sequence, diffusion gradient pulses are shown applied along the  $G_{\text{slice}}$  axis with magnitude  $g$ , for a duration  $\delta$  and the temporal separation between them is denoted by  $\Delta$ . The fundamental difference between this and the PFG-SE sequence is that the second RF pulse stores transverse magnetization along the longitudinal axis during the  $TM$  interval. The longitudinal magnetization experiences  $T_1$  relaxation during this interval and, since  $T_1 \gg T_2$  for biological tissues, the diffusion time ( $\Delta - \delta/4$ ) may be made very long relative to the PFG-SE sequence through the  $TM$  interval.

### 3.3. Diffusion Tensor Imaging

As discussed above, molecular displacements due to diffusion are encoded in the NMR signal using magnetic field gradient pulses. Those displacements that occur along the direction of the applied gradient will attenuate the signal. Diffusion anisotropy can therefore be detected by comparing measurements acquired with diffusion gradients applied in multiple directions over the sample.

The concept of a directional dependence associated with molecular diffusion has been formalized in the work of Basser *et al.* and has led to the development of diffusion tensor imaging (DTI) (Basser *et al.*, 1994a; 1994b).

An equivalent expression to Eq. (2.10) that incorporates the diffusion tensor,  $\mathbf{D}$ , and weighting matrix,  $\mathbf{b}$ , may be written as:

$$S(\mathbf{b}) = S_0 \exp\left(-\sum_{i,j=1}^3 b_{ij} D_{ij}\right) \quad (2.12)$$

where  $D_{ij}$  are elements of the diffusion tensor,  $\mathbf{D}$ , and  $b_{ij}$  are elements of the weighting matrix. The elements of the weighting matrix characterize the timing, amplitude and shape of all the applied magnetic field gradient pulses used to encode spatial information and diffusion effects in the NMR signal. Accurate determination of the elements of the weighting matrix is necessary for accurate calculation of the corresponding elements of the diffusion tensor (Mattiello *et al.*, 1994; 1997).

### 3.3.1. Acquisition Schemes

Various data acquisition schemes have been employed to enable determination of the full diffusion tensor (Mori *et al.*, 1995; Wong *et al.*, 1995; Conturo *et al.*, 1996; Papadakis *et al.*, 1999). For a given sample with unknown structure, the idea is to apply diffusion gradients with equal amplitude along several directions to cover a uniform orientational distribution through the sample so as not to bias the observed molecular

displacements along any one direction. The diffusion tensor is symmetric (i.e.,  $D_{ij} = D_{ji}$ , with  $i, j = x, y, z$ ), therefore, there are six independent elements in  $\mathbf{D}$  and the acquisition scheme must apply diffusion gradients along at least six noncollinear directions in order to generate adequate information to estimate the independent elements of  $\mathbf{D}$ . Methods have been developed where fewer than six directions are used to characterize  $\mathbf{D}$ , however, they generally assume axial symmetry in the sample (Conturo *et al.*, 1996). Given analytical expressions for elements of  $\mathbf{b}$ , the signal intensity of Eq. (2.12) may be written with  $\mathbf{b}$  separated into its scalar constants and a vector  $\mathbf{G}$  representing the applied gradient amplitude along the x, y, and z directions such that  $\mathbf{G} = (g_x, g_y, g_z)$ . One such acquisition scheme has been suggested by Basser *et al.* (1998) which performs diffusion-weighting over six directions defined by the following gradient vectors that contain the relative weighting of the applied gradient along the x, y, and z directions for each acquisition:

$$\mathbf{G}(g_x, g_y, g_z): \quad \left( \frac{\sqrt{2}}{2}, 0, \frac{\sqrt{2}}{2} \right); \left( -\frac{\sqrt{2}}{2}, 0, \frac{\sqrt{2}}{2} \right); \left( 0, \frac{\sqrt{2}}{2}, \frac{\sqrt{2}}{2} \right); \quad (2.13)$$

$$\left( 0, \frac{\sqrt{2}}{2}, -\frac{\sqrt{2}}{2} \right); \left( \frac{\sqrt{2}}{2}, \frac{\sqrt{2}}{2}, 0 \right); \left( -\frac{\sqrt{2}}{2}, \frac{\sqrt{2}}{2}, 0 \right)$$

Due to the large number of datasets necessary to generate the diffusion tensor, DTI experiments are often implemented using a fast-imaging method such as the echo-planar imaging (EPI) acquisition method (Turner *et al.*, 1990).

### 3.3.2. Metrics of Diffusion Isotropy

From DTI data, it is possible to extract information regarding the tissue microstructure on a voxel-by-voxel basis. Quantifiable DTI information should be independent of the orientation of the reference frame of the sample under study, that is, an invariant quantity. One invariant index of isotropic diffusion is the mean diffusivity, which characterizes the overall mean-squared displacement of molecules and overall presence of impediments to diffusion. The mean diffusivity is invariant to the coordinate system used to measure  $\mathbf{D}$  and, thus, is not affected by the orientation of the sample relative to the reference frame of the NMR system. Mean diffusivity,  $\langle D \rangle$ , is calculated from the trace of the diffusion tensor,  $\text{Tr}(\mathbf{D})$ , and is given by:

$$\langle D \rangle = \text{Tr}(\mathbf{D})/3 = (D_{xx} + D_{yy} + D_{zz})/3 \quad (2.14)$$

### 3.3.3. Metrics of Diffusion Anisotropy

Interest in extracting information regarding the degree of diffusion anisotropy from the diffusion tensor has led to derivation of numerous scalar quantities that describe the variation of molecular displacements throughout a sample of interest (Basser *et al.*, 1996). As with the mean diffusivity parameter, it is necessary that the diffusion anisotropy parameter be an invariant parameter to provide an objective measure of the intrinsic structure within the sample. Lacking an invariant measure, the anisotropy parameter would vary depending on the frame of reference of the NMR system gradient coils relative to the frame of reference of the

sample. The fractional anisotropy (FA) index is a commonly used invariant DTI parameter that provides objective intravoxel structural information. The FA represents the magnitude of the anisotropic component of  $\mathbf{D}$  as a percentage of the magnitude of the total diffusion tensor. Calculation of FA is facilitated through diagonalization of the diffusion tensor, which yields eigenvalues ( $\lambda_1, \lambda_2, \lambda_3$ ) and eigenvectors that define the predominant direction of diffusion. The FA parameter is then calculated from the eigenvalues and mean diffusivity on a voxel-by-voxel basis as given by:

$$FA = \sqrt{\frac{3}{2}} \frac{\sqrt{(\lambda_1 - \langle D \rangle)^2 + (\lambda_2 - \langle D \rangle)^2 + (\lambda_3 - \langle D \rangle)^2}}{\sqrt{\lambda_1^2 + \lambda_2^2 + \lambda_3^2}}. \quad (2.15)$$

FA is a dimensionless quantity that yields values between 0 (representing perfectly isotropic diffusion) and 1 (representing perfectly anisotropic diffusion).

# Chapter 3

## Tendon Composition and Characterization by NMR

---

Composition of Tendon  
Hierarchical Organization of Collagen  
Tendon Ultrastructure  
Tendon Mechanical Properties

Previous NMR Investigations of Tendon  
Spectroscopic Water Diffusion  
Characterization  
Spectroscopic Water Diffusion  
Characterization

This chapter provides an introduction to the structural composition of tendons and serves as background for the NMR experiments on tendons that are the topic of subsequent chapters in this dissertation. In addition, a review of previous NMR experiments with tendon is provided. Tendons are connective tissues that behave like cables to connect and transmit force between muscle and bone. In general, textbook discussions of tendon often note the interrelation between structure and function in tendon. That is, their composition of primarily parallel-fibered collagen is structured such that they are extraordinarily strong in resisting tensile load, a property that reflects the intent of their mechanical function: to enable animation of the skeleton.

## 1. Tendon Composition

### 1.1. Hierarchical Organization of Collagen

The tendon microstructure consists of sparsely distributed fibroblast cells and an extracellular matrix composed of fibrillar structures embedded in a ground substance (Frank *et al*, 1990). Comprising up to 85% of the tendon dry weight, type I collagen is the primary fibrillar component of the extracellular matrix with elastin (a scarce secondary fibrillar component) and proteoglycans (the primary component of the ground substance) each contributing less than 5% of the tendon dry weight (Martin *et al.*, 1998). The fibrillar structures of the extracellular matrix are highly ordered, hierarchical arrangements with collagen molecule building blocks. The diagram of Fig. 3.1 depicts the hierarchical organization of collagen that spans from the molecular tropocollagen chains to the macroscopic tendon fascicles. The type I collagen molecule consists of three chains of amino acids wound helically about one another (Viidik, 1990). Collagen molecules

aggregate to form microfibrils that in turn group to form fibrils. Collagen fibrils are packed into fibers that assemble into primary and secondary bundles or fascicles, which ultimately form the tendon itself. As the collagen structures pack together to form the successive structure in the hierarchy, they form primarily parallel to one another along what becomes the long axis of the gross tendon. Jozsa *et al.* (1991) have shown that in addition to those that form longitudinally with the long axis of the tendon, some fibrils ‘criss-cross’ with one another to form spiral-shaped fibrils while others are oriented horizontally and transversely to the primary tendon axis. The ratio of longitudinal to non-longitudinal fibril orientation ranges from 10:1 to 26:1 (Jozsa *et al.*, 1991). At the fiber level of the hierarchy, a planar waviness is observed in the relaxed specimen; a feature often referred to as fiber crimping (Kastelic *et al.*, 1978).

## 1.2. Tendon Ultrastructure

Delineating the various hierarchical levels of the tendon is a complex network of membranes. A common terminology has not been adopted in naming the layers within this hierarchy; therefore we will follow that of Jozsa and Kannus (1997) where the word ‘endotenon’ refers to the collagenous structures that work to bind the tendon fibers and fascicles together. Surrounding the entire tendon are two layers of connective tissue: paratenon, the outermost layer; and epitenon, the innermost layer (Jozsa *et al.*, 1997). As shown by Jozsa *et al.* (1991), the geometry of the collagen fiber epitenon network is best described as ‘criss-crossed’ with longitudinal, oblique and transversal fibers, it is much more heterogeneous than the primarily parallel fibers of the tendon core. Occasionally



epitenon fibers fuse with superficial tendon fibers to provide a union between the surrounding membrane and the core of the tendon. The outer paratenon layer is a loose network of connective tissue with synovial cells, collagen and elastin fibrils lining its inner surface (Jozsa *et al.*, 1991).

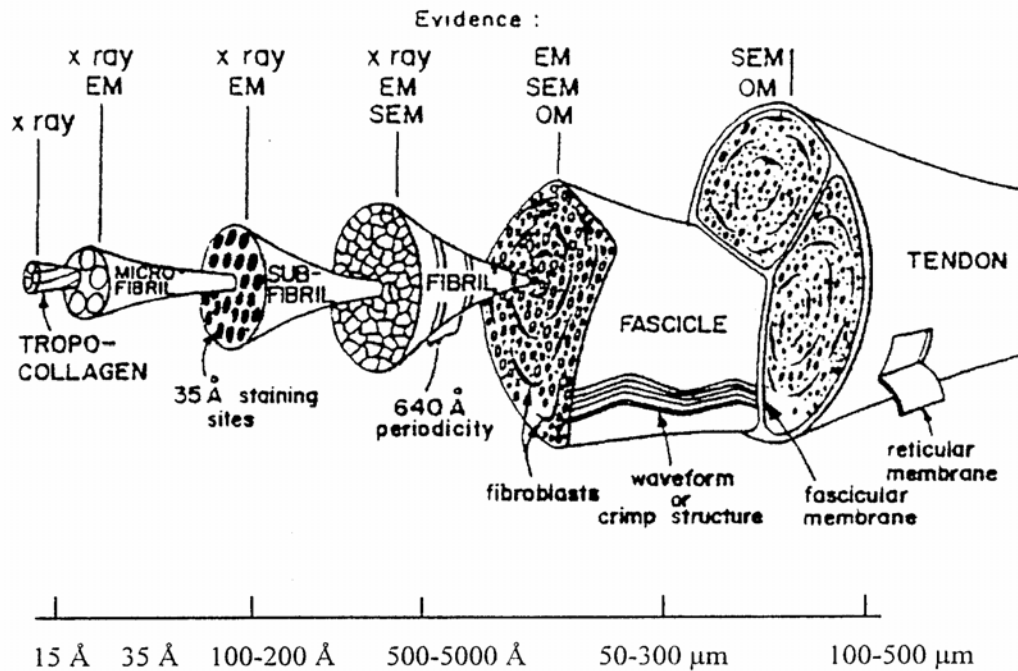


Figure 3.1 – Overview of the organizational structure of tendon. Spanning from the molecular tropocollagen to the macroscopic sub-tendon fascicles, the composition of the collagen substructure in tendon follows a hierarchical arrangement. [Figure from Kastelic J *et al.*, *Conn. Tis. Res.* 6:11-23 (1978).]

### 1.3. Tendon Mechanical Properties

Soft connective tissues such as tendon are, in general, viscoelastic materials (Martin, 1998), which implies that stress in the tissue at a fixed strain rate is time-dependent. The general stress-strain curve of tendon is characterized by three regions: a nonlinear toe region, a linear region, and a nonlinear failure region. The mechanical response of the toe region is believed to reflect the

gradual uncrimping of collagen fibers, while in the linear region, all the collagen fibers are in a state of tension as they are straightened and stretched. The final nonlinear region is the plastic deformation region resulting from yield and failure of the collagen fibers. The mechanical loads applied to the tendon samples in the experiments that follow in subsequent chapters of this dissertation are within the range of physiological loading and fall within the linear region of the stress-strain curve.

## 2. Previous NMR Investigations of Tendon

### 2.1. Spectroscopic Relaxation Time Characterization

A number of *in vivo*  $^1\text{H}$ -NMR studies have spectroscopically characterized  $T_1$  and  $T_2$  relaxation times of tendon (Peto *et al.*, 1990a; Henkelman *et al.*, 1994). Each of these works has demonstrated four distinct components of the transverse relaxation time, attributable to different proton populations in the tendon microstructure. Peto *et al.* (1990a) proposed that the four proton populations represented by these components were (in order of shortest to longest  $T_2$  value): macromolecular  $^1\text{H}$  (protons of the tropocollagen polypeptide chains); tightly bound interstitial water  $^1\text{H}$  (water molecules located within the triple-helix interstices and fixed by two hydrogen bonds); weakly bound tropocollagen hydration water  $^1\text{H}$  (weakly bound to macromolecules and much more mobile than interstitial water); free water  $^1\text{H}$  of the amorphous ground substance.

In addition, it is known that the  $T_2$  of tissues with ordered parallel molecular arrangements, as is the case with the hierarchical structure of collagen fibers in tendon, has an orientational dependence with respect to the  $B_0$  field (Berendsen,

1962; Fullerton *et al.*, 1985; Peto *et al.*, 1990b; Henkelman *et al.*, 1994; Haken *et al.*, 2000). This  $T_2$  anisotropy is due to variation in the susceptibility gradients that arise across the sample when placed in different orientations with respect to the static field (Fullerton *et al.*, 1988). A slight orientational dependence has also been exhibited for  $T_1$  relaxation (Fullerton *et al.*, 1985; Peto *et al.*, 1990b; Henkelman *et al.*, 1994), but not to the same degree as the  $T_2$  anisotropy.

## 2.2. Spectroscopic Water Diffusion Characterization

Tendon tissue has also been the subject of a number of studies investigating the ADC of water through NMR spectroscopy. Henkelman *et al.* (1994) investigated diffusion anisotropy in bovine tendon and found relatively large diffusion coefficients ( $\sim 1.4 \times 10^{-5} \text{ cm}^2/\text{sec}$ ) in directions parallel and perpendicular to the long axis of the tendon. In contrast, Han *et al.* (2000) have shown strong diffusion anisotropy between the parallel and perpendicular directions, which seems more consistent with the known structural anisotropy of tendon. The discrepancy between these two studies is probably due to the different experimental conditions used in each. In the work by Henkelman *et al.*, the tendon sample, not the gradient direction, was rotated to measure the water diffusion in perpendicular directions. As we have previously discussed, the  $T_2$  relaxation time in tendon is strongly dependent on sample orientation relative to the static magnetic field. Therefore, diffusion measurements made by varying the sample orientation would result in different populations of spins contributing to the measurement due to  $T_2$  relaxation effects. The experiments by Han *et al.* (2000) were conducted with the tendon long axis parallel to the  $B_0$  field and the

direction of the applied diffusion gradient was changed to assess diffusion anisotropy; therefore, different diffusion directions did not impose varying magnetic susceptibility gradients to the measurement.

Another aspect of the work by Han *et al.* (2000) was to study the effect of tensile loading on the spectroscopic measures of the water ADC. Application of a tensile load resulted in an ADC increase over that of the unloaded case for directions parallel and perpendicular to the tendon long axis. However, the diffusion anisotropy ratio fell from an unloaded value of 2.3 to 1.8 ( $t_{\text{dif}} = 8.5$  msec) upon loading. This finding was interpreted by hypothesizing that tensile loading causes extrusion of water from tendon. The extruded water accumulates along the outside boundary of the tendon, creating a bulk phase that is relatively free of barriers to diffusion. An increase in the spectroscopic ADC is observed because the NMR signal is averaged over the entire tendon structure, including the bulk water phase. This work also characterized the diffusion-time ( $t_{\text{dif}}$ ) dependent ADC response to each tensile load condition and diffusion direction. It was revealed that the resulting  $\text{ADC}(t_{\text{dif}})$  curves followed a similar behavior irrespective of load condition or direction of the ADC measurement. ADC decreased with increasing  $t_{\text{dif}}$  at the initial time points, as is characteristic of restricted diffusion systems (Helmer *et al.*, 1995), however, at longer  $t_{\text{dif}}$  points, the behavior of the curves was ambiguous. For some cases, it appeared that the water ADC remained constant at long  $t_{\text{dif}}$  while in others the ADC actually

appeared to increase. These results suggested that additional studies were needed to better characterize the diffusion-time dependence of the water ADC in tendon.

# Chapter 4

## Characterization of the Spectroscopic Water ADC( $t_{dif}$ ) in Rabbit Achilles Tendon

---

Introduction

Methodology

Experimental Set-up

NMR Experimental Parameters

Results

Discussion

Conclusion

Acknowledgments

---

This chapter summarizes a series of spectroscopic NMR experiments that were performed to investigate the diffusion-time dependence of the apparent diffusion coefficient of water in rabbit Achilles tendon. The characterization was made with tendons subjected to two states of tensile load to investigate the sensitivity of the water diffusion measurement to structural changes that may occur in the tendon under differing tensile load conditions.

#### 1. Introduction

In a previous report (Han *et al.*, 2000), we presented evidence of anisotropy in the apparent diffusion coefficient (ADC) of water in rabbit Achilles tendon. In that study, spectroscopic NMR measurements of water ADC were found to be greater in the direction parallel to the long axis of the tendon in comparison to the perpendicular direction. Since tendons are anisotropic materials (i.e. they are comprised of collagen fibrils that generally run parallel to the long axis of the tendon), this finding agreed with our hypothesis that the ADC of tendon water would also be anisotropic. That is, it was expected that water molecules diffusing in the direction parallel to the long axis of the tendon would encounter fewer restricting barriers than those diffusing in the perpendicular direction.

A goal of our initial study was to determine whether applying tensile loads to the tendon altered the ADC of water. It was shown in both the presence and absence of an applied tensile load that diffusion anisotropy in tendon is maintained. We also characterized the diffusion-time ( $t_{\text{dif}}$ ) dependent ADC response to each tensile load condition and diffusion direction. It was revealed that the resulting ADC( $t_{\text{dif}}$ ) curves

followed a similar behavior irrespective of load condition or direction of the ADC measurement. ADC decreased with increasing  $t_{\text{dif}}$  at the initial time points, as is characteristic of restricted diffusion systems (Helmer *et al.*, 1995), however, at longer  $t_{\text{dif}}$  points, the behavior of the curves was ambiguous. For some cases, it appeared that the water ADC remained constant at long  $t_{\text{dif}}$  while in others the ADC actually appeared to increase. These results suggested that additional studies were needed to better characterize the long  $t_{\text{dif}}$  behavior of the water ADC in tendon. Furthermore, we wanted to better characterize the short  $t_{\text{dif}}$  behavior of the tendon water ADC with the goal of ascertaining the effect of tensile loading on the surface-to-volume ratio (S/V).

In this study, the diffusion-time dependence of the ADC of endogenous water in rabbit Achilles tendon was characterized using spectroscopic measurements out to a  $t_{\text{dif}}$  of 400 msec. Also, the number of measurements at short  $t_{\text{dif}}$  values (i.e. where  $t_{\text{dif}} < 50$  msec) was increased relative to that used in the previous study in order to improve estimates of S/V. Diffusion sensitization was applied parallel ( $\text{ADC}_{\parallel}$ ) and perpendicular ( $\text{ADC}_{\perp}$ ) to the longitudinal axis of the tendon. The diffusion-time-dependent ADC curves were characterized with samples subject to two tensile load conditions: an initial case where the sample was maintained taut with a nominal 40 g mass; and a second case where a 500 g mass was applied to the sample. Preliminary results of this work have been previously reported (Wellen *et al.*, 2002).



## 2. Methodology

### 2.1. Experimental Set-up

The preparation of and method for applying tensile load to tendons are described in detail in Han *et al.* (2000). Briefly, Achilles tendons from young (~3 kg) New Zealand white rabbits of either sex were harvested from each hind-leg while held in a glove-box chamber maintained at a humidity level not less than 90%; tendons harvested from animals of this size were 2.0 – 2.5 cm in length. After harvesting, samples were maintained over the course of the experiment in a bath of perfluoroalkylether, Krytox<sup>®</sup> grade GPL-102 (DuPont, Deepwater, NJ) lubricant oil, in an effort to maintain the tendon samples near *in situ* hydration levels. The use of Krytox<sup>®</sup> also insured that there was no proton signal from the bathing solution contributing to the tendon water ADC measurements.

Tendons were mounted in an apparatus (Fig. 4.1) that orients the samples in the magnet bore such that their long axis is parallel to the static  $B_0$  field. The apparatus consists of a platform that rests in the bore of a gradient insert and an extension piece (not shown in Fig. 4.1) that reaches outside the magnet bore to support the mass used to load the sample. The platform contains a well that accommodates the RF coil and tendon and is filled with Krytox<sup>®</sup>. Lengths of size #1 braided-silk suture, tied to each end of the tendon, were used to secure the sample in the well and to apply the tensile load to the sample. The suture lines run through slots located at each end of the well. These slots were packed with Krytox<sup>®</sup> grade 240-AC grease to prevent leakage from the bathing well over the course of the experiments. An RF coil was fabricated from copper sheeting and formed into an oblong-shaped, single-turn solenoid with a cutout at each end to

allow it to be overlaid on the tendon sample in the well. A chip capacitor was soldered in the gap between the two ends of the RF coil (not shown in Fig. 4.1) to tune it to the appropriate resonance frequency. This coil was inductively coupled to a second coil placed on the underside of the well (not shown in Fig. 4.1) that connects directly to the transmitter and receiver electronics of the NMR system.

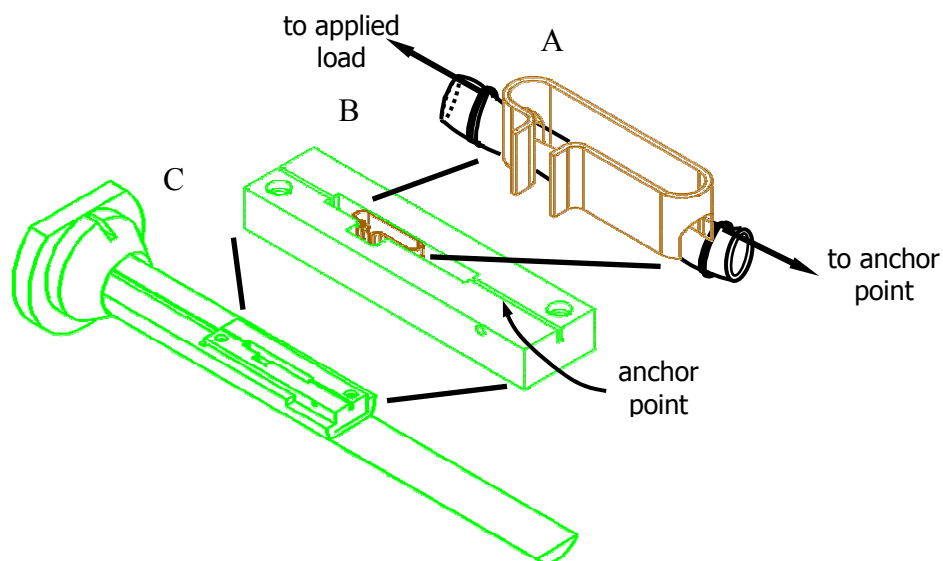


Figure 4.1 – Hierarchy of tendon-holding apparatus. The tendon rests in the trough of the Krytox<sup>®</sup> oil-filled well (B) with the suture material tied about each end. The suture material passes through slots at each end of the well, which were packed with a Krytox<sup>®</sup> grease to prevent leakage of the bathing oil. The RF coil (with a cutout at each end) fits over the tendon sample (A) and is inductively coupled to a pick-up coil place on the underside of the well (not shown in diagram). The well is secured on a slide (C) that rests in the bore of a  $\pm 280$  G/cm gradient insert.

## 2.2. NMR Experimental Parameters

NMR experiments were performed with a GE CSI-II 2.0T/45 cm imaging spectrometer (GE NMR Instruments, Fremont, CA) operating at 85.56 MHz for <sup>1</sup>H and equipped with a  $\pm 280$  G/cm gradient insert. Spectroscopic measurements

of tissue water ADC were made at 12 diffusion times (over the range of 5.5 – 400 msec) to characterize the ADC as a function of  $t_{\text{dif}}$ . At each  $t_{\text{dif}}$  point, data were acquired with diffusion sensitization parallel and perpendicular to the long axis of the tendon. A combination of diffusion-weighted spin echo (SE) and stimulated echo (STE) pulse sequences were used in the experiment with common parameters of: TR/TE = 1500.0/25.0 msec, SW =  $\pm 2000$  Hz, 1024 complex digitization points, NEX = 2 (for DW-SE) or 8 (for DW-STE),  $\delta = 6.0$  msec, and seven diffusion-gradient strengths ranging from 2 to 14 G/cm in 2 G/cm increments. Datasets were transferred to an off-line workstation for processing using routines written with IDL<sup>®</sup> (Research Systems, Boulder, CO).

### 3. Results

The calculated ADCs from the spectroscopic diffusion experiments ( $N = 8$ ) are given as a function of the square root of diffusion-time in the plots of Fig. 4.2. The data points represent average ADC values ( $\pm$  S.E.M.) calculated from all tendon samples. Each plot follows a similar  $t_{\text{dif}}^{1/2}$  dependence: an initial ADC decrease before a minimum value is reached, after which the ADC begins to rise and subsequently level off to a constant value at long diffusion times. For ADC measurements in both diffusion directions, the effect of an applied tensile load to the tendons is an increase in the water ADC at each diffusion-time.

### 4. Discussion

The data in Fig. 4.2 clearly corroborate the results from our previous study which demonstrated three characteristics of rabbit Achilles tendon: (1) the ADC is

anisotropic; (2) the ADC is diffusion-time dependent; and (3) tensile loading results in an ADC increase in both diffusion directions (for further discussion of these points, refer to (Han *et al.*, 2000)).

We previously interpreted the tensile-load-induced ADC increase as an extrusion of water from tendon (Han *et al.*, 2000). The presence of a bulk water phase increases the mean ADC of the entire tendon resulting in a constant offset of the ADC curves from their unloaded baseline condition. Structural information can be extracted from the curves of Fig. 4.2 by considering the ADC behavior at short diffusion times. In biological systems, where the motion of some fraction of water molecules is always restricted, the  $ADC(t_{dif})$  will be reduced from the bulk unrestricted self-diffusion coefficient,  $D_0$ . Mitra *et al.* (1992; 1993) have shown that in the short  $t_{dif}$  regime,  $ADC(t_{dif})$ , normalized by  $D_0$ , is given by the following equation:

$$\frac{ADC(t_{dif})}{D_0} = 1 - \frac{4}{9\sqrt{\pi}} \frac{S}{V} \sqrt{D_0 t_{dif}} \quad (4.1)$$

where  $(S/V)$  is the average surface-area to volume ratio of the space available for diffusion. The general form of Eq. (4.1) is a linear equation with intercept =  $D_0$  and slope  $\propto (S/V)$ ; therefore, the initial slope of the  $ADC(t_{dif})$  vs.  $t_{dif}^{1/2}$  plots in Fig. 4.2 reflects  $(S/V)$  of the system. Calculation of  $(S/V)$  with this equation, however, requires that  $D_0$  be known. Experimental determination of  $D_0$  is difficult in biological systems in general and is confounded even further in this circumstance by the constant offset effect of the bulk water on the loaded tendon  $ADC(t_{dif})$  curves. Normally,  $D_0$  could be estimated by noting that the limit of  $ADC(t_{dif}) \rightarrow D_0$  as  $t_{dif} \rightarrow$

0. Consequently, extrapolation of the linear fit of the initial time points of  $ADC(t_{dif})$  vs.  $t_{dif}^{1/2}$  back to the zero-time intercept would yield  $D_0$ . However, due to the ADC-offset effect from the bulk water component, this procedure results in erroneous  $D_0$  values. Instead, we used the slope from the linear fit of the three initial time points to bypass the bulk water  $D_0$  influence and directly infer the (S/V) ratio for each curve. The slopes that result from this procedure are reported for each experimental condition in Table 4.1.

Table 4.1 – Initial slopes from the short  $t_{dif}$  regime  $ADC(t_{dif})$  vs.  $t_{dif}^{1/2}$  plots (Fig. 4.2) for each experimental condition. Slopes were obtained from the linear fit of the first three time points to bypass the  $D_0$  influence that results from tendon loading, thereby directly inferring the (S/V) ratio for each curve.

	initial slope [ $\times 10^{-5} \text{ cm}^2/\text{sec}^{3/2}$ ]
$ADC_{\perp}$	
unloaded	-2.7
loaded	-4.0
$ADC_{\parallel}$	
unloaded	-2.2
loaded	-2.1

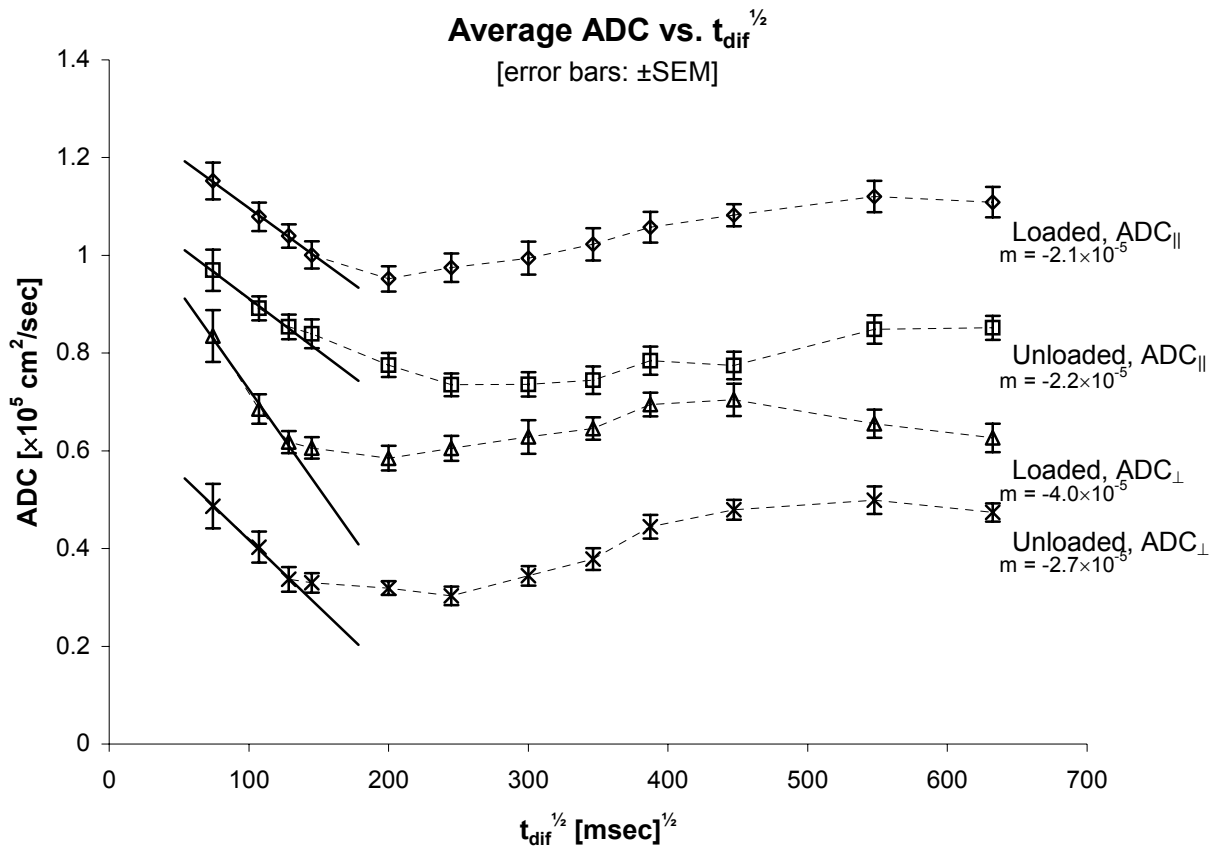


Figure 4.2 – Spectroscopically-acquired diffusion-time dependent plots of ADC ( $N = 8$ , mean  $\pm$  SEM) with diffusion sensitization parallel and perpendicular to the tendon long axis for each of the two tensile load conditions: unloaded refers to the case where a nominal 40 g mass was applied; loaded refers to the case where a 500 g mass was applied (--- lines connecting the data points are not fits to the data, rather an aid to guide the eye). A linear fit of the three initial time points of each curve (— lines) yields slopes,  $m$ , that are reflective of the  $(S/V)$  ratio for each curve. The ADC increase observed at the long  $t_{dif}$  points is interpreted as a  $T_1$  spin-editing effect from the use of the STE pulse sequence. This occurs because increasing the diffusion-time results in elimination of the population of water molecules with relatively short  $T_1$  values due to a concomitant increase in the TM period (during which  $T_1$  relaxation occurs) in the STE pulse sequence.

From the slope data in Table 4.1, we note a dramatic increase in the steepness of the slope of  $ADC_{\perp}$  between the unloaded and loaded conditions while  $ADC_{\parallel}$  experienced virtually no change in slope between load conditions. The slope  $\propto (S/V)$  relationship

implies that an increase in slope corresponds with a decrease in the local space available for molecular diffusion. The finding of an increased slope in the  $ADC_{\perp}$  direction with tensile loading is consistent with a structural model of tendon whereby loading increases the collagen fibril packing density. Measurement of rabbit Achilles tendon collagen fibril diameters from electron microscopy images were previously shown to have an average value on the order of  $\sim 0.15 \mu\text{m}$  (Han *et al.*, 2000). The 1-D mean molecular displacement for a given  $t_{\text{dif}}$  can be calculated from the ADC values in the plots of Fig. 4.2. For example, consider ADC values at the third  $t_{\text{dif}}$  point (i.e.,  $t_{\text{dif}} = 16.5 \text{ msec}$ ). The Einstein relation predicts a 1-D mean displacement of  $(2t_{\text{dif}}ADC)^{1/2}$ , which for the loaded  $ADC_{\parallel}$  case is  $5.9 \mu\text{m}$  and for the unloaded  $ADC_{\perp}$  case is  $3.3 \mu\text{m}$ . These displacement values are an order of magnitude larger than the mean collagen fibril diameter, which means that diffusing spins have traversed distances far greater than the fibril diameter and the ADC measurement averages over these structures. In spite of this, the difference in slope noted for the  $ADC_{\perp}$  direction suggests that the slope calculation is sensitive to structural changes occurring with tensile loading. This finding is interesting as it may provide evidence of the mechanism responsible for the displacement and subsequent accumulation of water molecules in a bulk phase upon tensile loading. In the direction parallel to the tendon long axis, collagen fibrils are largely oriented parallel to one another and offer fewer barriers to diffusion than in the perpendicular direction (this is evident from the diffusion anisotropy shown in Fig. 4.2). The lack of slope change in the parallel diffusion direction indicates either that no structural changes occur to the fibrils along the parallel direction or that the diffusion measurement was not sensitive to the

structural changes that do occur (i.e., tensile loading may straighten the crimped collagen fibrils that exist in tendon under rest (Kastelic *et al.*, 1978), but the length scale of the crimp is much larger than that of the RMS displacement of the diffusing water molecules).

The data in Fig. 4.2 also clarifies the previous ambiguity regarding the long  $t_{\text{dif}}$  water ADC behavior of tendon. For each experimental condition, the ADC increases after  $t_{\text{dif}} \sim 50$  msec. The ADC increase observed after  $t_{\text{dif}} \sim 50$  msec is most likely due to the elimination of one population of water molecules with relatively short  $T_1$  values. This  $T_1$  spin-editing effect is peculiar to the DW-STE pulse sequence where the diffusion-time increase is achieved through a concomitant increase in the TM period between the second and third  $90^\circ$  pulses. Since the z-magnetization is inverted during the TM period it will experience  $T_1$  decay. Consequently, the observed signal will be weighted to the distribution of water molecules having the longest  $T_1$  values and correspondingly fewer restrictions to diffusion. The effect of this situation would be an apparent increase in the water ADC at longer diffusion times.

## 5. Conclusions

The results of this study are consistent with our previous work which showed that the water  $\text{ADC}(t_{\text{dif}})$  behavior of rabbit Achilles tendon changed under differing states of tensile load. In this study, we have better characterized the water ADC at long  $t_{\text{dif}}$  points and hypothesized that the apparent increase in water ADC is due to  $T_1$  editing, which removes spins with short  $T_1$  from contributing to the long  $t_{\text{dif}}$  ADC values. Secondly, change in the inferred (S/V) ratio of  $\text{ADC}_\perp$  suggests that tensile loading



increases the collagen fibril packing density – a finding that should prove important in elucidating the mechanism of load-induced tendon water extrusion.

6. Acknowledgments

Discussions with Prof. Michael B. Smith regarding construction of the RF coil assembly are gratefully acknowledged.

Supported in part by NIH grant NS-10783.

# Chapter 5

## Spatial Characterization of Tendon by NMR

---

Introduction	Quantitative Analysis of Parameter Maps
Methodology	Diffusion-Time Dependent ADC Imaging
Sample Preparation	Discussion
Experimental Set-up	Spin Populations Observed in Imaging
NMR Experimental Parameters	Experiments
Data-Processing	Localized Relaxation & ADC Parameter Values
Results	Data Interpretation With Respect to Tendon
Tendon Imaging in Cross-Section	Ultrastructure
Qualitative Analysis of Parameter Maps	Acknowledgements

---

This chapter is a compilation of the series of NMR imaging experiments performed to spatially characterize the relaxation and water apparent diffusion coefficient parameters in rabbit Achilles tendons. As with the experiments of the preceding chapter, these experiments were conducted with tendon subject to differing states of tensile load to determine how the effects of tensile loading are manifested in the different parameters.

#### 1. Introduction

Water plays an important role in the response of biological soft tissue to mechanical perturbations (Viidik, 1990). In cartilage, for example, compressive-load testing has demonstrated the influence of hydration on the tissue's static material properties (Mow *et al.*, 1984). It has been shown that compressive loading causes water movement through the solid extracellular matrix of the tissue, adding a viscous component to the load response (Mow *et al.*, 1984; Elden, 1964). Similar behavior has been reported in mechanical testing of ligament. Chimich *et al.* (1992) varied the water content of ligaments through osmotic means prior to mechanical cycling tests and found that water content affects the viscoelastic response of the tissue. Time-dependent viscoelastic behaviors have also been noted in various soft tissues, reflecting interactions between the collagen structure, ground substance and extracellular water of the tissue (Woo *et al.*, 1981). Tensile loading of tendon has been found to cause a reduction in tissue water content (Hannafin *et al.*, 1994). A redistribution of the collagen fiber-packing array was the proposed mechanism of this water displacement. However, the exact mechanism of this tensile-load-derived displacement of water from tendon tissue remains uncertain. Gaining further

understanding of the role that water plays in soft tissue mechanics may enable further development of micromechanical models of soft-tissue behavior (Silver, 1987).

Previous *in vivo* measurements of water diffusion have been motivated by an interest in characterizing tissue properties such as structure, permeability or anisotropy. In a previous study from this laboratory (Han *et al.*, 2000), the apparent diffusion coefficient (ADC) of water was used to explore changes associated with tensile loading of tendons. ADC was measured spectroscopically in Achilles tendons during application of a tensile load. It was found that the tensile load caused an increase in the water ADC over that of the unloaded case. This finding was interpreted by hypothesizing that tensile loading causes extrusion of water from tendon. The extruded water accumulates along the outside boundary of the tendon, creating a bulk phase that is relatively free of barriers to diffusion. An increase in the spectroscopically-measured water ADC is observed because the NMR signal is averaged over the entire tendon structure, including the bulk water phase.

In order to test this model, the spatial variation of the tendon response to tensile loading was investigated. Since tendons are not homogeneous structures (Jozsa *et al.*, 1997), we hypothesized that diffusion measurements would be non-uniform in tendons. If the model is correct, tensile loading of tendon should cause the ADC to drop in the central core region and rise in the peripheral rim region. To this end, we have devised a method for segmenting transverse images of tendons into two regions: a core and a rim. We then studied whether loading caused the water ADC to rise in the rim and drop in the core – as would be expected if water were extruded. We also

investigated  $T_1$  and  $T_2$  relaxation parameters in the two regions with and without load. Similar to the expected changes in water ADC, extrusion of water from the core to the rim region upon tensile loading would increase the  $T_1$  and  $T_2$  relaxation times of the rim and decrease their values in core. Preliminary results of this work have been previously reported (Wellen *et al.*, 2001; 2002).

## 2. Methodology

### 2.1. Sample Preparation

Studies were conducted using Achilles tendons from young (~3 kg) New Zealand white rabbits of either sex. Rabbits were euthanized with an overdose of Nembutal<sup>®</sup> (Abbot Labs, Chicago, IL). Achilles tendon samples were harvested from each hind-leg. In an effort to minimize tendon dehydration, dissection of was performed in a glove-box chamber maintained at a minimum humidity level of 90%. After harvesting, samples were maintained over the course of the experiment in a bath of Krytox<sup>®</sup> oil (DuPont, Deepwater, NJ). This is a perfluoroalkylether that contains no hydrogen and thus is not visible in the  $^1\text{H}$  MRI of the tendon.

### 2.2. Experimental Set-up

Harvested tendon samples were 2.0 - 2.5 cm in length. Lengths of braided-silk suture (#1 braided) were tied to each end of the tendon. The tendon was mounted in a Krytox<sup>®</sup>-filled well on a Lucite<sup>®</sup> platform (refer to Fig. 4.1 in Chapter 4). The platform was placed in a gradient insert and held in the magnet bore such that the long axis of the tendon was parallel to  $B_0$  (Fig. 5.2). One piece of suture anchored the specimen to the platform; the other piece was used to

apply tensile loads to the sample. The suture lines ran through slots located at each end of the well. These slots were packed with Krytox<sup>®</sup> grade 240-AC grease to prevent oil leakage from the bathing well. An RF coil was fabricated from copper sheeting and formed into an oblong-shaped, 14 mm × 3 mm single-turn solenoid with a notch cut in each end. The notches allowed the coil to be overlaid on the tendon when it was mounted in the well. The geometry of the coil was designed so as to optimize the filling factor in an effort to maximize SNR. The resonant coil was inductively coupled to a coil placed on the underside of the well (not shown in Fig. 4.1). The suture used for applying loads was run along a beam that extended outside the magnet that had a pulley at its end (Fig. 5.2). Masses were hung from the suture to load the tendon under two states of tension: a baseline condition with a nominal (40 g) mass applied to maintain tautness in the sample (referred to as the ‘unloaded’ condition) and a test condition with a 500 g mass applied (referred to as the ‘loaded’ condition).

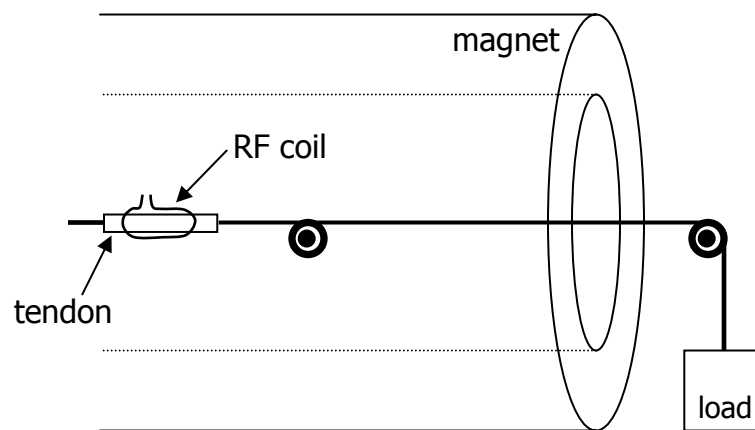


Figure 5.2 – Assembled experimental set-up with holding apparatus positioned in the magnet bore supporting the mass used to apply the tensile load to the tendon sample.

### 2.3. NMR Experimental Parameters

NMR experiments were performed with a GE CSI-II 2.0T/45 cm imaging spectrometer (GE NMR Instruments, Fremont, CA) operating at 85.56 MHz for  $^1\text{H}$  and equipped with a  $\pm 280$  G/cm gradient insert. Due to the duration of the experiments, not all datasets were acquired from each tendon sample. A summary of the experiments performed along with the number of samples used and, in the case of 3-D data acquisitions, number of slices included in the analysis of each is given in Table 5.1.

The primary imaging experiments involved acquisition of 3-D image datasets [ $128 \times 128 \times 8$ , FOV = 5 mm  $\times$  5 mm  $\times$  20 mm]. The 8-step phase-encoding direction was along the longitudinal axis of the tendon with a 20 mm FOV.

From the datasets, 2-D maps of  $T_1$ ,  $T_2$ ,  $M_0$  and ADC parallel and perpendicular to the long axis of the tendon ( $\text{ADC}_{\parallel}$  and  $\text{ADC}_{\perp}$ ) were calculated.  $T_1$  parameter maps were generated from image datasets acquired with a spin-echo progressive saturation (SE-PS) method [NEX = 2, TE = 5.0 msec, TR intervals = 100.0, 300.0, 500.0, 1000.0 and 2500.0 msec].  $T_2$  parameter maps (and the associated  $M_0$  maps) were generated from image datasets acquired with a spin-echo ( $T_2$ -SE) sequence [NEX = 8 or 16, TE intervals = 5.0, 15.0, 45.0 and 55.0 msec]. ADC maps with  $t_{\text{dif}}$  of 5.8 msec were generated from image datasets acquired using a diffusion-weighted, pulsed-field gradient spin-echo (PFG-SE) sequence [NEX = 8, TE = 12.1 msec, diffusion gradient duration  $\delta$  = 2.0 msec and spacing  $\Delta$  = 6.3 msec and diffusion-gradient amplitudes of 30, 45, 75, 125 and 175 G/cm].

In effort to maximize the efficiency of the lengthy 3-D imaging experiments, partial-flip-angle imaging was implemented in the T<sub>2</sub>-SE and PFG-SE sequences to reduce total acquisition time. The flip angle ( $\theta$ ) that yields the optimal signal-to-noise ratio for a given repetition time and sample T<sub>1</sub> (the Ernst angle) is given by:  $\theta = \cos^{-1}[\exp(-TR/T_1)]$  (Ernst *et al.*, 1966). Spectroscopic measurements of T<sub>1</sub> from our tendon samples were ~550 msec; therefore, with a 300 msec TR the optimal flip angle is 54°. In a spin-echo implementation, the initial excitation pulse angle is (180° -  $\theta$ ) rather than  $\theta$ , corresponding to 126° in our experiments (Winkler *et al.*, 1988).

In a separate set of diffusion-weighted imaging experiments, a single-slice stimulated-echo (DW-STE) sequence was used to generate ADC maps at diffusion-times longer than those used in the 3-D PFG-SE experiments ( $t_{\text{dif}} = 50.0, 125.0$  and  $250.0$  msec). Different diffusion-gradient strengths were used with each  $t_{\text{dif}}$  value to generate the corresponding ADC map. The values were calculated to yield four b-values that covered the same range as those used in the 3-D imaging experiments where  $t_{\text{dif}} = 5.8$  msec. Other parameters common to each acquisition in this set of experiments were: TR/TE = 1200.0/12.1 msec,  $\delta = 2.0$  msec, slice thickness = 4.0 mm and NEX = 16.

In the PFG-SE and DW-STE datasets, the readout compensation and phase-encode gradients were placed after the diffusion-sensitization period immediately before the signal readout period as discussed in (Conturo *et al.*, 1995) to alleviate cross-term effects.



Table 5.1 – Summary of the pulse sequence parameters used to acquire image datasets with the number of tendon samples and total number of slices analyzed in each dataset under each load condition.

Experiment	Acquisition Sequence	Incremented Parameter Values	# samples (# slices)	
			Unloaded	Loaded
3-D Parameter Mapping				
$T_1$	SE-PS (TE=5 ms)	TR=100, 300, 500, 1000, 2500 ms	4 (14)	5 (15)
$T_2$	SE (TR/ $\theta$ =300 ms/126°)	TE=5, 15, 45, 55 ms	10 (35)	11 (38)
$ADC_{  ,\perp}$	PFG-SE (TR/ $\theta$ =300 ms/126°, TE=12.1 ms, $\Delta$ =6.3 ms, $\delta$ =2.0 ms)	G=30, 45, 75, 125, 175 G/cm	10 (35)	10 (31)
ADC( $t_{dif}$ ) Imaging	DW-STE (TR/TE=1200/12.1 ms, $\delta$ =2.0 ms)	$t_{dif}$ = 50, 125, 250 ms	3	3

## 2.4. Data-Processing

Datasets were transferred to an off-line workstation for processing. Routines written with the IDL<sup>®</sup> software package (Research Systems, Boulder, CO) were used for image reconstruction, parameter-map generation, image segmentation and statistical calculations.

### 2.4.1. Image Reconstruction

During the 3-D dataset image reconstruction, a Hanning-window filter was applied over the in-plane slice data and across slices prior to Fourier transformation to reduce aliasing and interslice bleed. After reconstruction, the central 3 or 4 slices of a dataset were selected for inclusion in the remainder of the image analysis. Maps of relaxation parameters and diffusion coefficients were calculated from the reconstructed datasets on a pixel-by-pixel basis.

#### 2.4.2. Parameter Map Generation

A number of inclusion criteria were required in order for the fitted pixel value to be considered a valid contributor to a particular parameter map. First, voxels were required to meet a minimum signal-to-noise ratio of two. A criterion unique to ADC map generation was implemented due to the environment in which water protons reside in the tendon. In the log domain, pixel signal intensity values begin to decay in a non-linear fashion with increasing b-value due to structures within the tissue that provide restriction to diffusion. Only those b-values considered to fall within the linear portion of the decay curve were included in the linear fit in effort to obtain an accurate ADC value from the slope of the fitted line. To determine which b-values were in the linear portion of the decay curve, a comparison of the chi-squared difference between the fitted line and the points included in the fit for the case of 5 b-values, 4 b-values and 3 b-values was made. The percent change in the chi-squared value between fits of decreasing number of b-values was inspected and a percent change less than 5% was chosen to indicate a good linear fit using the higher number of b-values. Finally, fixed thresholds were applied to each of the parameter maps whereby pixels falling outside of the threshold range were discarded from the map. The upper level thresholds were chosen for each parameter based on expected values from bulk water protons: [0, 2000 msec], [0, 200 msec] and [0,  $2 \times 10^{-5}$  cm<sup>2</sup>/sec] for T<sub>1</sub>, T<sub>2</sub> and ADC, respectively.

#### 2.4.3. Image Segmentation

We wanted to make comparisons between measurements made in the rim versus the core region of the tendon. In order to discriminate between these two areas, we segmented the image into two compartments. A gradient-operator-based edge detection algorithm (Russ, 1995) using a  $3 \times 3$  kernel was applied to the proton-density ( $M_0$ ) maps to create two segmentation masks of each slice: one mask of the tendon central core region and one mask of the surrounding peripheral rim of the tendon. These masks were then used to segment the corresponding parameter maps from which average values of  $T_1$ ,  $T_2$ ,  $M_0$ ,  $ADC_{\parallel}$  and  $ADC_{\perp}$  were calculated for each region.

#### 2.4.4. Change in $M_0$ Ratio Calculation

The effect of tensile loading on the distribution of proton-density across the tendon was assessed through the  $M_0$  parameter maps. To allow comparison of the unitless  $M_0$  parameter between load conditions, a normalization process was employed. Each usable slice from a sample's  $T_2$  dataset was included to create an  $M_0$  ratio value for each load condition. The ratio was calculated from the average value of pixels contributing to the tendon central core or peripheral rim region. The average regional  $M_0$  values from each slice of a sample's dataset were then averaged to determine the representative  $M_{0\text{ RIM}}$  and  $M_{0\text{ CORE}}$  values of the sample. A ratio of  $M_{0\text{ RIM}} : M_{0\text{ CORE}}$  was then calculated for each load state of the sample:

$$M_0^{\text{RATIO}} = \left( \frac{\sum_1^m M_0^{\text{RIM}}}{\sum_1^n M_0^{\text{CORE}}} \right) \quad (5.1)$$

With the unloaded and loaded  $M_0$  ratios, the percent change between load conditions was determined:

$$\% \text{ change in } M_0 = \frac{M_{0, \text{Loaded}}^{\text{RATIO}} - M_{0, \text{Unloaded}}^{\text{RATIO}}}{M_{0, \text{Unloaded}}^{\text{RATIO}}} \quad (5.2)$$

With the 2-D ADC( $t_{\text{dif}}$ ) image datasets, maps of ADC were calculated for each  $t_{\text{dif}}$  point in the same manner as the 3-D ADC datasets. Average tendon core and peripheral rim region values of  $\text{ADC}_{\parallel}$  and  $\text{ADC}_{\perp}$  were calculated from the masked parameter maps for each load condition.

#### 2.4.5. Statistical Analysis

Average parameter values reported in Table 5.2 are shown plus or minus the associated standard error of the mean (S.E.M.). Statistically significant differences in the mean parameter value between tendon regions or tensile load conditions were determined based on Student's t-test analysis with a significance level of  $\alpha = 0.05$ . For those parameters found to have statistically significant differences, p-values are indicated.

### 3. Results

#### 3.1. Tendon Imaging in Cross-Section

From the proton-density weighted images, it was observed that in cross-section, the tendon samples were composed of two regions with distinct differences in

signal intensity [Fig. 5.3(A)]. At the periphery of the tendon, a thin region of high signal intensity encircles a region of low signal intensity in the central core. Adjacent to the image in Fig. 5.3 are the corresponding binary masks of the rim (B) and core (C) regions for the given slice generated from the segmentation routine.

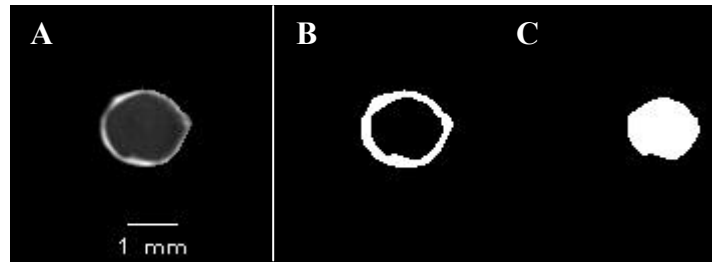


Figure 5.3 – Example proton density weighted image of tendon cross-section (A) with the corresponding binary masks of the rim (B) and core (C) regions for the given slice generated from the gradient-operator-based segmentation routine.

### 3.2. Qualitative Analysis of 3-D Parameter Maps

Representative parameter maps generated from the 3-D datasets ( $T_1$ ,  $T_2$ ,  $ADC_{\parallel}$  and  $ADC_{\perp}$ ) are provided in Fig. 5.4 with the rim region segmented from the core region for illustrative purpose. The range of values for each parameter is provided in the colorbar legend. The top row of maps and their associated histograms represent unloaded tendon data while the bottom row represents data from the corresponding slice in the loaded condition. Direct, semi-quantitative comparisons can be made between unloaded and loaded parameter map segments to assess the effect of tensile loading on the spatial distribution of values within the two tendon regions. The histogram plots associated with each segmented map provide the parameter values for both tendon regions (--- rim region, —

core region), showing in a more quantitative manner their distribution within a given region.

For the unloaded  $T_1$  data in Fig. 5.4, there is a dramatic difference in  $T_1$  values between the tendon rim and core regions: the rim region has a larger average value and wider distribution ( $\sim 0.6$  sec mean, 0.06 – 1.4 sec range) than that of the core region ( $\sim 0.5$  sec mean, 0.3 – 0.8 sec range). By contrast, the average values and distributions of  $T_2$ ,  $ADC_{\parallel}$  and  $ADC_{\perp}$  are relatively similar for the two regions in the unloaded state. With tensile loading, Fig. 5.4 demonstrates that a regional distinction of ADC values in both diffusion directions develops with the rim region moving toward a higher mean ADC while the core region remains unchanged from the unloaded condition. For  $ADC_{\perp}$ , the rim region average increases to  $\sim 0.6 \times 10^5$  cm<sup>2</sup>/sec (compared to  $\sim 0.4 \times 10^5$  cm<sup>2</sup>/sec in the unloaded case); within the  $ADC_{\parallel}$  maps, the rim region average increases to  $\sim 1.0 \times 10^5$  cm<sup>2</sup>/sec (compared to  $\sim 0.8 \times 10^5$  cm<sup>2</sup>/sec in the unloaded case). In both cases, the core region ADC maps do not differ from the unloaded case. For the  $T_1$  parameter, the number of loaded rim region pixels at the high end of the  $T_1$  range increases over that of the unloaded state, increasing the average  $T_1$  to  $\sim 0.8$  sec while the core region does not change from the unloaded case. The  $T_2$  parameter maps do not experience any load-induced change in either tendon region.

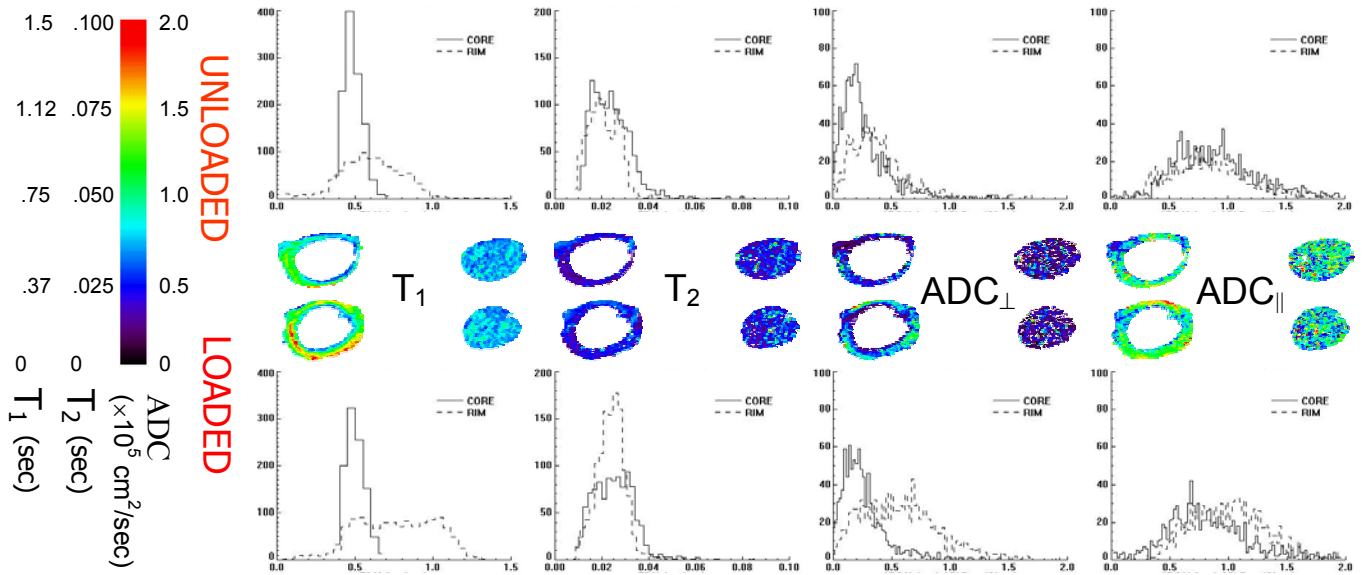


Figure 5.4 – Composite figure providing example output of  $T_1$ ,  $T_2$ ,  $ADC_{\parallel}$  and  $ADC_{\perp}$  segmented parameter maps with their respective histograms for each load condition.

### 3.3. Quantitative Analysis of 3-D Parameter Maps

A summary of the average calculated parameter values ( $\pm$  S.E.M.) from all tendon samples is reported by load condition and tendon region in Table 5.2. As with the parameter maps of Fig. 5.4, comparison of the overall average values in Table 5.2 between regions within a load condition demonstrates the heterogeneity that exists across the tendon. For the unloaded condition, statistically significant differences between the rim and core regions exist for  $T_1$ ,  $T_2$  and  $ADC_{\perp}$  ( $P < .05$ ). For the loaded condition, statistically significant differences between the rim and core regions exist for  $T_1$ ,  $T_2$ ,  $ADC_{\parallel}$  and  $ADC_{\perp}$  ( $P < .05$ ). Between-load-condition comparisons indicate a statistically significant increase in the rim-region  $ADC_{\parallel}$  and  $ADC_{\perp}$  ( $P < .005$ ) values. No

loaded core region parameter was found to have a statistically significant change from the unloaded case.

Loading was also found to affect the  $M_{0\text{ RIM}} : M_{0\text{ CORE}}$  ratio calculated from the  $T_2$  datasets. The ratio increased by 15% between the unloaded and the loaded conditions. This result is consistent with the hypothesis that loading causes a transfer of water molecules from the tendon core to the tendon rim.

Table 5.2 – Mean  $\pm$  S.E.M. values for  $T_1$ ,  $T_2$ ,  $ADC_{\parallel}$  and  $ADC_{\perp}$  calculated from average pixel values of RIM and CORE regions' respective parameter maps. \* – indicates a statistically significant difference for the parameter between tendon regions,  $P < .05$ . \*\* – indicates a statistically significant difference for the parameter within the tendon region between load conditions,  $P < .005$ . ( $N$ 's contributing to each of the parameter conditions indicated in Table 5.1.)

	Unloaded	
	rim	core
$T_1$ [msec]	$670 \pm 20$	$530 \pm 10^*$
$T_2$ [msec]	$22.0 \pm 0.5$	$28 \pm 1^*$
$ADC_{\perp}$ [ $\times 10^5$ cm <sup>2</sup> /sec]	$0.40 \pm 0.03$	$0.25 \pm 0.01^*$
$ADC_{\parallel}$ [ $\times 10^5$ cm <sup>2</sup> /sec]	$0.78 \pm 0.03$	$0.79 \pm 0.03$

	Loading effect on	
	rim	core
$T_1$ [msec]	$\downarrow 4.5\%$	$\downarrow 15.1\%$
$T_2$ [msec]	$\uparrow 4.1\%$	$\downarrow 10.0\%$
$ADC_{\perp}$ [ $\times 10^5$ cm <sup>2</sup> /sec]	$\uparrow 57.5\%^{**}$	$\uparrow 8.0\%$
$ADC_{\parallel}$ [ $\times 10^5$ cm <sup>2</sup> /sec]	$\uparrow 20.5\%^{**}$	$\downarrow 6.3\%$

Differences in diffusion anisotropy were found across tendon regions. In the tendon core region, the unloaded average  $ADC_{\parallel} : ADC_{\perp}$  anisotropy ratio from Table 5.2 is 3.2; in the tendon rim region, the average is 1.9. When loaded, the core-region average anisotropy ratio decreases to 2.7 and the rim-region average



anisotropy ratio declines to 1.5. What initially appears to be a noteworthy change in the core region is, upon closer inspection, a response to statistically insignificant changes in the average directional ADC values. The core-region data in Table 5.2 indicates the  $ADC_{\parallel}$  decreases while the  $ADC_{\perp}$  increases with tensile loading, but neither of these changes were found to be statistically significant. This situation exemplifies the care required when interpreting changes in the anisotropy ratio. The tensile-load-induced changes in water ADCs of the rim region, however, are statistically significant and result in an anisotropy-ratio decrease.

### 3.4. Diffusion-Time Dependent ADC Imaging

The water ADC diffusion-time dependence for the segmented tendon regions under each load condition is shown for  $ADC_{\parallel}$  and  $ADC_{\perp}$  in Fig. 5.5(A) and (B), respectively. Included for completeness in these plots are average ADC values obtained at  $t_{\text{dif}}=5.8$  msec from the 3-D datasets. The average ADC values plotted in these figures are the average of the  $M_0$ -weighted ADCs from each tendon region for the given experimental condition. That is, each point in the plots represents:

$$M_0\text{-weighted average ADC} = \frac{\sum_{i=0}^n M_{0i} ADC_i}{\sum_{i=0}^n M_{0i}} \quad (5.3)$$

where  $n$  is the total number of pixels in a given tendon region. All conditions in the  $ADC_{\parallel}$  case follow the trend of a decrease from the  $t_{\text{dif}}=5.8$  msec point followed by a rise after a minimum is reached at the 50 msec diffusion-time. In

the  $ADC_{\perp}$  case, the loaded condition follows this trend while the unloaded condition does not indicate a decrease from the  $t_{dif}=5.8$  msec point before rising with increasing diffusion time.

Figure 5.6 provides cumulative histograms of ADC values from the segmented ADC maps of the three tendon samples used in this experiment. The figure is separated into histogram triads that show the diffusion-time dependence of the water ADC within each tendon region as a function of diffusion sensitization direction and load condition. Axial scaling is identical on each of the histograms to allow direct comparison of the number of fitted pixels and the ADC distributions between tendon regions and between experimental conditions.

From this figure, the effect of increasing the period allowed for  $T_1$  relaxation (i.e. increasing  $t_{dif}$ ) on the ADC maps is the same for each experimental condition: the percent decrease in the number of core-region pixel contributions is larger relative to the decrease in the rim region. In general, the characteristics of the ADC distributions at successive diffusion-times within a given triad are comparable except for the loaded rim region triads. The general appearance of each histogram in a triad is Poisson-like with the peak of the distribution decreasing with increasing  $t_{dif}$ . The exception is the loaded-rim region where the triads in both diffusion directions show the bulk of the pixel values shifting to higher ADCs with increasing diffusion time.

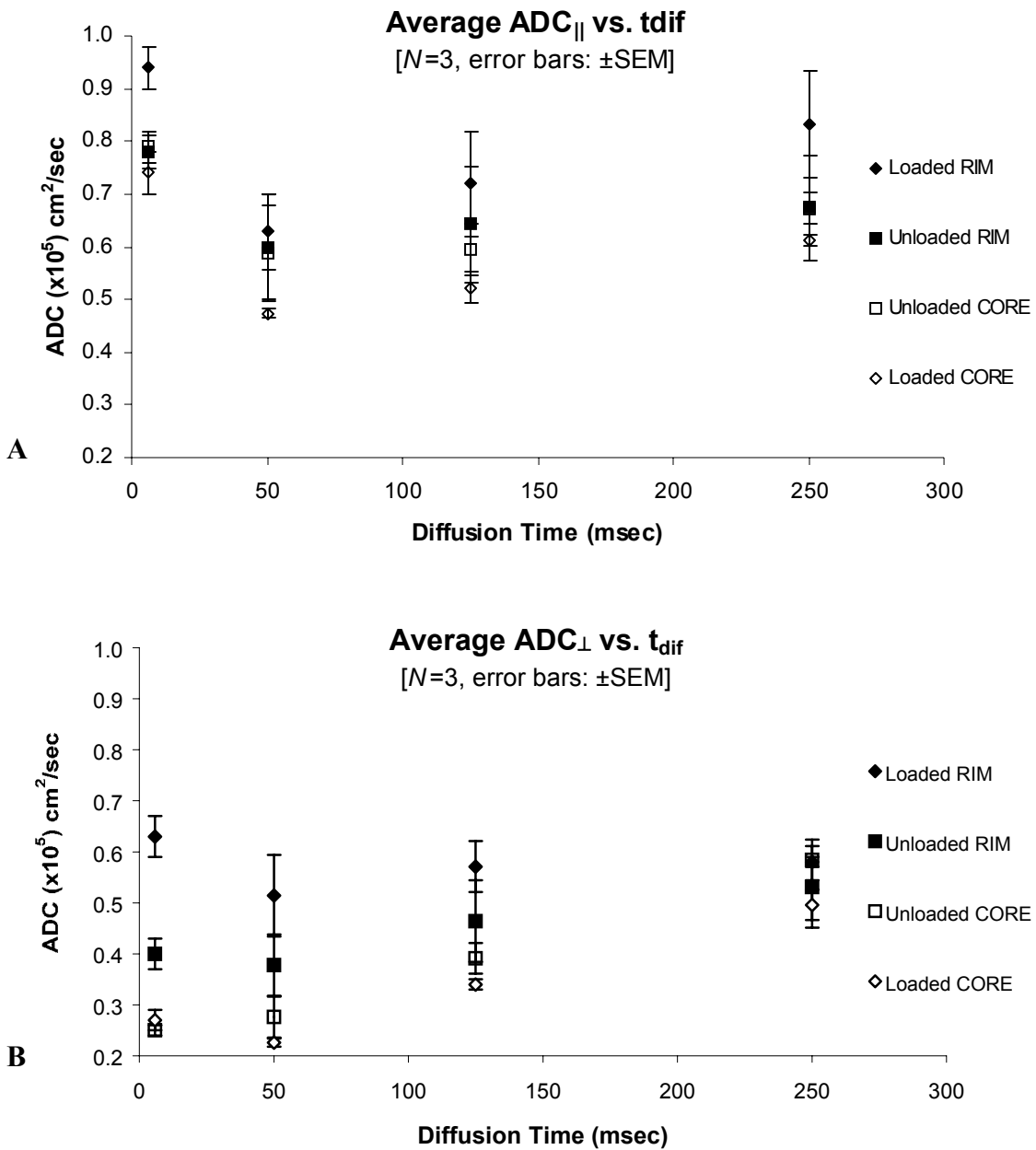


Figure 5.5 – Mean values of (A)  $ADC_{\parallel}$  and (B)  $ADC_{\perp}$  ( $\times 10^{-6}$   $cm^2/sec$ ) calculated from average pixel values in rim and core regions and plotted as a function of diffusion time for each load condition [points at  $t_{dif}=5.8$  msec included for reference] ( $N=3$ ).

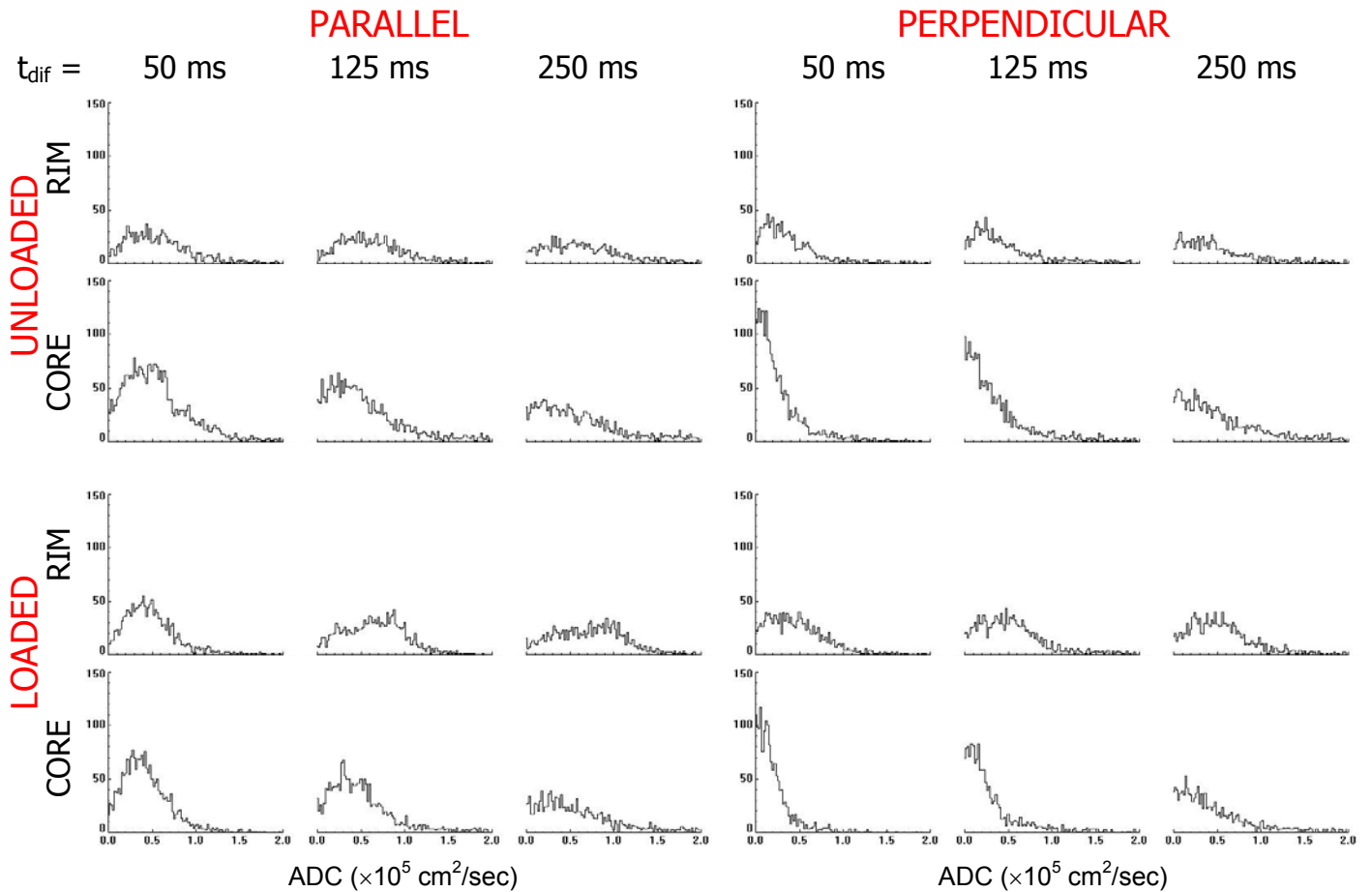


Figure 5.6 – Histograms of the cumulative number of fitted pixels from the segmented ADC maps of all tendon samples ( $N=3$ ) with respect to diffusion time point and experimental condition: diffusion sensitization parallel (left) and perpendicular (right) to the tendon long axis and subject to tensile load of: nominal 40g mass (unloaded) and 500g mass (loaded).

#### 4. Discussion

##### 4.1. Spin Populations Observed in Imaging Experiments

Several research groups have employed various fitting algorithms [e.g.

nonnegative least squares (Whittall *et al.*, 1989)] to spectroscopic NMR data

from tendon to demonstrate the heterogeneity of transverse relaxation times that

arise due to variations in the tendon microstructure (Fullerton *et al.*, 1985; Peto *et*

*al.*, 1990a; 1990b; Henkelman *et al.*, 1994). In the work by Peto *et al.* (1990a) and Henkelman *et al.* (1994), four distinct  $T_2$  components attributable to different proton populations were observed. Peto *et al.* proposed that the four proton populations represented by these components were (in order of shortest to longest  $T_2$  value): macromolecular  $^1\text{H}$  (protons of the tropocollagen polypeptide chains); tightly bound interstitial water  $^1\text{H}$  (water molecules located within the triple-helix interstices and fixed by two hydrogen bonds); weakly bound tropocollagen hydration water  $^1\text{H}$  (weakly bound to macromolecules and much more mobile than interstitial water); free water  $^1\text{H}$  of the amorphous ground substance.

The observed transverse relaxation values are dependent upon the tendon sample orientation in relation to the static magnetic field direction (Berendsen, 1962; Fullerton *et al.*, 1985; Peto *et al.*, 1990b; Henkelman *et al.*, 1994; Haken *et al.*, 2000). This behavior is due to variation in the susceptibility gradients that arise across the sample depending on its orientation with respect to the static field. All of our experiments were performed with samples aligned with their long axis parallel to the static field. According to Peto *et al.* (1990a), of the four  $T_2$  components they observed in this orientation, the two shortest are reported to have  $T_2$ 's  $< 5$  msec. All of our experiments use TE values greater than 5 msec; therefore, we do not expect any significant contributions from the tightly bound interstitial water or macromolecular protons (the two components with  $T_2 < 5$  msec) and attribute signal in our experiments to weakly bound and free water molecules. With regard to the  $T_2$  mapping, total-experiment-time limitations

only permitted acquisition of a limited number of TE values (four). Therefore, during the map generation routine, only single exponential fitting of the data was performed resulting in  $T_2$  maps that represent a weighted average of the two water  $^1\text{H}$  populations.

## 4.2. Localized Relaxation and ADC Parameter Values

### 4.2.1. Localized ADC Anisotropy Ratios

Our interpretation of the water ADC anisotropy ratios derived from the image datasets reveals two attributes of diffusion measurements in tendon subject to tensile load. First, the anisotropy ratio of the rim region follows very closely to the short  $t_{\text{dif}}$  spectroscopic anisotropy demonstrated in the plots of Fig. 4.2 from the previous chapter. The spectroscopically-derived anisotropy ratios from those experiments are  $\sim 2.0$  for the unloaded case and  $\sim 1.5$  for the loaded case. These values correspond with the rim region values obtained from Table 5.2 (1.9 and 1.5, for each of the respective load conditions) and suggest the tendon periphery plays a dominant role in water ADC measurements. The finding that the ADC anisotropy ratio of the rim region is less than that of the core region is consistent with the more densely packed fibrillar collagen structures of the tendon core. The second attribute addresses the significance of a larger percent increase in rim-region  $\text{ADC}_{\perp}$  relative to the  $\text{ADC}_{\parallel}$  increase with tensile loading. In support of our hypothesis that tensile loading induces extrusion of water to the tendon periphery, a large  $\text{ADC}_{\perp}$  increase is expected to accompany accumulation of bulk water at the tendon periphery. Due to fewer

restrictions parallel to the tendon long axis,  $ADC_{\parallel}$  is already high; therefore it follows that additional bulk water at the tendon periphery would yield a greater percent increase in  $ADC_{\perp}$  under tensile loading.

#### 4.2.2. Diffusion-Time Dependence of ADC

In the diffusion-weighted STE imaging sequence used to map the diffusion-time dependence of the ADC within tendon,  $T_1$  relaxation occurring during TM serves to effectively eliminate signal contributions from spins with short  $T_1$  at longer  $t_{dif}$  values. From the  $T_1$  parameter mapping data summarized in Table 5.2, we note a statistically significant difference between the average  $T_1$  of rim and core regions irrespective of load condition. Due to the shorter average  $T_1$  of the core relative to the rim, it is expected that a greater proportion of core-region spins will be eliminated at longer  $t_{dif}$ s. The experimental output of Fig. 5.6 supports this hypothesis.

Comparison of the rim- and core-region histogram triads in Fig. 5.6 reveals a larger percent decrease in the number of core-region pixel contributions relative to the rim region with increasing  $t_{dif}$  for each of the experimental conditions. In general, core-region pixels have a lower initial  $M_0$  and more restrictions to diffusion relative to those in the rim region. Therefore, the increase in  $t_{dif}$  will have a more profound effect in the core region than in the rim region. The effect of noise in the fitting routine is apparent in the core region's  $t_{dif} = 250$  msec histograms where

the frequency of high ADC voxels increases from the  $t_{\text{dif}} = 50$  msec points. From this, it was inferred that the core region is more susceptible to poor ADC fitting because of low SNR due to the low initial  $M_0$  in this tendon region.

Also note from Fig. 5.6 that not all low ADC voxels are eliminated from the  $t_{\text{dif}} = 250$  msec histograms, regardless of tendon region. This implies that those voxels with a low water ADC are associated with a distribution of  $T_1$  values and the distribution contains values sufficiently long enough such that they do not completely decay away during the longest diffusion time. In general, fewer low-ADC pixels are contributing to the histograms at the 125 and 250 msec  $t_{\text{dif}}$  points relative to the 50 msec  $t_{\text{dif}}$  point and therefore the relative weighting of high ADC values increases as  $t_{\text{dif}}$  increases. This effect is noted in the  $\text{ADC}(t_{\text{dif}})$  plots of Fig. 5.5, where the  $M_0$ -weighted average ADC values increase with increasing diffusion time. These findings provide further support for the hypothesis that the water ADC increase following the initial decline through the short  $t_{\text{dif}}$  points may be explained in terms of  $T_1$  spin-editing.

#### 4.2.3. Effects of Tensile Loading

The primary finding from the loaded-imaging experiments is a statistically significant increase in both  $\text{ADC}_{\parallel}$  and  $\text{ADC}_{\perp}$  of the rim region over the unloaded case (Table 5.2). An observation of note is that the average loaded  $T_2$  value decreased in the core region and increased in the rim



region. Though neither change was found to be statistically significant, the average  $T_2$  values of the rim and core did move in directions that would be consistent with the hypothesis of water transport from tendon core to rim. As suggested by Peto *et al.* (1990b), the greater the mobility of the water proton in the tendon microstructure, the longer its  $T_2$ . A  $T_2$  decrease in the tendon core would therefore indicate a smaller mobile water proton fraction contributing to the average regional value; similarly, a  $T_2$  increase in the tendon rim would indicate a larger mobile water proton fraction contributing to the average regional value.

The within-slice  $M_{0\text{RIM}}:M_{0\text{CORE}}$  ratio calculation yields representative  $M_0$  values that are normalized to permit an  $M_0$  comparison between load states. The observed increase in the  $M_0$  ratio between the load conditions implies an increase in the density of rim water protons relative to the core upon loading. Although we are unable to attribute this change in  $M_0$  to a specific tendon region (i.e., due to an isolated change in  $M_{0\text{RIM}}$  or  $M_{0\text{CORE}}$ ), the increase in the ratio between the load conditions is in itself of interest. Whether an increase in  $M_{0\text{RIM}}$  or a decrease in  $M_{0\text{CORE}}$ , the finding of an increased  $M_0$  ratio upon loading is consistent with the idea of water transport from the tendon core to its peripheral rim.

Another aspect of interest regarding the tensile-load-induced transport of water to the tendon periphery lies in the histogram triads of Fig. 5.6.

Within the loaded-rim-region  $ADC_{\parallel}$  triad, an increase in the number of mid-range ADC pixels occurs that is not observed in the unloaded case. One interpretation of this bulk shift of ADC values during the loaded experiment is the slow accumulation of water at the tendon periphery over the period of time required to acquire the datasets (approximately  $2\frac{1}{2}$  hours for each  $t_{dif}$  point). However, interpretation of this observation is slightly ambiguous due to the possibility of tendon translation and creep with tensile loading that may result in slightly different slice geometry in the images at each  $t_{dif}$  point.

The scatter plots of Fig. 5.7 were generated to investigate the effect of tensile loading on the relationship between  $ADC_{\parallel}$  and  $T_1$  from a tendon sample in which both datasets were acquired. Corresponding  $ADC_{\parallel}$  and  $T_1$  parameter map pixel values from a representative slice are plotted in Fig. 5.7 with colored data points that reflect their region of origin in the tendon. Marginal distributions of the corresponding regional parameter are provided by the dashes along the respective axis, yielding ‘dash-dot’ style plots as discussed in Tufte (1983). The distributions of  $ADC_{\parallel}$  and  $T_1$  in this figure follow a similar pattern to those provided in Fig. 5.4. The loaded dash-dot plot shows a change in ‘slope’ of the rim region pixels’  $ADC_{\parallel}:T_1$  relationship whereby those associated with a high ADC shift to a longer  $T_1$  relative to the unloaded case. In terms of our tensile-load-induced water extrusion model, we interpret the change of slope in the

rim-region  $ADC_{\parallel}:T_1$  relationship as a reflection of the non-uniform redistribution of bulk water to the rim region upon loading. This is in contrast to a shift of the entire population to longer  $T_1$ s that would accompany a uniform distribution of water at the tendon periphery – a situation that may develop over time.

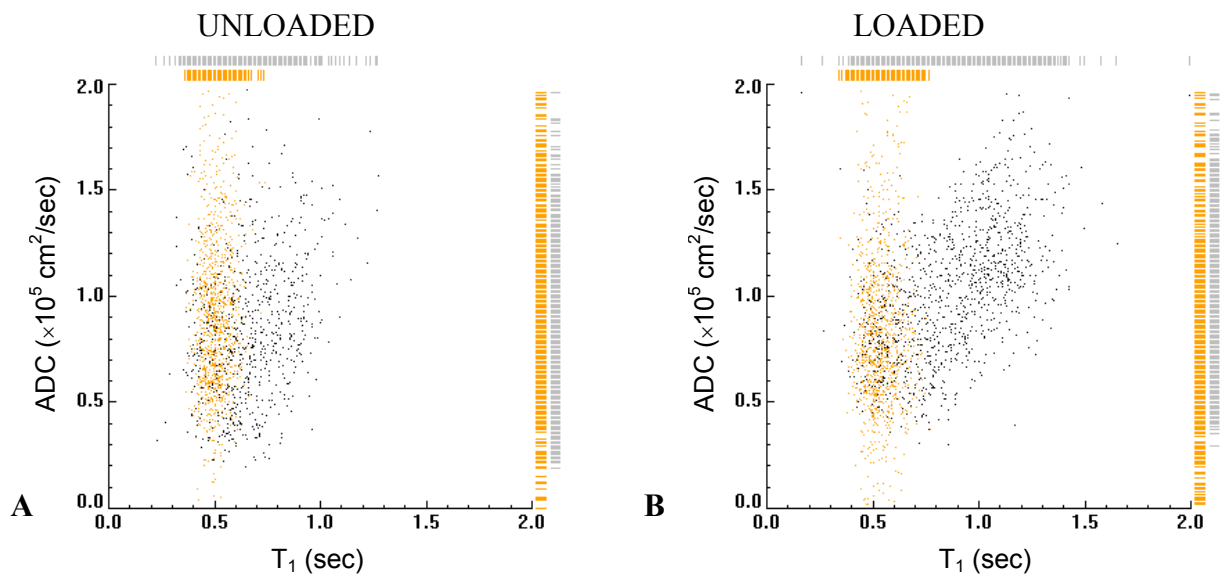


Figure 5.7 – Dash-dot style plots of the relationship between  $ADC_{\parallel}$  and  $T_1$  from a representative sample in the unloaded (**A**) and loaded (**B**) condition. Colored data points reflect their region of origin in the tendon (gray: rim, orange: core). Dashes along the axes allow comparison of the corresponding parameter’s marginal distribution between tendon regions.

#### 4.3. Data Interpretation With Respect to Tendon Ultrastructure

Differences exist between the structural characteristics of the central and peripheral regions of human tendon (Jozsa *et al.*, 1991). The different structural environments experienced by diffusing water protons are the most likely source of the regional differences in NMR parameters noted in this work. The regional differences in diffusion anisotropy, for example, are consistent with the regional differences in

tendon ultrastructure. Additionally, one of the primary effects of tensile loading on tendon is a statistically significant increase of the average water ADC in the rim region; a result that suggests tensile-load-induced structural changes occur in the tendon periphery. As noted in Jozsa *et al.* (1997), the collagen fibers of the epitenon are at an  $\sim 60^\circ$  angle with the fibers of the tendon core region while at rest. This angle decreases to  $\sim 30^\circ$  when stretched. Straightening of the epitenon fiber angularity may account for the increased  $ADC_{\parallel}$  upon tensile loading. In the perpendicular direction, an influx of water in the space between the epitenon and paratenon layers of the outer tendon sheath could account for the increase in  $ADC_{\perp}$  upon tensile loading. If this were the case, this finding would lend additional evidence to the argument for the extrusion of water to the tendon periphery upon tensile loading which may aid the development of micromechanical models of soft tissue behavior subject to mechanical perturbation.

#### 5. Acknowledgements

Discussions with Prof. Michael B. Smith regarding construction of the RF coil assembly are gratefully acknowledged.

Supported in part by NIH grant NS-10783.

# Chapter 6

## Functional Brain Imaging

---

Physiological Origins of BOLD Contrast  
Hemodynamic Response to Neuronal  
Activation  
Magnetic Properties of Blood  
Magnetic Susceptibility Induced  
Signal Change  
Characteristics of the BOLD Signal

Detection of Neuronal Activation  
Block Design Experiment  
fMRI Data Analysis  
Statistical Inference

---

This chapter is intended to provide an introduction to the principles behind functional brain imaging with MRI. The development of and applications for functional magnetic resonance imaging (fMRI) have grown to make fMRI one of the most widely used methods for investigating human brain function and continues to hold promising potential to provide insight into how the brain works, in both normal and diseased states. The foundations of this multi-disciplinary field of research are discussed in this chapter with emphasis placed on the use of blood-oxygenation-level-dependent (BOLD) contrast in functional neuroimaging. This method is based on MR signal changes due to hemodynamic and metabolic responses at the sites of neuronal activation induced by external and internal stimuli to the brain. The basic experimental approach used to exploit this difference in signal is to acquire imaging data during a *control* state and then during an *active* state. Neuroanatomical locations with non-zero differences in image signal intensity between the two states implies neuronal involvement during the active state. Application of this functional imaging technique has allowed researchers to construct high-spatial-resolution, whole-brain activation maps of sensory and cognitive function.

1. Physiological Origins of the BOLD Contrast Mechanism

A fundamental feature of neuronal activation that underlies a number of functional neuroimaging methods is that blood flow and energy metabolism are rather tightly linked to neuronal activity. Positron emission tomography (PET) has been used to demonstrate increased blood flow in focal cortical regions related to task activation, where the percent-blood-flow increase exceeded the percent increase in oxygen consumption (Fox *et al.*, 1986). This mismatch between blood flow and oxygen consumption is exploited in BOLD contrast fMRI, causing blood to act as an endogenous MRI contrast agent (Ogawa

*et al.*, 1990). It is these physiologic responses that enable BOLD-contrast fMRI to infer information about the underlying neuronal activity. In the following sections, these concepts are discussed further.

### 1.1. Hemodynamic Response to Neuronal Activation

A number of physiologic response mechanisms interact to regulate cerebral blood flow (CBF) as the local metabolic demand of activated neurons increases (Guyton *et al.*, 1996). Concomitant with a local increase in CBF are increases in cerebral blood volume (CBV) and the metabolic rate of oxygen consumption (CMRO<sub>2</sub>), however, no significant change in tissue oxygen extraction. These hemodynamic changes result in a decrease of the oxygen extraction fraction (OEF – a measure of the arterio-venous difference in hemoglobin oxygen saturation) that results from an increase in venous blood oxygenation. Consequently, it is the increase in venous blood volume and venous blood oxygenation that affects the signal intensity of the MR image during neuronal activation. The next issue to be discussed is the nature of this oxygenation-dependent variation in signal intensity.

### 1.2. Magnetic Properties of Blood

The magnetic properties of blood vary with oxygen content (Pauling *et al.*, 1936). The reason for this variation is related to the magnetic properties of the hemoglobin molecule. Since oxygen is not very soluble in blood, it is transported through the vasculature bound to hemoglobin of red blood cells. At the core of hemoglobin is a heme-iron complex that imparts its magnetic properties to the hemoglobin molecule. Due to the location of the oxygen binding sites on hemoglobin, the magnetic

susceptibility of the molecule will change as a function of its oxygenation status. Magnetic susceptibility ( $\chi$ ) is an index of the extent to which an applied magnetic field is distorted as it interacts with a material. Those materials that add a local contribution to the applied magnetic field (i.e., increased magnetic flux) are said to be paramagnetic, whereas materials that have a negligible local effect on the applied magnetic field are referred to as diamagnetic. Deoxygenated hemoglobin (deoxyHb) is paramagnetic and introduces magnetic-susceptibility-induced variation in the local magnetic field in and around blood vessels. In contrast, oxygenated hemoglobin (HbO<sub>2</sub>) is diamagnetic and exerts little effect on the local magnetic field. Because of this, the magnetic susceptibility difference between HbO<sub>2</sub> and the surrounding tissue is small (i.e., it exhibits low  $\Delta\chi$ ). As HbO<sub>2</sub> deoxygenates, magnetic field gradients are produced resulting in high  $\Delta\chi$  values across the interface between the vasculature and surrounding tissue. Thus, a change in hemoglobin oxygenation leads to changes in the local distortions of the externally applied magnetic field.

### 1.3. Magnetic-Susceptibility-Induced Signal Change

The local magnetic field disturbance caused by paramagnetic deoxyHb affects the NMR signal of the surrounding spins. Specifically, the large  $\Delta\chi$  causes accelerated loss of spin coherence resulting in shorter  $T_2^*$  relaxation times relative to those spins not affected by the susceptibility difference. This relaxation mechanism provides a means of localizing the effects of changes in hemoglobin oxygenation. From the hemodynamic response to local neuronal activation, an increased CBF and a corresponding decrease in OEF increases the concentration of HbO<sub>2</sub> in the capillary and venous vascular beds. Higher [HbO<sub>2</sub>], and consequently lower [deoxyHb],



reduces the  $\Delta\chi$  between the vasculature and surrounding tissue. This in turn increases the local effective intravoxel  $T_2^*$ , which leads to an increase in image intensity on  $T_2^*$ -weighted images (refer to Section 5.2 of Chapter 1 for further discussion of these points). The situation of higher venous  $[HbO_2]$  may also be considered in terms of a local decrease in  $T_2^*$  dephasing and less loss of phase coherence. Turner *et al.* (1991) demonstrated this effect using cats with induced hypoxia where it was found that MR signal intensity decreased with increasing deoxyHb and after oxygen was restored, signal intensity rose above the baseline level. Because more than 70% of the brain's blood lies within the microvascular capillaries and venules, the measurement of the magnetic-susceptibility-induced  $T_2^*$  signal loss is considered to predominantly reflect the regional deoxygenation state of the venous system (Bandettini *et al.*, 1992). Optical imaging techniques have demonstrated that subsequent to the onset of neural activity, there is a transient increase in the tissue concentration of deoxyHb caused by an increase in local oxygen consumption that precedes any change in blood flow or volume (Malonek *et al.*, 1996). This leads to a brief hypoxic state that is met with vasodilation of the arterioles, resulting in a large increase in CBF. The CBF increase generally overcompensates for the increase in local oxygen consumption and leads to blood hyperoxygenation and the standard positive BOLD response.

## 2. Characteristics of the BOLD Response Signal

An important limitation to BOLD-based fMRI is that the temporal resolution of the response signal is limited by the rate of the hemodynamic response, which occurs over a time course that is orders of magnitude slower than that of the neuronal response.

Temporal characteristics of BOLD signal change are often characterized by the time between stimulus onset and the point it reaches maximum amplitude (i.e., time to peak) as well as the time between stimulus cessation and the point it reaches baseline (i.e., time to fall). Temporal dynamics of the BOLD response vary across different neural tissue regions with time-to-peak values typically falling in the 5–8 sec range and time-to-fall values in the 5–9 sec range (Kwong *et al.*, 1992).

The technique also has low intrinsic signal-to-noise and contrast-to-noise, leading to the need for repetition of stimuli in order to decrease the variance of the results. The percent-signal change in activated brain regions is optimized by maximizing the contrast-to-noise ratio ( $CNR = \Delta s / \sigma_n$ , where  $\Delta s$  is the signal difference between tissue and noise, and  $\sigma_n$  is the standard deviation of noise), which is accomplished by matching the pulse sequence TE to the  $T_2^*$  of gray matter. At typical clinical-scanner field strength (i.e.,  $B_0 = 1.5T$ , which was strength of the scanner used in the experiments of the following chapter of this dissertation), the percent change in signal has been demonstrated to fall in the range of 1–5% (Kwong *et al.*, 1992). Since the effect of  $\Delta\chi$  is more pronounced at high field strength, the observed  $T_2^*$  induced signal change is correspondingly increased at higher field, in the range of 5–20% at 4T (Ogawa *et al.*, 1992).

The indirect coupling between neuronal activity and the observed NMR signal change also has implications with regard to the resolvable spatial resolution of BOLD-contrast-derived, neuronal-activation maps. Since the signal change is a result of a perfusion increase that is local to the tissue of interest, but is generally on a larger spatial scale than

the electrical activity, the site of the activation on an image may be somewhat larger than and distant from the site of neural activity.

### 3. Detection of Neuronal Activation

#### 3.1. Block Design Experiment

The most common experimental design applied in fMRI today is the blocked-task paradigm. In this approach, a series of trials of a continuous task are presented during a discrete epoch of time. This is followed by a transition to performing trials of a different task over another epoch of time. This experimental scheme is diagrammed in Fig. 6.1 where a 'control' task and an 'active' task are alternately performed over a 45-sec epoch. The strategy behind this approach is to isolate the cognitive process of interest and design control and active phases of the experiment that differ with respect to that process. This method is therefore limited to finding relative changes between task functions, however, the great flexibility inherent to the blocked paradigm design allows for a large range of parameter manipulation in the study design; for example, variation of the epoch timings or number of cycles in the paradigm; variation of stimulus duration and/or interstimulus interval during the control or active phases of the paradigm.

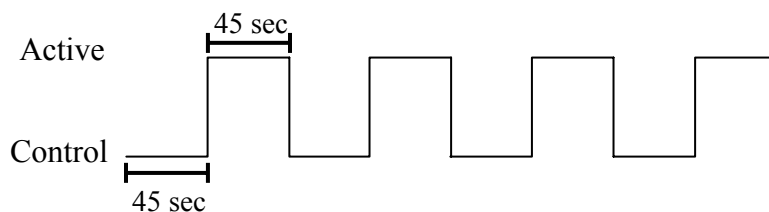


Figure 6.1 – Diagrammatic example of the timing in a four-cycle blocked-task paradigm. In this example, subjects are presented with the control task over the initial 45 sec of the paradigm. This is followed by 45 sec of the active component of the paradigm, which incorporates a task involving the cognitive process of interest that is not present in the control task. These two phases are then alternately repeated over the duration of the paradigm presentation.

### 3.2. fMRI Data Analysis

The number of methods available for analysis of fMRI data is large and growing as the technology and applications evolve. The choice of analysis method is highly dependent on the design of the experiment and the questions to be asked of the data. The most straightforward approach for analysis of the block design experiment is the univariate (i.e., pixel-by-pixel) subtraction analysis. In this method, average values for baseline (i.e., control) periods are subtracted from those of the corresponding active periods. A hypothesis test is then performed between the resulting difference values and zero to determine if there is a statistically significant difference in signal between the two periods.

In another data analysis-approach, a model of the expected temporal response is created and then fit to the time-course data. As with the subtraction analysis, this approach is also normally employed as a univariate analysis. Consider the time course of a single voxel,  $y(t)$ , as a 1-D vector of signal intensity values. In a simple

example of linear modeling, the time-course vector is related to the model time course,  $r(t)$ , (or reference waveform) as in:

$$y(t) = \alpha r(t) + c + \varepsilon(t) \quad (6.1)$$

where  $r(t)$  is also a 1-D vector that may replicate the square-wave block design of Fig. 6.1 in terms of a binary series. The value  $\alpha$  represents the parameter estimate for  $r(t)$ ;  $c$  is a constant that corresponds to the baseline intensity of the data; and  $\varepsilon(t)$  is the term that accounts for the residual error between the fitted model and the data. A pictorial interpretation of the relationship between the terms of Eq. (6.1) is provided in Fig. 6.2 to further illustrate these concepts. Thus, the model fitting involves adjusting the baseline level and the height of the square wave to best fit the data.

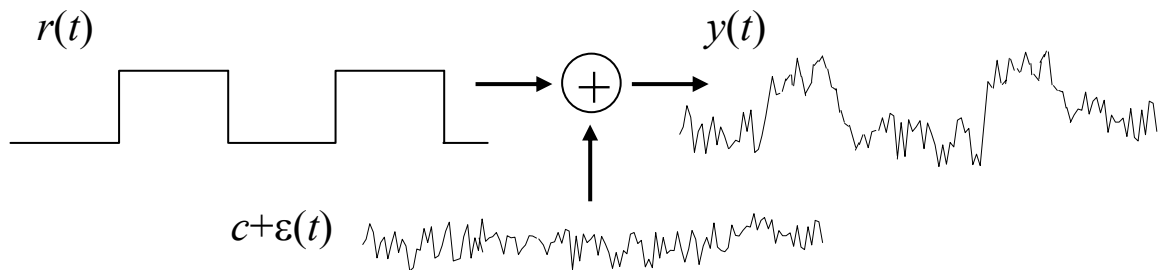


Figure 6.2 – Illustration of the relationship between the reference waveform,  $r(t)$ , baseline and error term,  $c + \varepsilon(t)$ , and the voxel time course,  $y(t)$ .

Bandettini *et al.* (1993) introduced calculation of the cross-correlation coefficient,  $\rho$ , between a reference waveform and a voxel time course:

$$\rho = \frac{\sum_{i=1}^N (y_i - \bar{y})(r_i - \bar{r})}{\left[ \sum_{i=1}^N (y_i - \bar{y})^2 \sum_{i=1}^N (r_i - \bar{r})^2 \right]^{1/2}} \quad (6.2)$$

where  $y_i$  and  $r_i$  represent individual time points in a series of  $N$  points for the voxel- and reference-waveform time courses, respectively; values  $\bar{y}$  and  $\bar{r}$  are the average values of their respective time course. This calculation is employed in the analysis of the functional imaging experiments presented in the following chapter of this dissertation.

### 3.3. Statistical Inference

An important complication that must be addressed prior to making valid statistical inference from the functional imaging time course data is that large numbers of voxels are simultaneously being assessed for change. For a given functional imaging data set with  $N$  independent voxels (for example, a common acquisition from our whole brain studies consists of 24 image slices at a resolution of  $64 \times 64 \rightarrow 98,304$  voxels), assuming a threshold for significance of change in each of the individual voxels of  $p = 0.01$  leads to an average of  $N \times 0.01$  voxels classified as statistically significant by chance alone (983 voxels in our example) – even if no stimulation is applied. This exemplifies the degree to which the problem of multiple comparisons can affect the analysis and interpretation of fMRI data. A typical approach for reducing the number of false positives is through Bonferroni correction where the significance level at each voxel is divided by the number of comparisons made (i.e., the number of voxels in the dataset). However, for the large  $N$  of most fMRI

datasets, this results in an excessively stringent threshold (for our example, a Bonferroni-corrected  $p$  threshold of  $0.01/98,304 = 0.0000001$ ).

Another approach to the multiple comparisons problem is advocated by Genovese *et al.* (2002), where an appropriate threshold is applied by controlling the fraction of significant voxels that are falsely significant. The false discovery rate (FDR) is the proportion of false positives (i.e., incorrect rejections of the null hypothesis) among those tests for which the null hypothesis is rejected. Controlling the FDR is a compromise between the loss of statistical power of the Bonferroni method, which controls the rate of false positives among all tests, whether or not the null is actually rejected, and the large number of potential false positives that arise by chance from the multiple comparisons.

The FDR control techniques introduced by Benjamini and Hochberg (1995) were used to threshold the statistical parametric maps generated by the experimental paradigms presented in the work of Chapter 7 of this dissertation. The general procedure for controlling the FDR in the  $N$  voxels (with their associated  $p$  values derived from an appropriate statistical test) being tested is as follows: (1) select the maximum average FDR (a parameter referred to as  $q$ ) that is desired for the experiment; (2) order the  $p$  values from smallest to largest; (3) find  $r$  that is the largest  $i$  in the  $p$  value sequence for which

$$p_i \leq \frac{i}{N} \frac{q}{c(N)} \quad (6.3)$$

where  $c(N)$  is a predetermined constant that is dependent on assumptions made about the distribution of  $p$  values across the voxels; (4) declare the voxels  $v_1 \rightarrow v_r$  to be active. For our experiments, we use a value of  $c(N)$  that makes no assumptions regarding independence of the voxels or the distribution of noise in the data and is calculated as:

$$c(N) = \sum_{i=1}^N \frac{1}{i} \quad (6.4)$$

A final point regarding implementation of the FDR procedure is to mention that it operates simultaneously on all voxels included in the analysis. For this reason, prior to FDR thresholding the statistical parametric map data, it is necessary to implement a procedure to remove those voxels that are known to not contribute any activation to the output (i.e., air surrounding the head, the skull and CSF of the ventricles) so as to increase the power of the procedure.



# Chapter 7

## Dynamic Changes in Neural Network Activation Patterns

---

Introduction  
Methodology  
  Data Acquisition  
  Subject Population  
  Temporal Analysis of Activation  
  Simple Motor Function  
  Semantic Reasoning  
  Visuospatial Processing  
  Working Memory  
  Temporal Analysis of Activation  
    Refinement

Results  
  Simple Motor Function  
  Semantic Reasoning  
  Visuospatial Processing  
  Working Memory  
Discussion  
  Simple Motor Function  
  Semantic Reasoning  
  Visuospatial Processing  
  Working Memory  
  Heterogeneous BOLD Response  
Conclusions

---

## 1. Introduction

Neuroscientists with the aim of understanding the relationship between brain and behavior have found fMRI to be a valuable research tool in the localization of neural function. With the continued development of analysis techniques, researchers in the field have recently tackled more demanding questions regarding the understanding of mechanisms of learning (Karni *et al.*, 1995) and defining cognitive processing networks (McIntosh *et al.*, 1998). The primary aim of the latter is to determine how brain regions interact to create a processing network used during cognitive tasks. Using standard methods to identify at least a portion of the regional nodes in a cognitive network, analytical techniques can then be applied to define the functional interrelations between activated regions. Methods such as structural equation modeling (McIntosh *et al.*, 1994), path analysis (Bullmore *et al.*, 2000) or independent component analysis (McKeown, 2000) provide measures of the strengths of the correlations between activation changes in different brain regions. The primary drawback to these methods, however, is the requirement of *a priori* information of the participating regions and the underlying anatomical model for the network. Additionally, they do not consider variation within a node of the network over time, which may result in loss of dynamic information within a network node. Rao *et al.* (2001) have presented an event-related method used to evaluate the time course of activation in different neural regions associated with time perception. They demonstrate a dynamic network of cortical-subcortical activation within the different regions associated with temporal information processing. However, this method is not applicable to the study of the temporal dynamics of brain activation patterns from a sustained activity. Therefore, the purpose of this study was to determine if volumes of activated brain regions change during a sustained task. We demonstrate examples of a

simple method for observing the evolution of activity in regions associated with a cognitive network with the goal of providing additional understanding of the connectivity and interactions that evolve between regions during a sustained activity.

In this work, we present a method to observe the evolution of neural activity within a given activation region during sustained task performance. We hypothesize that the analysis method will show regions of neuronal activation that adapt to the demands of a given task stimulus through either recruitment or discharge of adjacent areas of tissue. To assess the robustness of the method, we demonstrate application of the technique to four different task paradigms. Neural activation patterns from each paradigm are anticipated to encompass different brain regions that involve different neural networks. The four paradigms include: (1) simple motor function; (2) semantic reasoning; (3) visuospatial processing; and (4) working-memory (WM).

From the simple motor function paradigm, we anticipate activation in regions of the motor function control network, which encompasses bilateral regions in frontal and parietal cortex, basal ganglia, thalamus and cerebellum. In previous motor-function studies, different paradigms have revealed task specific patterns of activation in appropriate brain regions (Rao *et al.*, 1993).

The semantic reasoning paradigm gauges subjects' ability to make associations between words and their meaning. This paradigm was developed as a verbal categorization task, which requires subjects to (a) recognize the presented word; (b) retrieve from memory an

association between the word and a category that is used to (c) guide a decision and response. We anticipate regions of activation for this task to encompass word association regions of the left hemisphere and portions of the prefrontal cortex involved in executive function and decision-making.

The visuospatial task was implemented as an fMRI paradigm based on modification of the Wechsler Adult Intelligence Scale (WAIS-III), a widely used pencil-and-paper test of non-verbal intelligence. This paradigm requires subjects to (a) visually scan and encode into iconic memory different symbol patterns; (b) compare the different symbols to one another, visually scanning for symbols that match; (c) guide a decision and appropriate motor response based on the decision. We anticipate regions of activation for this task in the primary and secondary visual cortex, posterior parietal cortex and portions of the prefrontal cortex involved in executive function and decision-making.

The WM paradigm is a verbal WM task employing the *N*-back routine. The *N*-back is considered a WM task because it entails temporary storage and manipulation of information to guide behavior (Baddeley, 1992). Specifically, the *N*-back task requires (a) encoding a stimulus into memory; (b) maintaining a representation of the stimulus in memory while a subsequent stimulus is presented and also encoded in memory; (c) simultaneously with (b), a previous stimulus must be recalled from memory for use in (d), where a decision is made between the recalled stimulus and the currently presented stimulus to guide a motor response; (e) active removal of an old stimulus from the

hierarchy of stimuli in WM. Verbal WM tasks have previously shown neural activation involving several bilateral areas in the frontal and parietal cortex.

## 2. Methodology

### 2.1. Data Acquisition

All MRI data were acquired with a 1.5T GE Signa-LX scanner (GE Medical Systems, Milwaukee, WI) using a standard RF quadrature head volume (birdcage) coil. High-resolution [(256 × 256, 24 cm × 24 cm), 1.5 mm slice thickness], T<sub>1</sub>-weighted sagittal plane images were acquired with a spoiled GRASS sequence (TR/TE = 22/5 msec,  $\theta = 22^\circ$ , NEX = 1) for anatomic localization of functional activation. Data were acquired during runs of the functional tasks using a GRE-EPI sequence (TR/TE = 3000/60 msec,  $\theta = 90^\circ$ ) with contiguous axial slices positioned to cover the entire brain volume [(64 × 64, 24 cm × 24 cm), 5 mm slice thickness, generally 25–28 slices]. All task instructions and stimuli were presented to the subjects visually by back-projecting information on a screen placed at the foot of the scanning table. Subjects were able to view the screen using a mirror built into the RF head coil positioned above their eyes and angled out the bore of the magnet.

### 2.2. Subject Population

Subjects participating in these experiments were all healthy, normal, right-hand dominant adults aged 20-62 (mean=36). Not all experiment paradigms were administered to all subjects.

### 2.3. Simple Motor Function

During the simple motor function task, subjects were instructed to repetitively open and close their right hand at a self-paced, consistent rate over a 45-sec period. The opening/closing activity was alternated with a 45-sec rest phase in a four-cycle blocked-paradigm over a six-minute period (i.e., 120 repetitions of the 3-sec TR GRE-EPI acquisition). Subjects repeated two runs of this task and the data were concatenated to produce one contiguous dataset for analysis.

### 2.4. Semantic Reasoning

The semantic reasoning experiment is a self-paced task developed as a test of verbal categorization. Categorization tests are often administered to patients as a component to a battery of tests used to make a neuropsychological assessment (Kolb *et al.*, 1990). Figure 7.1 provides examples of the tasks involved in this paradigm. During the control task, a series of upper-case nonsense words was presented with a matching lower-case nonsense word and a foil located on the left or the right side of the slide. The subject was instructed to match their response via a two-button finger-response keypad to the side of the slide that the matching lower-case nonsense word appeared. During the verbal categorization component of the paradigm, a series of noun words was presented. For each noun presented, a decision was made regarding whether the word represents a living or a non-living object. Based on the decision, the subject responded via finger-response keypad. An appropriate button response was dependent upon which side of the slide the decision category was located. For example, in the first slide of the verbal categorization task in Fig. 7.1, a 'worm' is a living object and the living (L) flag is located on the left side of the slide, therefore,

the correct response is the left button. This component of the task was included in effort to negate the effects of the visual scanning aspect of the control task. Both tasks were self-paced by the subject over a period of 45 sec. The tasks were alternately performed during 45-sec intervals in a four-cycle blocked-paradigm over a six-minute period (i.e., 120 repetitions of the 3-sec TR GRE-EPI acquisition). Subjects repeated two runs of this paradigm and the data were concatenated to produce one contiguous dataset for analysis.

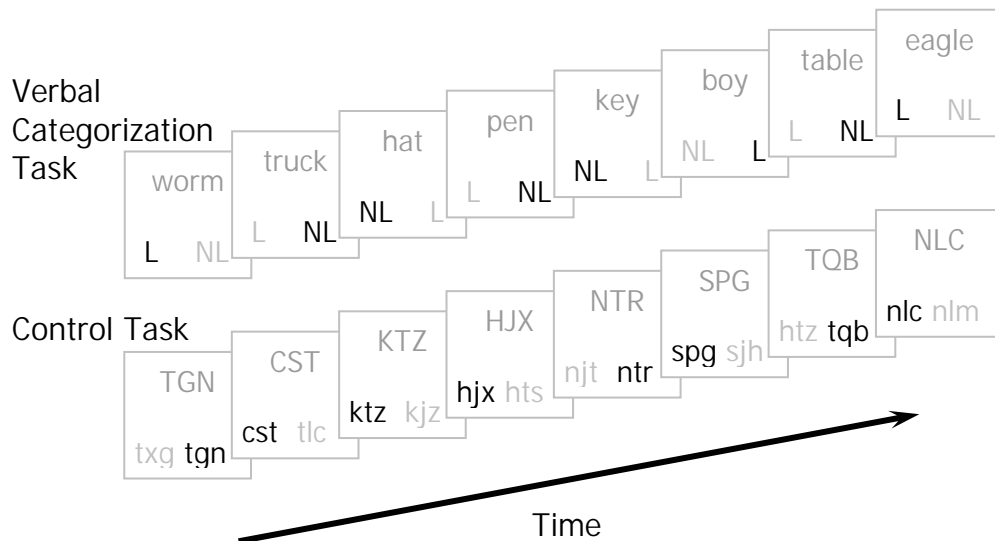


Figure 7.1 – Example word sequence in the verbal-categorization and control-task components of the self-paced semantic reasoning paradigm. During the control task, subjects indicate which lower-case nonsense word matches the upper-case target nonsense word. An appropriate left- or right-button response is dependent on which side of the slide the matching nonsense word is located. In the verbal categorization task, a decision is made regarding whether the presented noun is a living (category flag ‘L’) or a non-living object. The appropriate left- or right-button response is dependent on which side of the slide that the correct category is located. For the instructional purposes of this example, the darker colored category flag denotes the correct response for each slide.

## 2.5. Visuospatial Processing

The visuospatial processing paradigm presented here is an adaptation of a widely used pencil-and-paper test of non-verbal intelligence: Wechsler Adult Intelligence Scale (WAIS-III). Figure 7.2 provides examples of the tasks involved in this paradigm. During the control task, a series of symbol groupings, arranged with two symbols located in one row and five symbols in a row beneath them, was presented with one symbol in either grouping missing. The subject was instructed to respond via a two-button finger-response keypad by matching the button pressed to the side of the slide with the missing symbol. During the symbol-search component of the paradigm, a series of symbol groupings, arranged in the same manner as the control task, was presented where either symbol from the top grouping was a target for a possible match in the bottom grouping. The subject was instructed to indicate whether one of the target symbols from the top grouping was located in the bottom grouping via a left button press for a positive match and a right button press for no match. Both tasks were self-paced by the subject over a period of 45 sec. The tasks were alternately performed during 45-sec intervals in a four-cycle blocked-paradigm over a six-minute period (i.e., 120 repetitions of the 3-sec TR GRE-EPI acquisition). Subjects repeated two runs of this paradigm and the data were concatenated to produce one contiguous dataset for analysis. Our adaptation of the WAIS-III differs slightly from the standard exam in terms of how the symbol groupings are arranged in their presentation. In the standard exam, the target symbols are located horizontally from the choice symbol group; whereas in the modified version we present to subjects, the symbol groups are vertically offset from one another. We do not expect this modification to have a severe effect on subject performance, as the



geometry of the symbols is, in general, of sufficient complexity to enforce a memory component to the task.

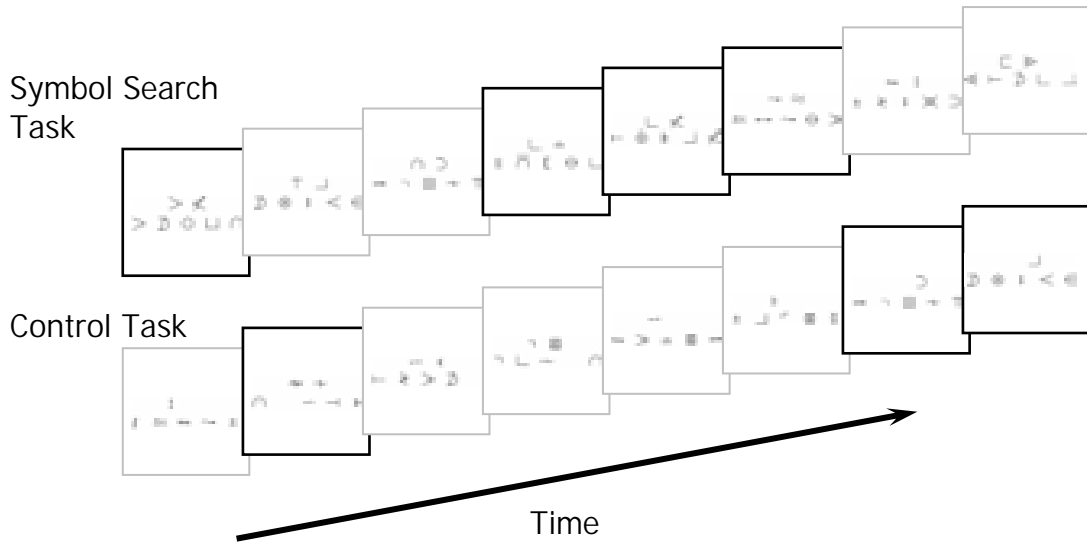


Figure 7.2 – Example sequence of slides presented in the symbol-search and control-task components of the self-paced visuospatial processing paradigm. During the control task, subjects visually scan each slide to determine on which side the missing symbol is located. A two-button finger-response keypad is used to record subject responses whereby the button corresponding to the side of the slide with the missing symbol (i.e., left or right) is pressed. During the symbol-search component of the paradigm, subjects visually compare symbols from the top grouping (the target grouping) for a possible match in the bottom grouping. Subjects indicate whether one of the target symbols is located in the bottom grouping via a left button press for a positive match and a right button press for no match. For the instructional purposes of this example, a darker outlined slide denotes a symbol missing from the left half of the screen during the control task and a positive target match during the symbol search task.

## 2.6. Working Memory

As demonstrated in Fig. 7.3, a common 2-back task was used in the WM paradigm.

During the 2-back task, a series of consonant letters were presented (0.5-sec-stimulus duration, 2.5-sec inter-stimulus interval) and the subject responded via a two-button finger-response keypad following each letter, indicating whether the current letter matched the one presented two letters earlier. During the control condition, a series

of consonant letters was presented (following the same timing interval as used during the 2-back task) and the subject indicated whether the presented letter matched a predetermined target letter. Thus, the control task featured the same sensory and motor components as the 2-back task while minimizing WM demands. For either condition, the subject was instructed to disregard the case of the presented letter such that a positive match should be indicated for a given letter presented in either upper or lower case. The 2-back task and control conditions were alternately performed during 45-sec intervals in a four-cycle blocked-paradigm over a six-minute period (i.e., 120 repetitions of the 3-sec TR GRE-EPI acquisition). Subjects repeated two runs of this paradigm and the data were concatenated to produce one contiguous dataset for analysis.

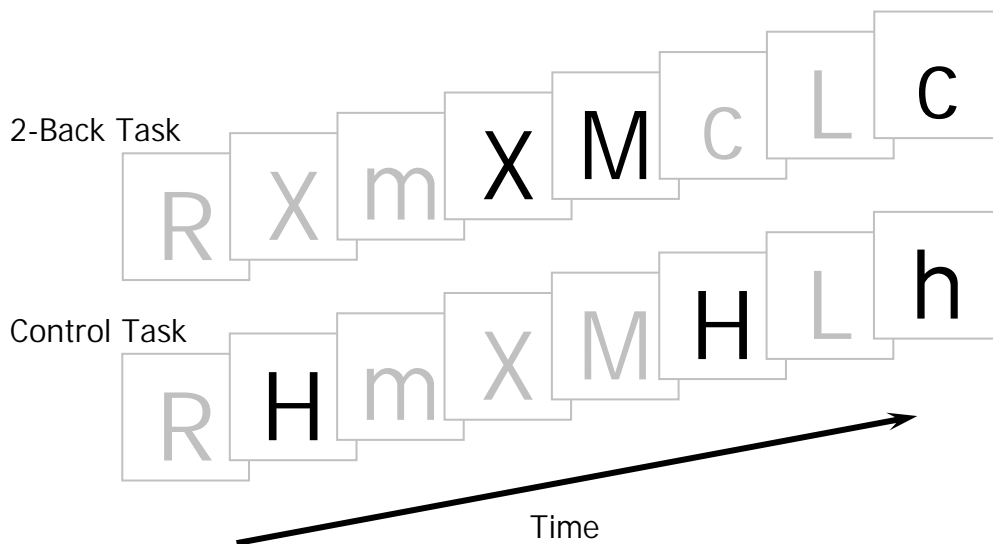


Figure 7.3 – Example letter sequence in the 2-back and control-task components of the working memory paradigm. For each letter presented, subjects make a yes/no decision based on the task instructions. In the control task, a positive response is when the presented letter matches a predetermined target letter (for the case above, the letter ‘h’ is the target). In the 2-back task, a positive response is indicated when the current letter matches the one presented two earlier. For the instructional purposes of this example, a darker colored letter denotes a positive response for each task.

## 2.7. Temporal Analysis of Activation Refinement

All fMRI data were analyzed using AFNI (Cox, 1996). For each subject, time-series images were spatially registered to minimize effects of head motion. The two individual runs of each 4-cycle task were concatenated to produce a single dataset of 240 repetitions. With the concatenated dataset, cross-correlation analysis was performed against ideal waveforms created by dividing the stimulus epochs into subsets of TRs with each of the control epochs maintained whole (refer to the diagrams of Fig. 7.4). The four intervals from the active periods of the task are referred to as individual ‘fourths’ and we refer to this procedure as a ‘fourths-analysis’. Correlation-coefficient maps obtained from each of the ideal waveforms were thresholded for statistical significance using a routine written to control the false discovery rate (Genovese *et al.*, 2002). The threshold applied to the simple motor function was at the 0.001 level and for the three other paradigms at the 0.01 level. Individual subject anatomical and functional images were then interpolated to volumes with 1 mm<sup>3</sup> voxels, co-registered, transformed to standard Talairach coordinate space (Talairach *et al.*, 1988) and spatially smoothed using a 4-mm Gaussian FWHM filter.

To obtain information regarding the group response to a given stimulus paradigm, individual, spatially-normalized (i.e., transformed to Talairach coordinate space), subject correlation data sets were grouped by averaging their thresholded data sets, yielding averaged activation maps for each subset of the stimulus epoch. The information we were interested in observing from this analysis approach was the

location of the activation and observing how the volume of activation varied over the duration of the active task epoch. For this reason, activity in the subject-averaged output was classified in a binary (on or off) manner.

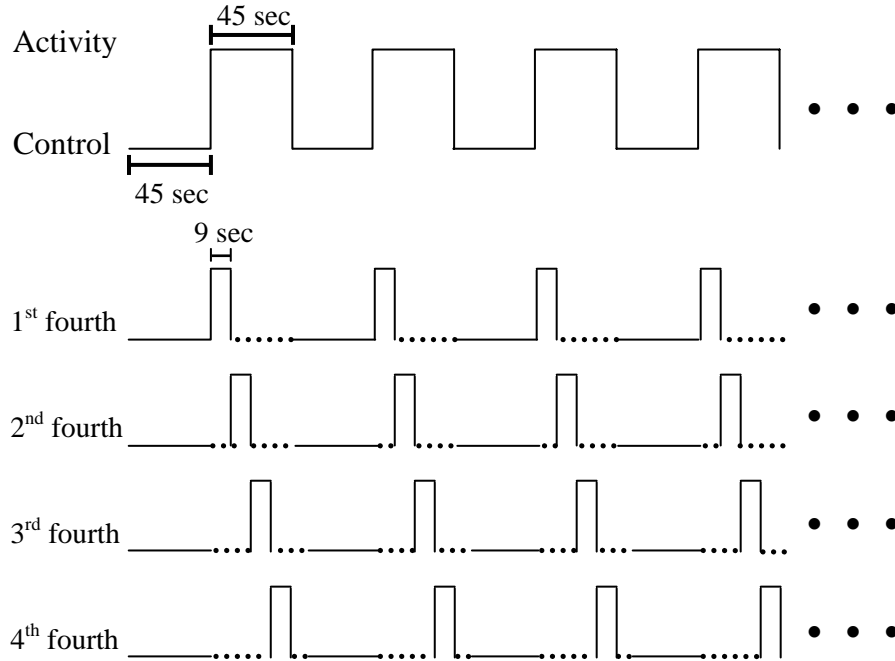


Figure 7.4 – Demonstration of subdivision of 4-cycles of the active epochs in the blocked paradigm into ‘fourths’ for analysis of the temporal evolution of activation refinement over the duration of the sustained task. The dots at the end of the cycles represent continuation of the process over the remaining 4-cycles of the concatenated 8-cycle dataset.

### 3. Results

Output from each of the stimulus paradigms administered in these studies was found to yield task specific regions of activity. Averaged summary maps of activation are provided for each of the respective paradigms in the figures that follow. These figures are presented with the functional-activation maps overlaid on an averaged high-resolution anatomical data set to aid spatial localization of the active region.

### 3.1. Simple Motor Function

Activation output from the fourths analysis of the simple motor function paradigm is shown in Fig. 7.5. The regions of activation in this figure represent the FDR thresholded ( $q = 0.001$ ) correlation output averaged from ten subjects, overlaid on the average of their anatomical data. Axial plane images (3-mm offset between slices) and the corresponding volume renderings with cutouts positioned to highlight medial frontal and left hemisphere features of the activation output are provided from each of the four time interval segments in sequential order from (A.) – (D.). Activation during the first time interval is localized completely in the medial frontal and left hemisphere dorsolateral prefrontal cortex (DLPFC), areas consistent with initiation and execution of motor plans, respectively. During the subsequent time intervals, activation in these two regions persists and remains relatively constant in volume. By the second interval, spurious areas of bilateral activation in the inferior parietal lobes are observed that persist and, in some cases, expand over the course of the remaining intervals.

In contrast to the activation patterns from the fourths analysis, Fig. 7.6 demonstrates regions of activation generated from correlation analysis against the entire stimulus presentation waveform using the same subject data as used in the fourths analysis of Fig. 7.5. Regions of activation here, in general, mimic those noted in the fourths analysis with the addition of activity in the right hemisphere DLPFC area and greater extent of activation in regions of inferior parietal and subcortical nuclei.

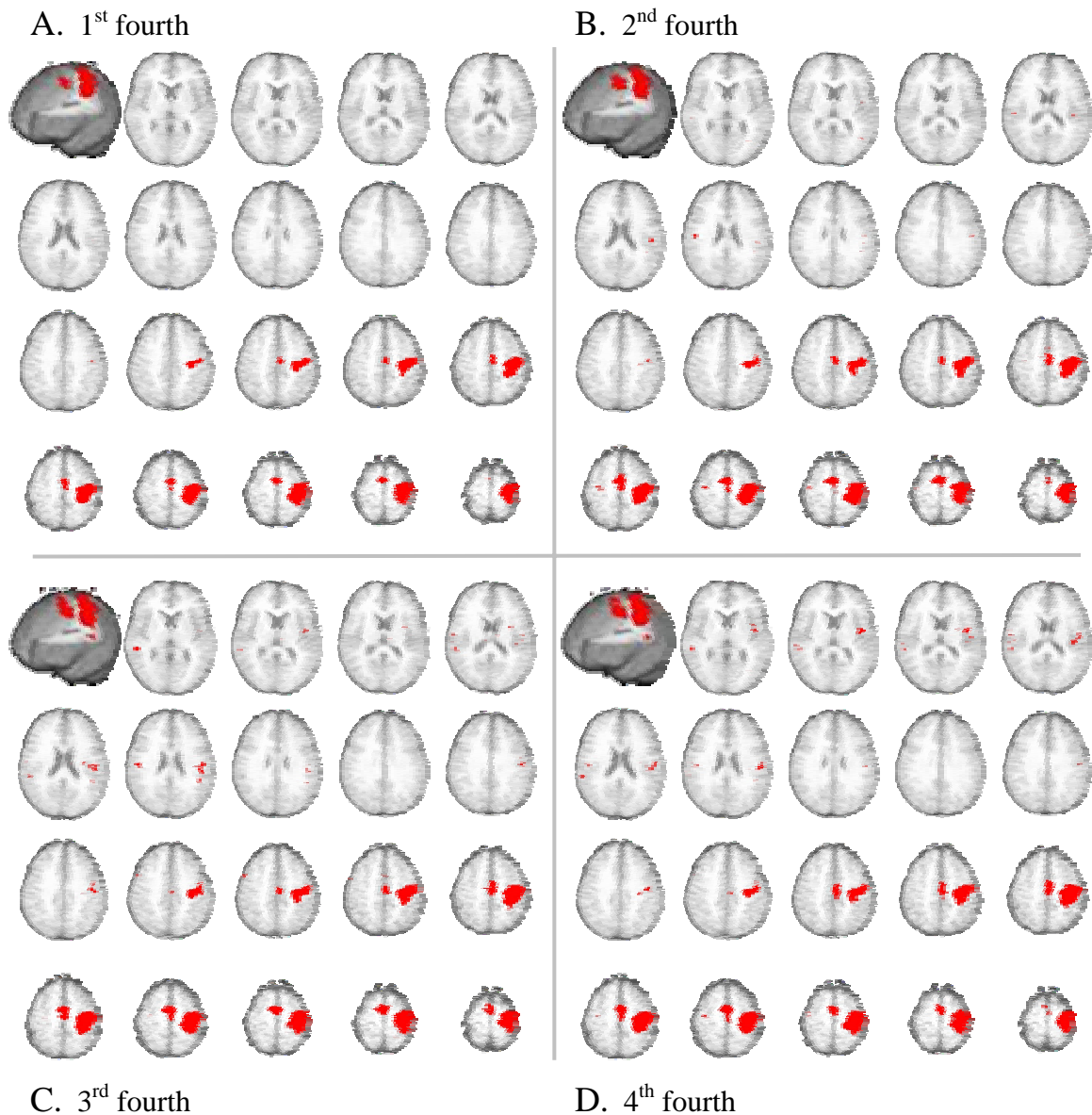


Figure 7.5 – Activation output from the fourths analysis of the simple motor function paradigm. The regions of activation represent the FDR thresholded ( $q = 0.001$ ) correlation output averaged from  $N = 10$  subjects, overlaid on the average of their anatomical data. Axial-plane images and the corresponding volume renderings with cutouts positioned to highlight selected features of the activation output are provided from each of the four time interval segments in sequential order from (A.) – (D.). Axial-plane images are shown with a 3-mm slice offset from one another.

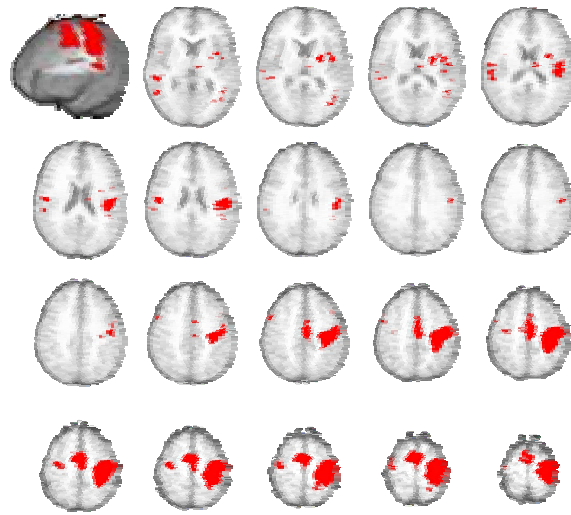


Figure 7.6 – Simple motor paradigm activation output generated from correlation analysis against the entire stimulus presentation waveform. The regions of activation represent the FDR thresholded ( $q = 0.001$ ) correlation output averaged from  $N = 10$  subjects, overlaid on the average of their anatomical data. Axial-plane images shown with a 3-mm slice offset from one another and the cutout in the volume rendering is positioned to highlight left-hemisphere and medial-frontal activation.

### 3.2. Semantic Reasoning

Output from the fourths analysis of the semantic reasoning paradigm (Fig. 7.7)

shows activation in areas consistent with the language network and decision-making aspects of the task. The regions of activation in this figure represent the FDR thresholded ( $q = 0.01$ ) correlation output averaged from eight subjects. Axial plane images (3-mm offset between slices) and the corresponding volume renderings with cutouts positioned to highlight selected features of the activation are provided from each of the four time interval segments in sequential order from (A.) – (D.).

Activation during the first time-interval is noted in bilateral regions of the temporal-parietal-occipital region, consistent with areas of language and reading comprehension. Over the time intervals, activation in these regions appears to

completely dissipate from the right hemisphere, but a slight activation volume persists in the left hemisphere region. By the second time interval, a volume of activation in the left inferior frontal gyrus, consistent with language generation areas, begins to develop. Activation in this region grows in volume over the third and fourth intervals. Similarly, activation in the DLPFC of the left hemisphere and the medial prefrontal region begins to develop during the second interval and continues to grow in volume throughout the remaining intervals with activation in the right DLPFC noted by the fourth time interval. Activation in these areas is consistent with the initiation and motivational (medial prefrontal) and prioritization and decision-making (DLPFC) aspects of the task demands.

For comparison, regions of activation generated from correlation analysis against the entire stimulus presentation waveform are provided in Fig. 7.8 from the same subject data as used in the fourths analysis of Fig. 7.7. From this data, we note more extensive regions of activation in the left inferior frontal gyrus than seen from the fourths analysis. The extent of activation in the medial frontal and bilateral regions of the DLPFC, however, appear similar to that generated with the fourths analysis.



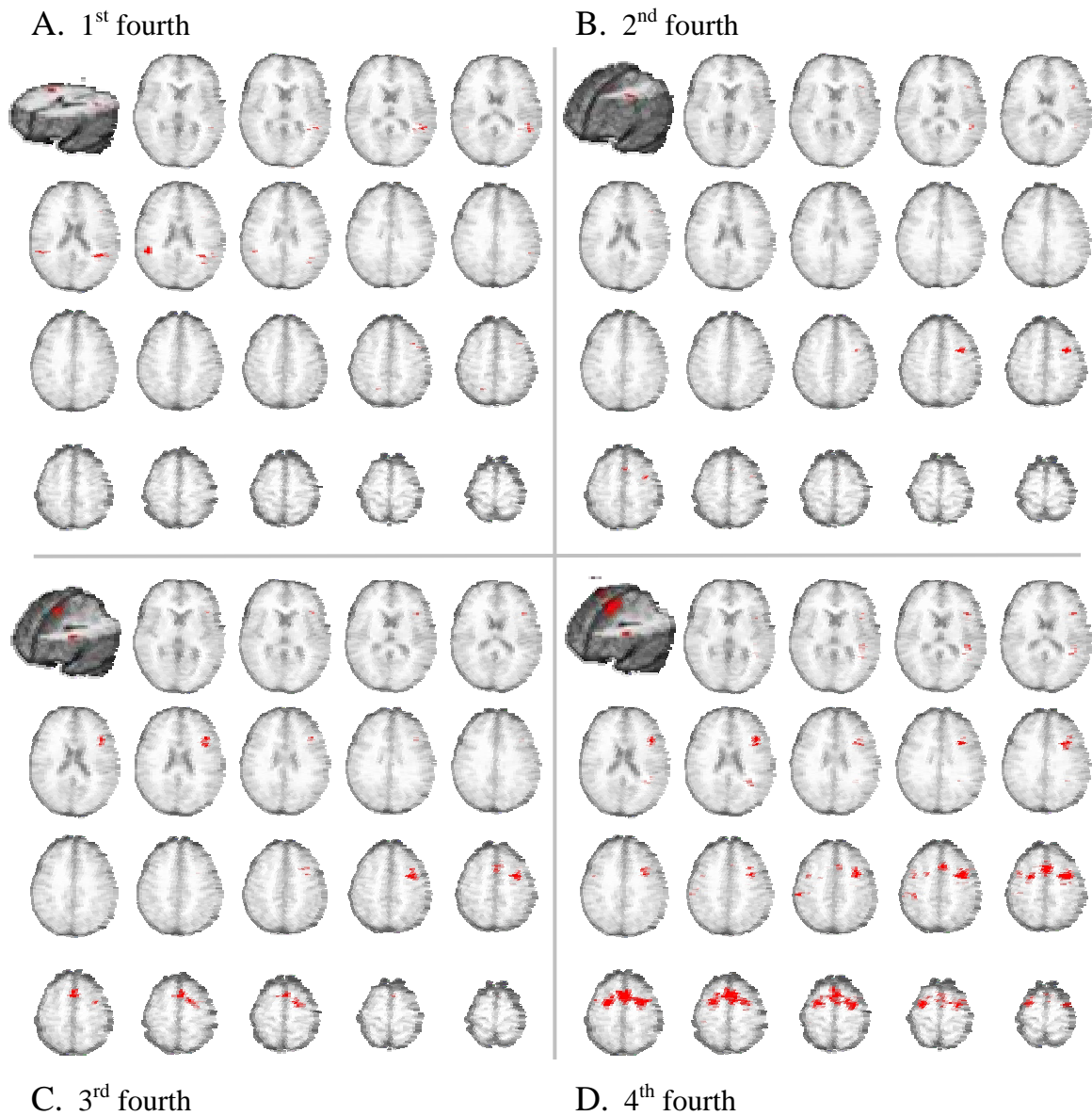


Figure 7.7 – Activation output from the fourths analysis of the semantic reasoning paradigm. The regions of activation represent the FDR thresholded ( $q = 0.01$ ) correlation output averaged from  $N = 8$  subjects, overlaid on the average of their anatomical data. Axial-plane images and the corresponding volume renderings with cutouts positioned to highlight selected features of the activation output are provided from each of the four time interval segments in sequential order from (A.) – (D.). Axial-plane images are shown with a 3-mm slice offset from one another.

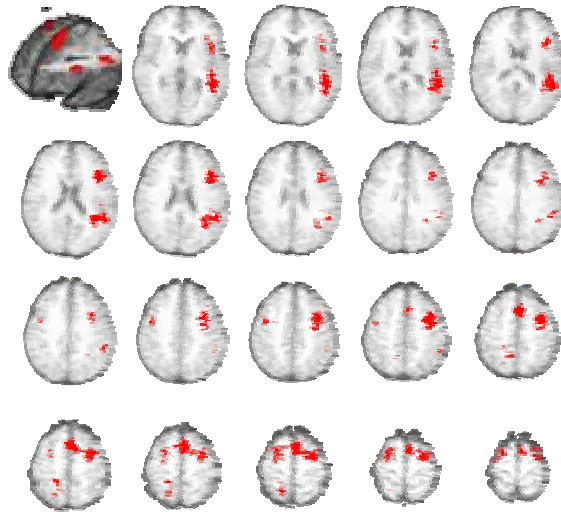


Figure 7.8 – Semantic reasoning paradigm activation output generated from correlation analysis against the entire stimulus presentation waveform. The regions of activation represent the FDR thresholded ( $q = 0.01$ ) correlation output averaged from  $N = 8$  subjects, overlaid on the average of their anatomical data. Axial-plane images shown with a 3-mm slice offset from one another and the cutout in the volume rendering is positioned to highlight left hemisphere and medial frontal activation.

### 3.3. Visuospatial Processing

Output from the fourth analysis of the visuospatial processing paradigm (Fig. 7.9) shows activation in areas consistent with the visual, working memory and decision-making aspects of the task. The regions of activation in this figure represent the FDR thresholded ( $q = 0.01$ ) correlation output averaged from nine subjects. Axial-plane images (3-mm offset between slices) and the corresponding volume renderings with cutouts positioned to highlight occipital lobe and left hemisphere regions of activation output are provided from each of the four time interval segments in sequential order from (A.) – (D.). A large volume of activation is noted in the occipital lobe region during the first time interval. Activation in this region dissipates over the time intervals, but a core volume remains through the later

intervals in areas consistent with primary visual processing. Regions of activation in the left hemisphere inferior frontal and posterior parietal lobes are noted during the first time interval to progressively increase in volume throughout the remaining intervals and, during the third interval, homologous regions in the right hemisphere appear active. The activity in the inferior frontal and posterior parietal regions is consistent with, respectively, the executive control and iconic working memory aspects of the task demands. Also during the second interval, activity in the left hemisphere DLPFC region is noted. By the third interval, activity in this region expands concurrent with the onset of medial frontal and right hemisphere DLPFC activity – regions of activity consistent with the initiation and decision making aspects of the visuospatial processing task.

In contrast, regions of activation generated from correlation analysis against the entire stimulus presentation waveform are provided in Fig. 7.10 from the same subject data as used in the fourths analysis of Fig. 7.9. From this data, we note activation in the occipital lobe region that is similar to the fourths output.

Additionally, we note a number of areas with bilateral activity: inferior frontal cortex, posterior parietal cortex, and DLPFC. Also noted are anterior and posterior regions of medial frontal activation.

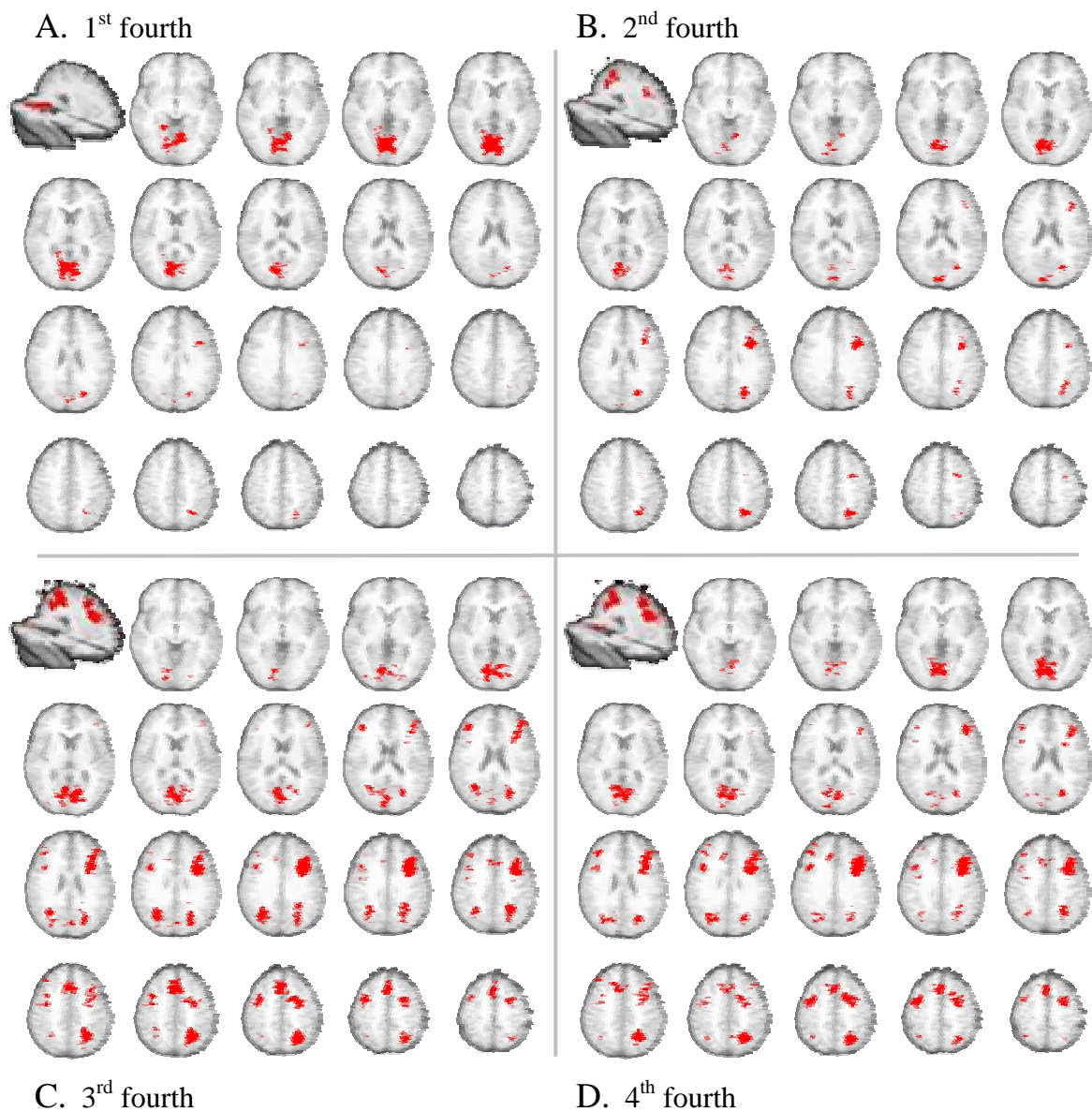


Figure 7.9 – Activation output from the fourths analysis of the visuospatial processing paradigm. The regions of activation represent the FDR thresholded ( $q = 0.01$ ) correlation output averaged from  $N = 9$  subjects, overlaid on the average of their anatomical data. Axial-plane images and the corresponding volume renderings with cutouts positioned to highlight selected features of the activation output are provided from each of the four time interval segments in sequential order from (A.) – (D.). Axial-plane images are shown with a 3-mm slice offset from one another.

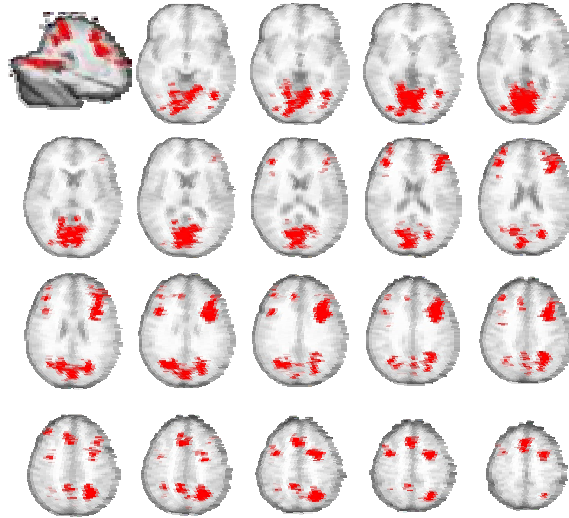


Figure 7.10 – Visuospatial processing paradigm activation output generated from correlation analysis against the entire stimulus presentation waveform. The regions of activation represent the FDR thresholded ( $q = 0.01$ ) correlation output averaged from  $N = 9$  subjects, overlaid on the average of their anatomical data. Axial-plane images shown with a 3-mm slice offset from one another and the cutout in the volume rendering is positioned to highlight occipital lobe and left hemisphere dorsolateral prefrontal cortex activation.

### 3.4. Working Memory

Output from the fourth analysis of the 2-back WM paradigm (Fig. 7.9) shows activation in areas consistent with the visual, working memory and decision-making aspects of the task. The regions of activation in this figure represent the FDR thresholded ( $q = 0.01$ ) correlation output averaged from 17 subjects. Axial-plane images (3-mm offset between slices) are provided from each of the four time interval segments in sequential order from (A.) – (D.). Sparse activation in the posterior parietal regions is noted during the initial time interval, consistent with regions responsible for iconic working memory function. By the second interval, activation has greatly expanded throughout the posterior parietal and frontal lobe regions, consistent with the iconic working memory and executive control aspects of the 2-back task. Over the course of the remaining intervals, the activation remains well

localized to the regions previously mentioned, but it appears that the activity expands to encompass greater volumes of brain. Figure 7.12 summarizes the measures of behavioral response accuracy as a percentage of the correct positive and correct negative responses over the four temporal intervals. Repeated measures ANOVA performed on the response data was found to indicate significant differences within each response category ( $P < .001$ ). In post-hoc t-test analysis between the different time intervals, a number of pairwise comparisons were found to be significantly different ( $P < .02$ ) and are indicated by the bracketed pairings. The significant differences between accuracy response scores over the time intervals are consistent with a decrease in subject performance in spite of the static task demands.

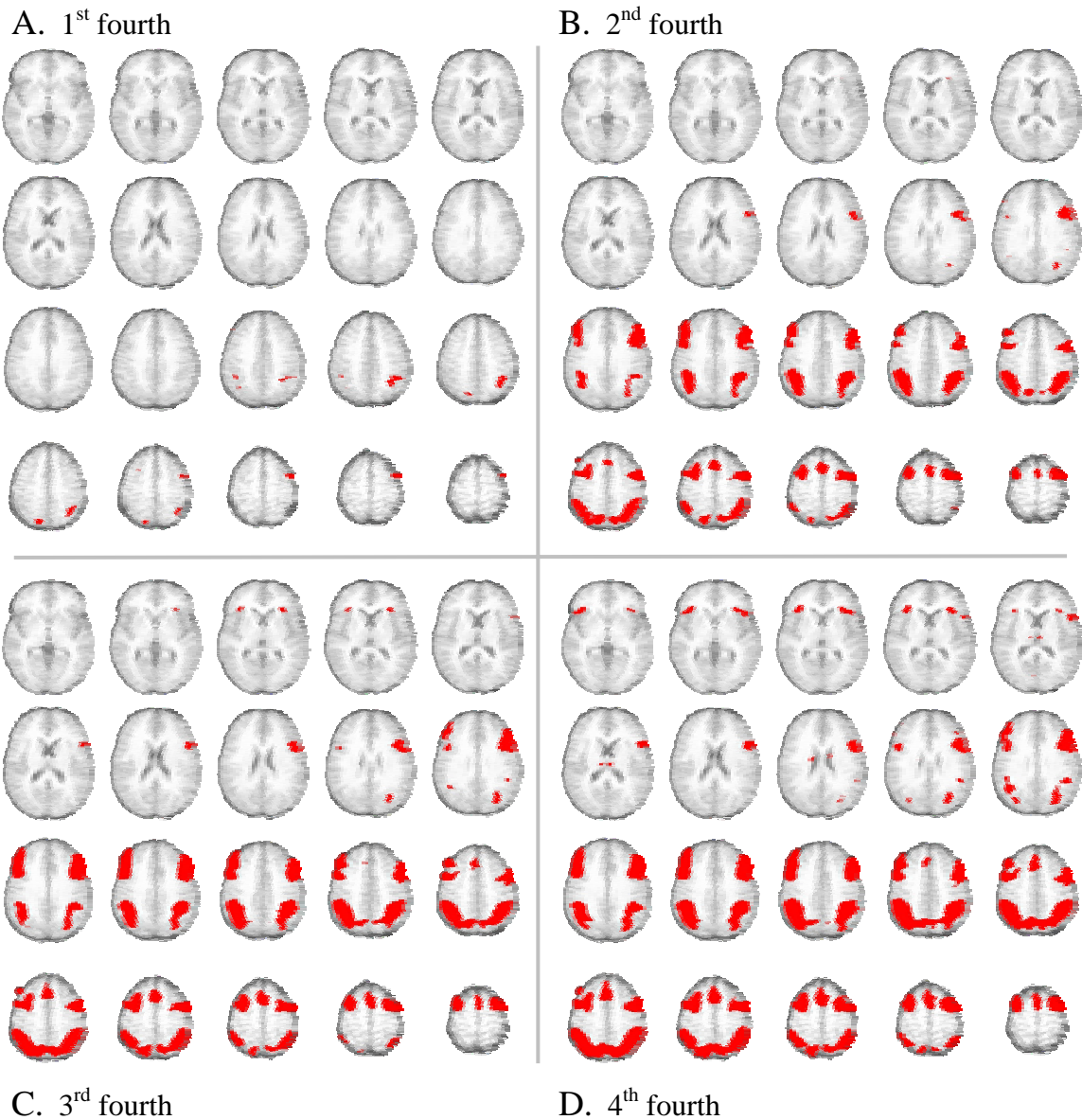


Figure 7.11 – Activation output from the fourths analysis of the 2-back working memory paradigm. The regions of activation represent the FDR thresholded ( $q = 0.01$ ) correlation output averaged from  $N = 17$  subjects, overlaid on the average of their anatomical data. Axial-plane images, shown with a 3-mm slice offset from one another, are provided from each of the four time interval segments in sequential order from (A.) – (D.).

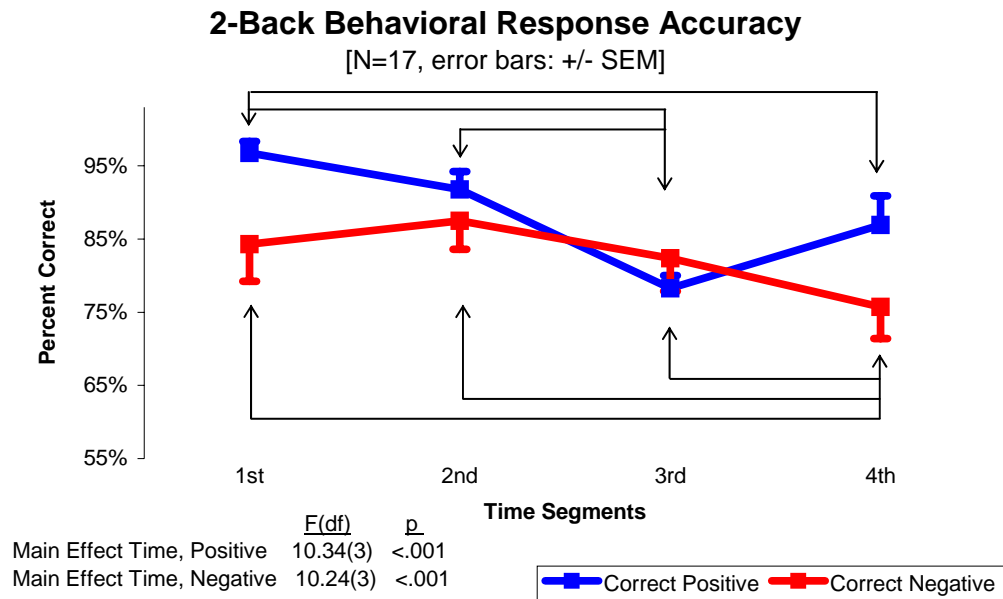


Figure 7.12 – Summary behavioral response data from the 2-back WM task. This figure plots accuracy as a percentage of the correct positive and correct negative responses over the four temporal intervals. Repeated measures ANOVA performed on the response data was found to indicate significant differences within each response category ( $P < .001$ ). The bracketed pairings between time intervals for either response category indicate the pairwise comparisons from post-hoc t-test analysis that were found to be significantly different ( $P < .02$ ). The significant differences between accuracy response scores over the time intervals are consistent with a decrease in subject performance in spite of the static task demands.

#### 4. Discussion

##### 4.1. Simple Motor Function

From this paradigm of self-paced, sustained motor activity, we observe patterns of neural activation that remain rather constant over the duration of the task and that are consistent with similar imaging studies of motor function (Rao *et al.*, 1993). To determine whether a statistically significant difference in regionally localized volumes of activation were present over the course of the intervals, three region-of-interest masks were created to encompass (1) left hemisphere primary sensorimotor region, (2) medial frontal supplementary motor area (SMA), and (3) right



hemisphere primary sensorimotor region. A rendering of the localization of the three ROI masks is provided in Fig. 7.13. Masking individual subject activation maps from the four task intervals with the ROIs enabled determination of the number of active voxels in a given region at each interval. A repeated measures ANOVA was conducted using the individual subject active voxel counts at each time segment as the dependent variable and found no significant variation in the volumes of activity over the course of the interval for any of the regions ( $P > .25$ ).

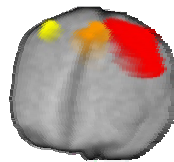


Figure 7.13 – Localization of three regions of interest used to investigate the variation in volumes of activity over the four task intervals in each of the respective motor control areas: primary sensorimotor region (red), supplementary motor region (orange), and contralateral sensorimotor region (yellow). ANOVA results indicated no significant variation in the volumes of activity over the course of the interval for any of the regions ( $P > .25$ ).

Several lines of evidence suggest that the SMA of the medial frontal region is important for the initiation of voluntary motor movement (Goldberg, 1985), including studies demonstrating that electrical stimulation of this region can elicit an urge to perform movement (Fried, 1996), and that Parkinson's disease is associated with impaired activation of the SMA (Passingham, 1996). Also, from EEG and motor fMRI studies (Weilke *et al.*, 1999) it is known that onset of the BOLD response in SMA occurs prior to that of the primary sensorimotor cortex. The results of the current work add to that body of knowledge by suggesting that the volume of

neural tissue in the medial frontal region remains constant over the duration of a sustained motor task. Contrary to a previous study of the sensorimotor region (Samuel *et al.*, 1998), the fourth analysis did not indicate development of any substantial volume of activation in the contralateral primary motor region. The observation of activity in the inferior parietal lobe at the later time intervals during the task is, however, consistent with other neuropsychological studies. The inferior parietal lobe is generally assumed to be involved in sensory awareness. This is based on the fact that neglect, which constitutes an attentional rather than a sensory deficit, is most commonly found after lesions of the inferior parietal lobe (Driver *et al.*, 1998). This consistency supports the instructional constraints of the task where subjects were asked to perform the right-hand opening and closing at a self-paced, but consistent, rate.

#### 4.2. Semantic Reasoning

Output from the semantic reasoning paradigm contributes to the notion that word retrieval depends on the operation of a distributed set of cortical regions, which includes regions outside the classically-defined, left-hemisphere language areas. For example, the observed right-hemisphere inferior-parietal activation noted during the initial interval of the task is an interesting observation that is consistent with arguments made by Beeman *et al.* (1994). Their work suggests that the contribution of the right hemisphere to linguistic activities is to bring together connotative associations. The semantic-reasoning task we presented to subjects was a single categorization task: living or non-living object. Being the region of right inferior-parietal-activation persists at only the initial time interval, we interpret this as a

reflection of the neural categorization processing strategy. That is, being the categorization strategy is constant throughout the task, after it is elicited at the onset of the categorization task, this component habituates and is no longer needed.

Another interesting finding from this analysis is the evolution of activity in the left hemisphere DLPFC. Grabowski *et al.* (1998) describe results from a word categorization study using PET that indicate a role for non-classical language areas in the processing of word retrieval. Their data suggest the premotor region is engaged in the retrieval of words denoting actions or objects that have characteristic actions. This is consistent with other PET studies involving verb generation from noun stimuli (Petersen *et al.*, 1988). Since the semantic-processing task we presented to subjects consisted of a series of noun words, the finding of activity in DLPFC is consistent with these previous PET studies. However, this task also entailed a decision-making component to it when subjects decided how to classify the noun. Given that the prefrontal cortex is widely recognized as a region with a primary role in higher cognitive functions such as planning, reasoning and decision making (Grafman, 1989), it is difficult to determine whether any observed variation of activation in this region is due to the language aspects or the decision-making aspects of the task.

#### 4.3. Visuospatial Processing

A prominent feature of the visuospatial processing activation in Fig. 7.9 is the variation in the volume of activation in the occipital lobe over the time intervals. We interpret the large blush of activation at the initial interval to be a result of the

inclusion of visual-feature-detection regions that extend outside of the primary visual cortex. This observation is consistent with the notion that after the transition from the control task, the feature-detection areas of the visual cortex are re-engaged, resulting in activation of brain that extends beyond primary visual cortex into the secondary visual processing areas. As the symbol-search component of the task progresses, the regions involved in the feature-detection aspect of the task habituate and are no longer needed. In addition to the large occipital region of activity, the posterior parietal and bilateral frontal lobe regions, each respectively responsible for iconic memory and executive control functions, show evolving volumes of activity over the time intervals, possibly reflecting a perceived increase in task difficulty over the duration of this task.

#### 4.4. Working Memory

The 2-back WM paradigm presents subjects with a series of static task demands over an extended period of time. The stimulus presentation of the 2-back differs from the two previous cognitive paradigms we have discussed in that the subject dictates the rate of stimulus presentation in those paradigms. In a previous, related study (Paskavitz *et al.*, 2003), we showed in the 2-back WM task that the volume of activation in anterior brain regions exhibited a significant increase over time, whereas activation in the posterior regions indicated a trend toward increased activation. These results suggest anterior regions increase recruitment of adjacent neural tissue as the task progresses, while simultaneously, from the behavioral response data of Fig. 7.12, we note that performance decreases as the task progresses. This inverse relationship may reflect compensation by these anterior

brain regions for impaired temporal information flow to frontal decision making areas, short-term-memory (STM) buffer saturation in bi-parietal regions, or both. We postulate that the STM buffer may be unable to cycle through constantly changing incoming information in an efficient manner, resulting in recruitment of more parietal resources. The frontal system response to this network demand is a disproportionately large recruitment of adjacent tissue to manage this information load effectively. This may reflect a temporally mediated capacity constraint on the *N*-back working memory network that has not been previously demonstrated.

#### 4.5. Data Analysis in Light of Heterogeneous BOLD Response

Interpretation of the differences in the activation patterns observed during the four temporal intervals of a given paradigm is complicated by the temporal dynamics of the hemodynamic response. Although the hemodynamic response for a given individual has been shown to be very stable in timing, shape and amplitude across separate measurements within a brain region (Dale *et al.*, 1997; Miezin *et al.*, 2000), across brain regions these response characteristics have been shown to vary (Buckner *et al.*, 1996; Schacter *et al.*, 1997; Aguirre *et al.*, 1998; Friston *et al.*, 1998; Miezin *et al.*, 2000). As a specific example, in the study by Miezen *et al.*, the BOLD response in the motor cortex was found to have a longer latency than in the visual cortex. These observations emphasize the fact that endogenous regional variability in the latency of hemodynamic responses hinders the utility of fMRI to resolve the temporal cascade of neural activity across the cortex. However, the experimental analysis presented in this work is not intended to discern the rapid succession of

neural events that embody a given task. Rather, the intent is to observe gross variations in a particular region over time during a period of sustained activity. As indicated in Fig. 7.4, the timing intervals in the fourths analysis are offset from one another by increments of 9 seconds. Given the known range of BOLD response characteristics, we know of no evidence that any brain region has a latency period on the order of 10's of seconds (Menon *et al.*, 2001). This argues that variations of activity observed within a given region over the timing intervals are neurally driven rather than artifactual consequences of the BOLD response. For example, in the 2-back WM paradigm, regions of increased activation volume were noted in bilateral regions of the frontal and parietal cortex over the temporal intervals, consistent with the notion of neural recruitment to satisfy increased WM processing demands. Additionally, during the visuospatial-processing paradigm, the volume of activity in the occipital cortex was observed to decrease over the intervals, a finding that is also consistent with the hypothesized neural activity in this region.

## 5. Conclusions

In this work, we have explored the use of a simple analysis method for observing dynamic changes in brain regions involved in different neural network processes during a period of sustained activity. The results are consistent with the idea that, over time, brain regions adapt to the given task demands through either recruitment or discharge of adjacent areas of tissue. These results also indicate that traditional analysis of block-design fMRI studies may underestimate dynamic changes in brain regions during a sustained task. This time-segment-analysis method may be useful as an exploratory tool to observe region-specific variations in activation that may allow inferences to be made

regarding how different brain regions adapt to and interact with one another during periods of extended activity.

## References

- Aguirre GK, Zarahn E, D'Esposito M, The variability of human, BOLD hemodynamic responses, *Neuroimage* **8**:360-369 (1998).
- Baddeley AD, Working memory, *Science* **255**:556-559 (1992).
- Bandettini PA, Wong EC, Hinks RS, Tikofsky RS, Hyde JS, Time course EPI of human brain function during task activation, *Magn Reson Med* **25**:390-397 (1992).
- Bandettini PA, Jesmanowicz A, Wong EC, Hyde JS, Processing strategies for time-course data sets in functional MRI of the human brain, *Magn Reson Med* **30**:161-173 (1993).
- Basser PJ, Mattiello J, LeBihan D, Estimation of the effective self-diffusion tensor from the NMR spin echo, *J Magn Res B*, **103**:247-254 (1994a).
- Basser PJ, Mattiello J, LeBihan D, MR diffusion tensor spectroscopy and imaging, *Biophys J* **66**:259-267 (1994b).
- Basser PJ, Pierpaoli C, Microstructural and physiological features of tissues elucidated by quantitative-diffusion-tensor MRI, *J Magn Res B* **111**:209-219 (1996).
- Basser PJ, Pierpaoli C, A simplified method to measure the diffusion tensor from seven MR images, *Magn Reson Med* **39**:928-934 (1998).
- Beeman M, Friedman RB, Grafman J, Perez E, Summation priming and coarse semantic coding in the right hemisphere, *J Cogn Neurosci* **6**:26-45 (1994).
- Benjamini Y, Hochberg Y, Controlling the false discovery rate: a practical and powerful approach to multiple testing, *J Royal Stat Soc Ser B* **57**:289-300 (1995).
- Berendsen HJC, Nuclear magnetic resonance study of collagen hydration, *J Chem Phys* **36**:3297-3305 (1962).
- Bloch F, Nuclear induction, *Phys Rev* **70**:460-474 (1946).
- Bloembergen N, Purcell EM, Pound RV, Relaxation effects in nuclear magnetic resonance absorption, *Phys Rev* **73**:670-712 (1948).
- Buckner RL, Bandettini PA, O'Craven KM, Savoy RL, Petersen SE, Raichle ME, Rosen BR, Detection of cortical activation during averaged single trials of a cognitive task using



- functional magnetic resonance imaging, *Proc Natl Acad Sci USA* **93**:14878-14883 (1996).
- Bullmore E, Horwitz B, Honey G, Brammer M, Williams S, Sharma T, How good is good enough in path analysis of fMRI data? *NeuroImage* **11**:289-301 (2000).
- Callaghan PT. Principles of Nuclear Magnetic Resonance Microscopy. Oxford University Press: New York, NY (1993).
- Chimich D, Shrive N, Frank C, Marchuk L, Bray R, Water content alters viscoelastic behaviour of the normal adolescent rabbit medial collateral ligament, *J Biomech* **25**:831-837 (1992).
- Conturo TE, McKinstry RC, Aronowitz JA, Neil JJ, Diffusion MRI: Precision, accuracy and flow effects, *NMR Biomed* **8**:307-332 (1995).
- Conturo TE, McKinstry RC, Akbudak E, Robinson BH, Encoding of anisotropic diffusion with tetrahedral gradients: a general mathematical diffusion formalism and experimental results, *Magn Reson Med* **35**:399-412 (1996).
- Cox RW, AFNI: Software for analysis and visualization of functional magnetic resonance neuroimages, *Comput Biomed Res* **29**:162-173 (1996).
- Dale AM, Buckner RL, Selective averaging of rapidly presented individual trials using fMRI, *Hum Brain Mapp* **5**:329-340 (1997).
- Damadian RV, Goldsmith M, Minkoff L, NMR in cancer: XVI. FONAR image of the live human body, *Physiol Chem Phys* **9**:97-100 (1977).
- Driver J, Mattingley JB, Parietal neglect and visual awareness, *Nature Neurosci* **1**:17-22 (1998).
- Edelstein WA, Hutchinson JMS, Johnson G, Redpath TW, Spin warp NMR imaging and application to human whole-body imaging, *Phys Med Biol* **25**:751-756 (1980).
- Elden HR, Hydration of connective tissue and tendon elasticity, *Biochem Biophys Acta* **79**:592-599 (1964).
- Ernst RR, Anderson WA, Application of Fourier transform spectroscopy to magnetic resonance, *Rev Sci Instr* **37**:93-102 (1966).
- Farrar TC. Introduction to Pulse NMR Spectroscopy. Farragut Press: Madison, WI (1989).

Fox PT, Raichle ME, Focal physiological uncoupling of cerebral blood flow and oxidative metabolism during somatosensory stimulation in human subjects, *Proc Natl Acad Sci USA* **83**:1140-1144 (1986).

Frank CB, Hart DA, "The Biology of Tendons and Ligaments," in Biomechanics of Diarthrodial Joints, Vol. 1. Mow VC, et al (eds.) Springer-Verlag: New York, NY (1990).

Fried I, Electrical stimulation of the supplementary sensorimotor area, *Adv Neurol* **70**:177-185 (1996).

Friston KJ, Fletcher P, Josephs O, Holmes A, Rugg MD, Turner R, Event-related fMRI: Characterizing differential responses, *Neuroimage* **7**:30-40 (1998).

Fullerton GD, Cameron IL, Ord VA, Orientation of tendons in the magnetic field and its effect on T<sub>2</sub> relaxation times, *Radiology* **155**:433-435 (1985).

Fullerton GD, Cameron IL, "Relaxation of Biological Tissues," in Biomedical Magnetic Resonance Imaging: Principles, Methodology and Applications. Wehrli FW, Shaw D, Kneeland JB (eds.) VHC Publishers: New York, NY (1988).

Grabowski TJ, Damasio H, Damasio R, Premotor and prefrontal correlates of category-related lexical retrieval, *Neuroimage* **7**:232-243 (1998).

Gadian DG. NMR and Its Applications to Living Systems. Oxford University Press: New York, NY (1995).

Genovese CR, Lazar NA, Nichols T, Thresholding of statistical maps in functional neuroimaging using the false discovery rate, *Neuroimage* **15**:870-878 (2002).

Goldberg G, Supplementary motor area structure and function: review and hypotheses, *Behav Brain Sci* **8**:567-619 (1985).

Grafman J. Neuropsychology. Erlbaum: Hillsdale, NJ (1989).

Guyton AC, Hall JE. Textbook of Medical Physiology. WB Saunders: Philadelphia, PA (1996).

Hahn EL, Spin echoes, *Phys Rev* **80**:580-594 (1950).

Haken R, Blumich B, Anisotropy in tendon investigated in vivo by a portable NMR scanner, the NMR-MOUSE, *J Magn Reson* **144**:195-199 (2000).

Han S, Gemmell SJ, Helmer KG, Grigg P, Wellen JW, Hoffman AH, Sotak CH, Changes in ADC caused by tensile loading of rabbit Achilles tendon: Evidence for water transport, *J Magn Reson* **144**:217-227 (2000).

Hannafin JA, Arnoczky SP, Effect of cyclic static tensile loading on water content and solute diffusion in canine flexor tendons: An *in vitro* study, *J Ortho Res* **12**:350-356 (1994).

Helmer KG, Dardzinski BJ, Sotak CH, The application of porous-media theory to the investigation of time-dependent diffusion in *in vivo* systems, *NMR Biomed* **8**:297-306 (1995).

Henkelman RM, Stanisz GJ, Kim JK, Bronskill MJ, Anisotropy of NMR properties of tissues *Magn Reson Med* **32**:592-601 (1994).

Jozsa L, Kannus P, Balint JB, Reffy A, Three-dimensional ultrastructure of human tendons, *Acta Anat* **142**:306-312 (1991).

Jozsa LG, Kannus P. Human Tendons. Human Kinetics: Champaign, IL (1997).

Karni A, Meyer G, Jezard P, Adams MM, Turner R, Ungerleider LG, Functional MRI evidence for adult motor cortex plasticity during motor skill learning, *Nature* **377**:155-158 (1995).

Kastelic J, Galiski A, Baer E, The multicomposite structure of tendon, *Conn Tis Res* **6**:11-23 (1978).

Kolb B, Whishaw IQ. Fundamentals of human neuropsychology. WH Freeman: New York, NY (1990).

Kwong KK, Belliveau JW, Chesler DA, Goldberg IE, Weisskoff RM, Poncelet BP, Kennedy DN, Hoppel BE, Cohen MS, Turner R, Cheng HM, Brady TJ, Rosen BR, Dynamic magnetic resonance imaging of human brain activity during primary sensory stimulation, *Proc Natl Acad Sci USA* **89**:5675-5679 (1992).

Lauterbur PC, Image formation by induced local interactions: Examples employing nuclear magnetic resonance, *Nature* **242**:190-191 (1973).

Le Bihan D, Breton E, Lallemand D, Grenier P, Cabanis E, Laval-Jeantet N, MR imaging of intravoxel incoherent motions: Applications to diffusion and perfusion in neurologic disorders. *Radiology*, **161**:401-407 (1986).

Malonek D, Grinvald A, Interactions between electrical activity and cortical microcirculation revealed by imaging spectroscopy: implications for functional brain mapping, *Science* **272**:551-554 (1996).

Mansfield P, Multi-planar image formation using NMR spin echoes, *J Phys Chem* **10**:L55-58 (1977).

- Martin RB, Burr DB, Sharkey NA. Skeletal Tissue Mechanics. Springer-Verlag: New York, NY (1998).
- Mattiello J, Basser PJ, LeBihan D, Analytical expressions for the  $b$  matrix in NMR diffusion imaging and spectroscopy, *J Magn Res A* **108**:131-141 (1994).
- Mattiello J, Basser PJ, LeBihan D, The  $b$  matrix in diffusion tensor echo-planar imaging, *Magn Reson Med* **37**:292-300 (1997).
- McIntosh AR, Gonzalez-Lima F, Structural equation modeling and its application to network analysis in functional brain mapping, *Human Brain Map* **2**:2-22 (1994).
- McIntosh AR, Cabeza RE, Lobaugh NJ, Analysis of neural interactions explains the activation of occipital cortex by an auditory stimulus, *J Neurophys* **80**:2790-2796 (1998).
- McKeown MJ, Detection of consistently task-related activations in fMRI data with hybrid independent component analysis, *NeuroImage* **11**:24-35 (2000).
- Menon RS, Goodyear BG, "Spatial and temporal resolution in fMRI," in Functional MRI, Jezzard P, Matthews PM, Smith SM, (eds.) Oxford University Press: New York, NY (2001).
- Miezin FM, Maccotta L, Ollinger JM, Petersen SE, Buckner RL, Characterizing the hemodynamic response: effects of presentation rate, sampling procedure, and the possibility of ordering brain activity based on relative timing, *Neuroimage* **11**:735-759 (2000).
- Mitra PP, Sen PN, Schwartz LM, Le Doussal P, Diffusion propagator as a probe of the structure of porous media, *Phys Rev Lett* **68**:3555-3558 (1992).
- Mitra PP, Sen PN, Schwartz LM, Short-time behavior of the diffusion coefficient as a geometrical probe of porous media, *Phys Rev B* **47**:8565-8574 (1993).
- Mori S, van Zijl PC, Diffusion weighting by the trace of the diffusion tensor within a single scan, *Magn Res Med* **33**:41-52 (1995).
- Mow VC, Holmes MH, Lai WM, Fluid transport and mechanical properties of articular cartilage: A review, *J Biomech* **17**:377-394 (1984).
- Ogawa S, Lee TM, Kay AR, Tank DW, Brain magnetic resonance imaging with contrast dependent on blood oxygenation, *Proc Natl Acad Sci USA* **87**:9868-9872 (1990).
- Ogawa S, Tank DW, Menon R, Ellermann JM, Kim SG, Merkle H, Ugurbil K, Intrinsic signal changes accompanying sensory stimulation: Functional brain mapping with magnetic resonance imaging, *Proc Natl Acad Sci USA* **89**:5951-5955 (1992).

Papadakis NG, Xing D, Huang CLH, Hall LD, Carpenter TA, A comparative study of acquisition schemes for diffusion tensor imaging using MRI, *J Magn Res* **137**:67-82 (1999).

Paskavitz JP, Sweet L, Wellen J, Helmer KG, and Cohen R, Dynamic changes in brain volumes of activation during sustained working memory observed with fMRI, Thirty-first Annual Meeting of the International Neuropsychological Society, Honolulu, Hawai'i, USA (2003).

Passingham RE, Functional specialization of the supplementary motor area in monkeys and humans, *Adv Neurol* **70**:105-116 (1996).

Pauling L, Coryell C, The magnetic properties and structure of hemoglobin, oxyhemoglobin and carbon monoxyhemoglobin, *Proc Natl Acad Sci USA* **22**:210-216 (1936).

Petersen SE, Fox PT, Posner MI, Mintun M, Raichle ME, Positron emission tomographic studies of the cortical anatomy of single-word processing, *Nature* **331**:585-589 (1988).

Peto S, Gillis P, Henri VP, Structure and dynamics of water in tendon from NMR relaxation measurements, *Biophys J* **57**:71-84 (1990a).

Peto S, Gillis P, Fiber-to-field angle dependence of proton nuclear magnetic relaxation in collagen, *Magn Reson Imag* **8**:705-712 (1990b).

Rao SM, Binder JR, Bandettini PA, Hammeke TA, Yetkin FZ, Jesmanowicz A, Lisk LM, Morris GL, Mueller WM, Estkowski LD, Functional magnetic resonance imaging of complex human movements, *Neurology* **43**:2311-2318 (1993).

Rao SM, Mayer AR, Harrington DL, The evolution of brain activation during temporal processing, *Nature Neurosci* **4**:317-323 (2001).

Russ JC. The Image Processing Handbook. CRC Press: Boca Raton, FL (1995).

Samuel M, Williams SC, Leigh PN, Simmons A, Chakraborti S, Andrew CM, Friston KJ, Goldstein LH, Brooks DJ, Exploring the temporal nature of hemodynamic responses of cortical motor areas using functional MRI, *Neurology* **51**:1567-1575 (1998).

Schacter DL, Buckner RL, Koutstaal W, Dale AM, Rosen BR, Late onset of anterior prefrontal activity during true and false recognition: An event-related fMRI study, *Neuroimage* **6**:259-269 (1997).

Silver FH. Biological Materials: Structure, Mechanical Properties, and Modeling of Soft Tissues. New York University Press: New York, NY (1987).

Stejskal EO, Use of spin-echoes in a pulsed magnetic field gradient to study anisotropic, restricted diffusion and flow, *J Chem Phys*, **43**:3597-3603 (1965).

Stejskal EE, Tanner JE. Spin diffusion measurements: spin echoes in the presence of a time-dependent field gradient. *J Chem Phys*, **42**:288-292 (1965).

Talairach J, Tournoux P. Co-planar Stereotactic Atlas of the Human Brain. Thieme Medical Publishers: New York, NY (1988).

Taylor DG, Bushell MC, The spatial mapping of translational diffusion coefficients by the NMR imaging technique, *Phys Med Biol*, **30**:345-349 (1985).

Tufte ER. The Visual Display of Quantitative Information. Graphics Press: Cheshire, CT (1983).

Turner R, Le Bihan D, Single-shot diffusion imaging at 2.0 Tesla, *J Magn Reson* **86**:445-452 (1990).

Turner R, Le Bihan D, Moonen CT, Despres D, Frank J, Echo-planar time course MRI of cat brain oxygenation changes, *Magn Reson Mes* **22**:159-166 (1991).

Viidik A, "Structure and Function of Normal Healing Tendons and Ligaments," in Biomechanics of Diarthrodial Joints, Vol. 1. Mow VC, et al (eds.) Springer-Verlag: New York, NY (1990).

Weilke F, Spiegel S, Grafin V, Einsiedel H, Boecker H, Schwaiger M, Bartenstein P, Conrad B, Erhard P, Time-resolved fMRI of sequential activation in SMA and M1 (abstr), in *Proc Int Soc Magn Reson Med* **2**, 773 (1999).

Wellen J, Helmer KG, Grigg P, Sotak CH, Impact of tensile load on rabbit Achilles tendon characterized by MRI spatial differentiation of T<sub>1</sub>, T<sub>2</sub> and ADC parameters (abstr), in *Proc Int Soc Magn Reson Med* **2**, 863 (2001).

Wellen J, Helmer KG, Grigg P, Sotak CH, Spatial characterization of the time-dependent ADC of water in rabbit Achilles tendon subject to tensile loading (abstr), in *Proc Int Soc Magn Reson Med* **3**, 1816 (2002).

Whittall KP, MacKay AL, Quantitative interpretation of NMR relaxation data, *J Magn Reson* **84**:134-152 (1989).

Winkler ML, Ortendahl DA, Mills TC, Crooks LE, Sheldon PE, Kaufman L, Kramer DM, Characteristics of partial flip angle and gradient reversal MR imaging, *Radiology* **166**:17-26 (1988).

Wong EC, Cox RW, Song AW, Optimized isotropic diffusion weighting, *Magn Res Med* **34**:139-143 (1995).

Woo SL-Y, Gomez MA, Akeson WH, The time and history-dependent viscoelastic properties of the canine medial collateral ligament, *J Biomech Eng*, **103**:293-298 (1981).

# Curriculum Vitae

## JEREMY WELLEN

22 Merlin Court  
Worcester, MA 01602  
(508) 798-3292      *jwellen@wpi.edu*

### EDUCATION

1995	B.S.	Biomedical Engineering	Boston University	Boston, MA
2001	M.E.	Biomedical Engineering	Worcester Polytechnic Institute	Worcester, MA
2003	Ph.D.	Biomedical Engineering	Worcester Polytechnic Institute	Worcester, MA

### PROFESSIONAL

#### EXPERIENCE

**Research Assistant, *Biomedical Engineering Department, Worcester Polytechnic Institute, Worcester, MA***      September 1998 – present

Conducted applied research in biomedical science using nuclear magnetic resonance spectroscopy (MRS) and imaging (MRI). Research topics included investigations of water diffusion in tendon while subject to tensile loading in both MRS and MRI modalities; characterization of intervertebral disc morphology with high-resolution MRI; (both studies performed on a GE 2T CSI-II imaging spectrometer) and clinical functional MRI (fMRI) studies of neural network function using simple motor, language, visuospatial and cognitive working memory paradigms (performed on a GE Signa LX scanner). Responsibilities in this position include: general maintenance of and pulse sequence development on the GE research imaging spectrometer; design and fabrication of RF coils; software development for data processing and image analysis using C and IDL programming environments; construction and maintenance of a multi-system (i.e. SGI IRIX, Linux and Windows NT workstations) LAN for the laboratory.

**Mechanical Engineer, *Mentor Ophthalmics, Norwell, MA***      June 1996 – September 1998

Member of the development team that brought a novel hydrophilic, thermoplastic intraocular lens (IOL) implant (MemoryLens®) to market – FDA approval received December 1997.

**QC Technician, *Belmont Instruments, Billerica, MA***      May 1993 – December 1993

A student co-op experience in the quality control department. Responsibilities included operational testing and troubleshooting of electromechanical modules, printed circuit boards and final assemblies of intra-aortic balloon pumps (IABP) and blood infusion systems.

### AWARDS & SOCIETY

#### MEMBERSHIPS

USDE GAANN Fellowship, Worcester Polytechnic Institute, 1998-present.  
International Society of Magnetic Resonance in Medicine, 1998-present.

### PUBLICATIONS

Changes in ADC Caused by Tensile Loading of Rabbit Achilles Tendon: Evidence for Water Transport, S. Han, S.J. Gemmell, K.G. Helmer, P. Grigg, J. Wellen, A.H. Hoffman, and C.H. Sotak, *J. Magn. Reson.* **144**, 217-227 (2000).

Spectroscopic Characterization of the Diffusion-Time Dependence of the Water ADC in Rabbit Achilles Tendon, J. Wellen, K.G. Helmer, P. Grigg, and C.H. Sotak (*in preparation*).



Spatial Characterization of Relaxation Parameters and the Water ADC in Rabbit Achilles Tendon Subject to Tensile Loading, J. Wellen, K.G. Helmer, P. Grigg, and C.H. Sotak (*in preparation*).

Measurement of the Spatial Redistribution of Water in Rabbit Achilles Tendon in Response to Static Tensile Loading, K.G. Helmer, J. Wellen, P. Grigg, and C.H. Sotak (*in preparation*).

## CONFERENCE PROCEEDINGS

Investigations of Water Transport in Rabbit Achilles Tendon Under Load, J.W. Wellen, K.G. Helmer, P. Grigg, and C.H. Sotak, Oral presentation at the IEEE 26<sup>th</sup> Annual Northeast Bioengineering Conference, University of Connecticut, Storrs, Connecticut, April, 2000; also published in *Proc. IEEE 26<sup>th</sup> Annual Northeast Bioeng. Conf.*, 15-16 (2000).

Large-q Investigations of the Effects of Static Loading on Rabbit Achilles Tendon, K.G. Helmer, J.W. Wellen, P. Grigg, and C.H. Sotak, Abstract, Poster presented at the 41<sup>st</sup> Experimental NMR Spectroscopy Conference, Pacific Grove, California, April, 2000.

Spatially Resolved Changes in Water ADC Caused by Tensile Loading of Rabbit Achilles Tendon, K.G. Helmer, J.W. Wellen, P. Grigg, and C.H. Sotak, Abstract, Poster presented at the 42<sup>nd</sup> Experimental NMR Spectroscopy Conference, Orlando, Florida, March, 2001.

Impact of Tensile Load on Rabbit Achilles Tendon by MRI Spatial Differentiation of T<sub>1</sub>, T<sub>2</sub> and ADC Parameters, J.W. Wellen, K.G. Helmer, P. Grigg, and C.H. Sotak, Abstract, Poster Presented at the Ninth Scientific Meeting of the International Society of Magnetic Resonance in Medicine, Glasgow, Scotland, U.K., April, 2001; also published in *Proc. Int. Soc. Magn. Reson. Med.* **2**, 863 (2001).

Measurement of the Spatial Redistribution of Water in Rabbit Achilles Tendon in Response to Static Tensile Loading, K.G. Helmer, J. Wellen, P. Grigg, and C.H. Sotak, Abstract, Poster presented at the Tenth Scientific Meeting of the International Society of Magnetic Resonance in Medicine, Honolulu, Hawai'i, USA, May, 2002; also published in *Proc. Int. Soc. Magn. Reson. Med.* **3**, 1809 (2002).

Spatial Characterization of the Time-Dependent ADC of Water in Rabbit Achilles Tendon Subject to Tensile Loading, J. Wellen, K.G. Helmer, P. Grigg, and C.H. Sotak, Abstract, Poster presented at the Tenth Scientific Meeting of the International Society of Magnetic Resonance in Medicine, Honolulu, Hawai'i, USA, May, 2002; also published in *Proc. Int. Soc. Magn. Reson. Med.* **3**, 1816 (2002).

Dynamic Changes in Brain Volumes of Activation During Sustained Working Memory Observed with fMRI, J. Paskavitz, L. Sweet, J. Wellen, K. Helmer, and R. Cohen, Abstract, Poster presented at the Thirty-first Annual Meeting of the International Neuropsychological Society, Honolulu, Hawai'i, USA, February, 2003.

A Functional Magnetic Resonance Imaging Study of Word Similarity Effects, L. Sweet, J. Paskavitz, J. Wellen, R. Cohen, Abstract, Poster presented at the Thirty-first Annual Meeting of the International Neuropsychological Society, Honolulu, Hawai'i, USA, February, 2003.

Improving the Visibility of Catheters for Interventional Procedures Under MRI Guidance, S. Zhong, E. Ma, J. Wellen, L. Dao, C.H. Sotak, Abstract, Poster presented at the 44<sup>th</sup> Experimental NMR Spectroscopy Conference, Savannah, GA, March/April, 2003.

Dynamic Changes in Neural Network Activation Patterns During Sustained Motor and Cognitive Tasks Observed with fMRI, J. Wellen, L. Sweet, K.G. Helmer, C.H. Sotak, and J. Paskavitz, Abstract, Poster presented at the Eleventh Scientific Meeting of the International Society of Magnetic Resonance in Medicine, Toronto, Ontario, Canada, May, 2003; also published in *Proc. Int. Soc. Magn. Reson. Med.* **3**, 1922 (2003).

